VISCOELASTIC CHARACTERIZATION OF RABBIT NUCLEUS PULPOSUS TISSUE IN TORSIONAL CREEP

by

Christopher D. Agosti

BS in Mechanical Engineering, The Pennsylvania State University, 2004

Submitted to the Graduate Faculty of the

School of Engineering in partial fulfillment

of the requirements for the degree of

Master of Science in Mechanical Engineering

University of Pittsburgh

2006

UNIVERSITY OF PITTSBURGH

SCHOOL OF ENGINEERING

This thesis was presented

by

Christopher David Agosti

It was defended on

April 27, 2006

and approved by

Dr. Donald J. Plazek, Professor Emeritus, Dept. of Material Science and Engineering

Dr. Lars G. Gilbertson, Associate Professor, Dept. of Orthopedic Surgery

Dr. Patrick J. Smolinski, Associate Professor, Dept. of Mechanical Engineering
Thesis Advisor

VISCOELASTIC CHARACTERIZATION OF RABBIT

NUCLEUS PULPOSUS TISSUE IN TORSIONAL CREEP

Christopher D. Agosti, MS

University of Pittsburgh, 2006

Recently, molecular therapy approaches have been shown to favorably alter the course of intervertebral disc degeneration (IDD) in a rabbit model. Typical experimental outcome measures for the rabbit model of IDD include MRI, x-ray, histology, and gene expression. Biomechanical function is another desirable parameter through which to compare treatments, although this is difficult due to limited availability of data for small animal models. In the current study, nucleus pulposus tissue was taken from the healthy rabbit intervertebral disc and tested in torsional creep to establish a database of healthy tissue behavior for future use in assessing the functional efficacy of molecular therapy treatments of IDD.

Nucleus pulposus tissue was excised from the L5-L6 intervertebral disc, mounted between the cone and plate of an AR1000 Rheometer, and various torsional creep experiments were performed. Several creep models were fit to the data and modeling analyses were conducted. Of the models compared, the Andrade creep model provides the most reliable data extrapolation. It appears that the tissue is nonlinearly viscoelastic since it does not adhere to the Boltzmann superposition principle. A nonlinear viscoelastic constitutive model, derived for Andrade creep and used to predict the strain behavior obtained at higher levels of stress, provides

consistent prediction results. The application of this model to degenerated rabbit NP tissue is expected to result in altered model parameters – thus providing quantifiable, functional benchmarks of success for molecular therapy approaches to the treatment of IDD.

TABLE OF CONTENTS

ACKNOWLEDGEMENTS xvii

LIST OF ABBREVIATIONS xviii

1.0 INTRODUCTION 1

2.0 BACKGROUND 3

2.1 THE INTERVERTEBRAL DISC 3

2.1.1 Composition 3

2.1.2 Biomechanics 5

2.1.3 Biochemistry of Proteoglycan and Collagen in the IVD 6

2.1.4 Mechanical Testing of the Intervertebral Disc 7

2.2 INTERVERTEBRAL DISC DEGENERATION 12

2.2.1 Overview and Impact 12

2.2.2 General Features of IDD 13

2.2.3 Pain attributed to IDD 18

2.2.4 Animal models of IDD 19

2.2.5 Treatments of IDD 20

2.2.6 Evaluation of Treatment Efficacy 22

2.3 VISCOELASTICITY 22

2.3.1 Foundational Work and Preliminaries 22

2.3.2 Viscoelastic Solids and Viscoelastic Fluids 25

2.3.3 Common Mechanical Testing Techniques 27
2.3.4 Linear Viscoelasticity 30
2.3.5 Nonlinear Viscoelasticity 34
2.3.6 Andrade Creep 38
3.0 SPECIFIC AIMS 42
3.1 ESTABLISH PROCEDURE FOR TESTING RABBIT NP TISSUE 42
3.2 BUILD DATABASE OF RABBIT NP TISSUE CREEP BEHAVIOR 42
3.3 APPLY CONSTITUTIVE MODEL TO DESCRIBE TISSUE BEHAVIOR 42
4.0 EXPERIMENTAL METHODS 43
4.1 INSTRUMENTATION 43
4.1.1 AR1000 Rheometer 43
4.1.2 Cone and Plate Geometry 45
4.2 PRE-EXPERIMENTATION SETUP 47
4.2.1 Instrument Setup and Calibration 47
4.2.2 Specimen Preparation and Installation 48
4.3 EXPERIMENTAL TESTING PROCEDURES 50
4.3.1 Variable Stress Testing 50
4.3.2 Consecutive Creep Testing at 6 Pa Stress 51
4.3.3 Mineral Oil Dye Testing 52
4.3.4 General Humidity Chamber Setup and Testing 53
4.3.5 Variable Temperature Testing 58
4.4 POST-EXPERIMENTAL PROCEDURES 59
4.4.1 Data Extraction and Processing 59

4.4.2 Quasilinear Viscoelasticity (QLV) Statistical Analysis 60
4.4.3 Critical Strain Yield Analysis 61
4.4.4 Computer Assisted Curve Fitting Method 63
4.4.5 Model Extrapolation Analysis 64
4.4.6 Test for Boltzmann Superposition Principle Adherence 64
4.4.7 Analysis of Isochronal Creep Data on Linear Axes of Strain Versus Stress 66
4.4.8 Analysis of Isochronal Data on Log-Log Axes of Strain Versus Stress 66
4.4.9 Strain Prediction at Stresses of 18 Pa and 54 Pa 68
4.4.10 Analysis of Consecutive Creep Testing Data 72
4.4.11 Analysis of Heat Transfer Through NP Tissue at 40 ºC 73
5.0 RESULTS 75
5.1 VARIABLE STRESS TESTING DATA SET (N = 9) 75
5.1.1 General Observations 75
5.1.2 Creep Steps Performed at 2 Pa Shear Stress 81
5.1.3 Quasi-Linear Viscoelasticity (Factorization) Statistical Analysis Results 82
5.1.4 Critical (Yield) Strain Analysis 84
5.2 MODELING ANALYSIS (N = 5) 87
5.2.1 General Andrade Creep Model Fitting 87
5.2.2 Computer Assisted Curve Fits 87
5.2.3 Comparison of Andrade and Nutting Models 89
5.2.4 Extrapolation of Entire Data Range as a Measure of Model Performance 91
5.2.5 Boltzmann Superposition Principle Adherence 94
5.2.6 Isochronal Data Analysis on Linear Axes 97

5.2.7 Isochronal Data Analysis on Log-Log Axes 98
5.2.8 Strain Prediction at Stresses of 18 Pa and 54 Pa 101
5.3 MINERAL OIL VALIDATION TESTING 106
5.3.1 Consecutive Creep Testing at 6 Pa (N = 10) 106
5.3.2 Mineral Oil Dye Testing (N = 3) 111
5.4 HUMIDITY CHAMBER EXPERIMENTATION 113
5.4.1 Temperature Testing Heat Transfer Analysis Results 113
5.4.2 Temperature Ramp Test Results 114
5.4.3 Specimen Creep Performance Using Mineral Oil Versus Humidity Chamber 116
6.0 DISCUSSION 120
6.1 VARIABLE STRESS TESTING DATA SET 120
6.2 MODELING ANALYSIS 124
6.3 MINERAL OIL VALIDATION TESTING 130
6.4 HUMIDITY CHAMBER EXPERIMENTATION 133
7.0 CONCLUSION 138
8.0 FUTURE WORK 140
APPENDIX A. MANUAL CURVE FITTING OF ANDRADE CREEP MODEL 141
APPENDIX B. ISOCHRONAL DATA R^2 AND ADJUSTED-R^2 VALUES 149
APPENDIX C. POST-YIELD MENDING TESTING 150
APPENDIX D. CONSTITUTIVE MODEL USING COMBINED PARAMETERS 153
APPENDIX E. VARIABLE HYDRATION TESTING MASTER CREEP CURVES 155
APPENDIX F. DEFINITIONS OF STATISTICAL PARAMETERS [92] 159
BIBLIOGRAPHY 161

LIST OF TABLES

Table 2.1 Biomechanical testing of the intact intervertebral disc.[10-30] 9

Table 2.2 Biomechanical testing of the nucleus pulposus.[4, 33 – 38] 10

Table 2.3 Biomechanical testing of the annulus fibrosus.[34,35,39-44] 11

Table 2.4 Biomechanical testing of the cartilaginous endplate.[45-47] 11

Table 4.1 Variable stress testing procedure. 51

Table 4.2 Procedural summary for consecutive creep testing. 52

Table 4.3 Humidity chamber operation modes and corresponding testing procedures. 57

Table 4.4 Temperature ramp up (or down) testing procedure between 25 ºC and 40 ºC. 58

Table 4.5 Temperature ramp-up ramp-down testing procedure between 25 ºC and 40 ºC. 59

Table 4.6 Hand calculations: Basic simplifying assumptions and thermal conductivities used.. 73

Table 4.7 3-D FEA model: Assumptions, boundary conditions, and model parameters..... 74

Table 5.1 Calculated creep rates from 2 to 4 seconds and statistical analysis variables. 83

Table 5.2 Statistical outcome data of QLV M-ANOVA. Statistical significance, *p*, is in bold. . 84

Table 5.3 Relevant critical strain data at time of yield inflection point. 85

Table 5.4 Andrade creep model fit statistics and parameters from curve fitting program. 88

Table 5.5 Nutting model fit statistics and parameters obtained with curve fitting program. 89

Table 5.6 R-squared and adjusted R-squared values for isochronal data regressions. 98

Table 5.7 Stress power, m, obtained using isochronal data on log-log axes of strain vs. stress.. 99

Table 5.8 QLV model parameters for strain prediction at applied stresses of 18 Pa and 54 Pa. 102

Table 5.9 R^2 values for QLV model and linear viscoelastic model strain predictions. 105

Table 5.10 SSE values for QLV model and linear viscoelastic model strain predictions. 105

Table 5.11 Percent error in compliance between each of first four creep steps at 300 seconds.110

Table A.1 Fit statistics and model parameters for manually fit Andrade creep model. 144

Table A.2 Comparison of computer vs. manual model fits. 148

Table B.3 R^2 and adjusted-R^2 values of isochronal data 1st and 2nd order regressions. 149

Table D.4 Determination of constitutive model parameters with Rab 9 as an outlier. 153

LIST OF FIGURES

Figure 2.1 Representations of the IVD with nucleus pulposus and annulus fibrosus..... 4

Figure 2.2 Compressive loading of the healthy IVD. 6

Figure 2.3 Representations of IDD features. 15

Figure 2.4 Depiction of annular herniation. 18

Figure 2.5 Depiction of longitudinal strain (a) and shear strain (b)..... 24

Figure 2.6 Ideal strain behavior of (a) viscoelastic solids and (b) viscoelastic fluids with time. 26

Figure 2.7 Typical behavior of a viscoelastic solid in (a) creep and (b) stress relaxation.[73] 28

Figure 2.8 Demonstration of Boltzmann superposition principle..... 32

Figure 2.9 Plots of (a) compliance and (b) strain versus time for a linear viscoelastic material. 33

Figure 2.10 Isochronal data for (a) linear and (b) nonlinear viscoelastic materials. 34

Figure 2.11 Compliance vs. time plots of yielding behavior on (a) linear and (b) log-log axes. 36

Figure 2.12 Depiction of QLV in creep compared to more general nonlinearity. 37

Figure 2.13 Depiction of the Andrade creep model (in form of equation 2.15). 40

Figure 4.1 (a) AR 1000 Rheometer. (b) Detail of Peltier plate with 6 mm conical geometry.... 44

Figure 4.2 Representation of (a) cone and plate geometry and (b) parallel plate geometry. 46

Figure 4.3 Axial cross-section of rabbit intervertebral disc. 49

Figure 4.4 Photograph of fixtured NP specimen. Geometry gap is completely filled. 49

Figure 4.5 Photograph showing fixtured NP with mineral oil applied. 50

Figure 4.6 Rheometer setup with prototype humidity chamber and supporting subsystems. 55

Figure 4.7 Representation of initial procedure for the equilibration mode..... 57

Figure 4.8 Depiction of relative minimum velocity to obtain yield onset time, t_y. 62

Figure 4.9 Schematic of 1-D conduction analysis. 74

Figure 5.1 Creep data showing strain (absolute value) plotted versus time on log-log axes..... 76

Figure 5.2 Recovery data showing strain (absolute value) plotted versus time (log-log axes). .. 76

Figure 5.3 Creep data showing strain (absolute value) plotted versus time on linear axes. 77

Figure 5.4 Recovery data showing strain (absolute value) plotted versus time on linear axes. .. 77

Figure 5.5 Creep data plotted on log-log axes of compliance versus time. 79

Figure 5.6 Recovery data plotted on log-log axes of compliance versus time. 79

Figure 5.7 Creep data plotted on linear axes of compliance versus time. 80

Figure 5.8 Recovery data plotted on linear axes of compliance versus time. 80

Figure 5.9 Plot of strain vs. time (log-log) portraying reversal of creep direction. 81

Figure 5.10 Linear plot showing creep strain versus time. 82

Figure 5.11 Mean creep rates at each applied stress and the associated standard deviation. 83

Figure 5.12 Yielding and non-yielding behavior on linear axes of creep compliance vs. time... 86

Figure 5.13 Log-log plot of strain versus time showing yielding and non-yielding..... 86

Figure 5.14 Andrade creep fits (lines) and associated data (dots) on linear axes. 88

Figure 5.15 Comparison of SSE between Andrade and Nutting models..... 90

Figure 5.16 Compliance vs. time plot of data with Andrade and Nutting models. 91

Figure 5.17 Extrapolation of model based on first 300 s of data for *rab 8*..... 92

Figure 5.18 Extrapolation of model based on first 300 s of data for *rab 9*..... 92

Figure 5.19 Extrapolation of model based on first 300 s of data for *rab 12*..... 93

Figure 5.20 Extrapolation of model based on first 300 s of data for *rab 13*..... 93

Figure 5.21 Extrapolation of model based on first 300 s of data for *rab 15*..... 94

Figure 5.22 Actual and predicted recovery for *Rab 8*. $R^2 = 0.9816$, SSE = 0.00518. 95

Figure 5.23 Actual and predicted recovery for *Rab 9*. $R^2 = 0.5264$, SSE = 0.00770. 95

Figure 5.24 Actual and predicted recovery for *Rab 12*. $R^2 = 0.8551$, SSE = 0.02495. 96

Figure 5.25 Actual and predicted recovery for *Rab 13*. $R^2 = 0.9304$, SSE = 0.01748. 96

Figure 5.26 Actual and predicted recovery for *Rab 15*. $R^2 = 0.9483$, SSE = 0.01472. 97

Figure 5.27 Isochronal data for *Rab 8* on (a) linear and (b) log-log axes of strain vs. stress. 99

Figure 5.28 Isochronal data for *Rab 9* on (a) linear and (b) log-log axes of strain vs. stress. ... 100

Figure 5.29 Isochronal data for *Rab 12* on (a) linear and (b) log-log axes of strain vs. stress. . 100

Figure 5.30 Isochronal data for *Rab 13* on (a) linear and (b) log-log axes of strain vs. stress. . 101

Figure 5.31 Isochronal data for *Rab 15* on (a) linear and (b) log-log axes of strain vs. stress. . 101

Figure 5.32 *Rab 8* - Strain vs. stress prediction for (a) linear viscoelastic and (b) QLV model. 102

Figure 5.33 *Rab 9* - Strain vs. stress prediction for (a) linear viscoelastic and (b) QLV model. 103

Figure 5.34 *Rab 12* - Strain vs. stress prediction for (a) linear and (b) QLV model. 103

Figure 5.35 *Rab 13* - Strain vs. stress prediction for (a) linear and (b) QLV model. 104

Figure 5.36 *Rab 15* - Strain vs. stress prediction for (a) linear and (b) QLV model. 104

Figure 5.37 Data showing consistent decrease in compliance between consecutive steps. 107

Figure 5.38 Data showing general trend of decreasing compliance despite variability. 108

Figure 5.39 Data showing gross decrease in creep strain over extended number of steps. 108

Figure 5.40 Data showing gross decrease in recovery strain over extended number of steps... 109

Figure 5.41 Percent error between first two creep steps versus time..... 110

Figure 5.42 Percent error versus initial creep compliance..... 111

Figure 5.43 Photomicrograph (21x mag.) showing presence of droplets after three days. 112

Figure 5.44 Photomicrographs (10x mag.) showing increase in droplet quantity with time.... 112

Figure 5.45 Photomicrograph (40x mag.) showing droplets and rod-like entities. 113

Figure 5.46 FEA model (a) mesh and (b) temperature distribution in specimen and cone. 114

Figure 5.47 Results of the temperature ramp-up creep testing. 115

Figure 5.48 Results of the temperature ramp-down creep testing. 115

Figure 5.49 Results of the temperature ramp-up, ramp-down creep testing. 116

Figure 5.50 Representative creep data on axes of strain vs. time using mineral oil. 117

Figure 5.51 Representative recovery data on axes of strain vs. time using mineral oil..... 117

Figure 5.52 Representative creep data on strain vs. time axes using humidity chamber. 118

Figure 5.53 Representative recovery data on strain vs. time axes using humidity chamber. 119

Figure 6.1 Log-log strain vs. time plot. Log-log slope is approx. equal for all stresses. 123

Figure 6.2 Photograph of cone and plate while testing with humidity chamber. 136

Figure 6.3 Photograph of the humidity chamber in operation during testing of specimen. 137

Figure A.1 Andrade creep parameter determination (a) and determination of viscosity, η (b). 142

Figure A.2 Experimental and recoverable compliance plotted against the cube root of time. .. 143

Figure A.3 Viscous contribution to deformation. Viscosity is obtained from inverse slope.... 144

Figure A.4 Linear regression fits to data on J(t) vs t^1/3 axes. 145

Figure A.5 Manually and computer determined viscosity values for Andrade creep model. ... 145

Figure A.6 *Rab 8* - Actual and predicted recovery of manual (a) and computer (b) fit creep.... 146

Figure A.7 *Rab 9* - Actual and predicted recovery of manual (a) and computer (b) fit creep.... 146

Figure A.8 *Rab 12* - Actual and predicted recovery of manual (a) and computer (b) fit creep.. 147

Figure A.9 *Rab 13* - Actual and predicted recovery of manual (a) and computer (b) fit creep.. 147

Figure A.10 *Rab 15* - Actual and predicted recovery of manual (a) and computer (b) fit creep.148

Figure C.11 Post-yield mending testing plot for specimen tested using mineral oil. 152

Figure C.12 Post-yield mending plot for specimen tested with humidity chamber..... 152

Figure D.13 Compliance versus time plot of 6 Pa creep data and general constitutive model. . 154

Figure E.14 Log-Log plot of compliance versus time showing dehydration testing results. 156

Figure E.15 Plot of creep tests performed at increasing levels of hydration. 157

Figure E.16 Master curve constructed from Figure E.15 by shifting along time axis. 158

ACKNOWLEDGEMENTS

Upon the successful completion of this research endeavor, I'm thankful to all those individuals that supported my efforts. I am grateful to my advisor Prof. Smolinski and co-advisors, Prof. Gilbertson and Prof. Plazek, for their patience and guidance. Thank you, also, Prof. Plazek for the many discussions we had regarding viscoelasticity and especially for your availability. It is a wonder how you, being retired, tended to be so accessible. It has truly been an honor to work under you. Thank you Kevin Bell for the countless times you provided support, guidance, and suggestions in numerous ways. You are a tremendous asset to the Ferguson Laboratory. I feel immense gratitude for the support and encouragement provided by my loving fiancée Debra. I am indebted to you for the many sacrifices you made and countless times you served as a sounding board while I was undergoing this task. I'm also grateful for the support of my parents who contributed in too many ways to cite specific examples. My grandmother, Dolores, deserves recognition since it was her personal experience with a herniated disc that motivated me to perform this research. In addition, this work serves as a tribute to my late grandfather, Joseph, whose example and ideals inspired a hard work ethic within me. I'm thankful to Donald Sentner and Justin D'Antonio for their respective contributions to the construction and development of the prototype humidity chamber. To Glinda, Brittany, and the Mechanical Engineering Department as a whole, thank you for your encouragement, patience, and support in the many forms it was afforded to me. I'm appreciative of Gianluca Vadalà and Dr. James Larson for their contributions in harvesting specimens. I thank The Pittsburgh Foundation: Albert B. Ferguson, Jr. M.D. Orthopaedic Fund and Freddie H. Fu, M.D., D.Sc. for financial support of this research. Last, but certainly not least of all, I thank God for all the blessings in my life that have enabled me to accomplish this feat.

LIST OF ABBREVIATIONS

Adjusted coefficient of multiple determination[++]	R^2_{adj}
Annulus fibrosus	AF
Cartilaginous endplate	CE
Coefficient of multiple determination[++]	R^2
Finite element analysis	FEA
Food and Drug Administration	FDA
Glycosaminoglycan	GAG
Institutional Animal Care and Use Committees	IACUC
Intervertebral disc	IVD
Intervertebral disc degeneration	IDD
Magnetic resonance	MR
Multivariate analysis of variance	M-ANOVA
Nucleus pulposus	NP
Polyethylene glycol	PEG
Polymethylmethacrylate or acrylic glass	PMMA
Quasilinear viscoelasticity	QLV
Radiography	X-ray
Sum of squared error[++]	SSE

[++] Definitions of statistical parameters, R^2, R^2_{adj}, and SSE are provided in Appendix F.

1.0 INTRODUCTION

The intervertebral disc (IVD) is a tissue structure located between the vertebrae of the spine, which serves to join the adjacent vertebrae while allowing relative motion to occur between them. It also serves as a cushion or shock absorber, reducing the transmission of impact loads and vibrations along the spinal column. As a result, the IVD serves several necessary and important functions within the bodies of humans and animals. Unfortunately, the IVD is subject to degeneration over time; a condition referred to as intervertebral disc degeneration (IDD). Each year, millions of people worldwide are affected by IDD. Current treatments for severe cases of IDD are fusion or more recently arthroplasty, which are invasive techniques involving surgery. Research is now being done on tissue engineering treatments such as gene therapy using animal models of IDD. Different methods, such as MRI, X-ray, histology, and mechanical testing are used to determine treatment efficacy. Mechanical testing is done to assess the biomechanical behavior of treated specimens, since load-bearing performance is an important outcome measure. Small animal models of IDD have been developed for research for both economical and ethical reasons. However, a difficulty in the use of small animal models is small size of tissue samples. Testing obstacles associated with size, such as fixturing complexity, may produce poor experimental data so careful consideration is required when choosing testing methods and equipment.

Different mechanical testing techniques yield different results and much debate has occurred over the appropriate method. Difference of opinion has also occurred regarding load application,

such as torsional versus compressive loading. This stems mainly from the biomechanical behavior of the IVD, which is viscoelastic in nature. In the most general sense, a viscoelastic material is a material that behaves neither as a purely elastic solid, nor as a purely viscous fluid, but rather possesses behavioral traits from each of these ideal material types. Common techniques for studying viscoelastic materials include creep, stress-relaxation and dynamic testing. Over the course of the scientific development relating to viscoelastic materials, constitutive models have been created to describe or predict the behavior of these materials. A famous model arriving early in the study of viscoelasticity is the Andrade creep model, which has successfully been used to describe the aggregate creep behavior of numerous viscoelastic materials.

Ultimately, as tissue engineering treatments for IDD are further developed, there is need to comprehensively evaluate treatment effectiveness. Of the multiple ways to measure treatment efficacy, the information available from mechanical testing is particularly sparse for small animal models of IDD due to testing complexities. Within the area of mechanical testing, creep testing results are limited, although information obtained from this type of testing could provide valuable insight into understanding how to effectively treat IDD. Given the necessity of evaluating treatment effectiveness for small animal models of IDD, a viscoelastic model is needed to describe and predict the creep behavior of IVD tissue of small animals as an outcome measure for disc treatments. In the current study, healthy nucleus pulposus tissue taken from the rabbit IVD has been evaluated using torsional creep testing to characterize the viscoelastic behavior of the tissue. This is done to determine a constitutive model for evaluating the efficacy of treatments applied to a rabbit model of IDD. It is hypothesized that the Andrade creep model may be used to describe and predict the creep behavior of healthy rabbit nucleus pulposus tissue.

2.0 BACKGROUND

2.1 THE INTERVERTEBRAL DISC

2.1.1 Composition

The intervertebral disc is composed of three main components: the nucleus pulposus, annulus fibrosus, and the cartilaginous endplate. These components differ significantly in structure and function.

The nucleus pulposus (NP) is at the center of the IVD (Figure 2.1). It has a gelatinous, mucous-like consistency, with a milky-white appearance, often varying between opacity and translucence from one specimen to another.[1,2]* The nucleus pulposus is composed primarily of water, 70-90%, and its dry weight is composed of 25-60% proteoglycan, 10-20% collagen, and other minor constituents. The proteoglycan, a hydrophilic protein that readily absorbs water, is mainly of the aggregating type known as aggrecan that is found in cartilage, although other types may also be found in the NP.[3] Fine, loosely organized fibers comprise the collagen network, resulting in material isotropy.[3,4]

The annulus fibrosus (AF) surrounds the NP with an annular series of distinct fibrous laminations (lamellae) that transition radially from the nucleus periphery to outer annulus, producing the outer disc boundary.[1,3] The annulus fibrosus is composed primarily of water, 65-80%, and highly organized collagen. The dry weight of the outer AF is about 75-90% collagen

* Parenthetical references placed superior to the line of text refer to the bibliography.

and 10% proteoglycan while the inner AF is about 40-75% collagen and 20-30% proteoglycan.[3] The fibers within each lamination are unidirectional and oriented at an angle to the spinal axis that varies from 60º at the outer AF to 45º at the inner AF.[3] In any two adjacent lamellae, the fibers are oriented in opposite directions of one another (Figure 2.1), distinguishing each ply and contributing to the material anisotropy of the AF.[1]

At the boundary between the vertebral body and the IVD lies a thin layer of hyaline cartilage, comprising the cartilaginous endplate (CE).[3] Resembling articular cartilage, the cartilaginous endplate is comprised of 70-80% water and 7% of its dry weight is proteoglycan.[3] Similar to the AF, the CE varies in composition depending on radial position with an increase in collagen content and subsequent decrease in proteoglycan and water content as the outer edge is approached.[3]

Figure 2.1 Representations of the IVD with nucleus pulposus and annulus fibrosus.
At the left, the intact annulus fibrosus and nucleus pulposus may be seen. At the right, fiber orientation may be seen to alternate with each lamination of the annulus.

2.1.2 Biomechanics

The spinal motion segment; also known as the functional spinal unit, is composed of two vertebrae and the contained IVD. From the behavior of a single spinal motion segment, multiple segments may be combined to represent the behavior and motion of the entire spine.[3] The IVD allows motion in the functional spinal unit. It permits six degrees of freedom in motion; translation along three orthogonal axes and rotation about these three axes.[3] The tissue properties of the IVD vary with water content, resulting in complex mechanical behavior such as stiffness that varies depending on the applied load.[3]

Each component of the IVD contributes to its range of motion and mechanical behavior. The NP serves to support compressive or eccentric loads on the vertebral body through fluid pressurization.[4] Essentially, pressure resulting from an applied load presses outward on the surfaces surrounding the NP, causing the AF and CE to contain this pressure, as seen in Figure 2.2.[1] It is for this reason that the NP is often modeled as an incompressible fluid in finite element analysis (FEA) studies, although it has been suggested that a biphasic or poroelastic model is more appropriate.[3] The outward pressure applied to the AF predominantly causes hoop stresses along the circumference of the lamellae, placing the fibers of the AF in tension.[1,3] While the outer AF is in tension, axially as well as circumferentially, the inner AF bears some of the compressive loading axially (Figure 2.2).[1] It may be seen from the outer AF fiber angle of 60º that the hoop stresses are greater than the axial stresses in this region.[1,3]

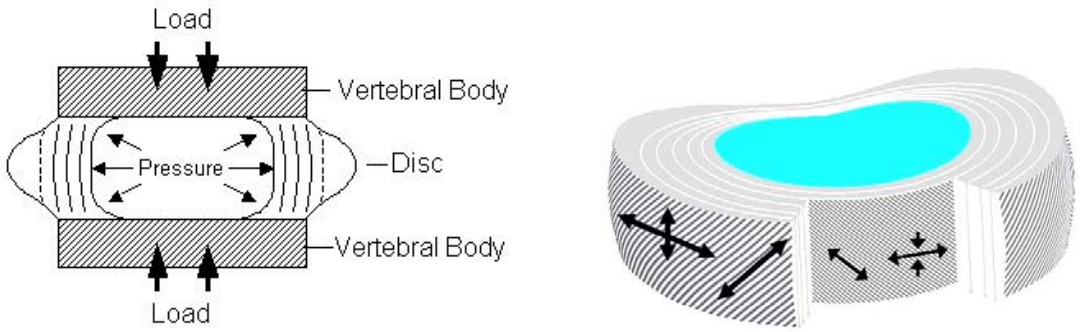

Figure 2.2 Compressive loading of the healthy IVD.
Arrows indicate approximate direction and magnitude. At left, the fluid-like nature of the NP is demonstrated by hydrostatic loading placed on the inner AF. At right, the fibers of both the inner and outer AF are in tension. Inner and outer circumferential stresses and outer axial stresses are also tensile. Inner axial stresses are of low magnitude and compressive. In a degenerate IVD, inner fibers are in compression, resulting in an altered stress state.[1]

The cartilaginous endplate attaches to the inner annulus such that it encloses the NP and the outer annulus attaches directly to bone of the adjacent vertebrae. The CE is a semi-permeable membrane that permits the flow of water, nutrients, and waste products to and from the NP and inner annulus. Studies have shown that it has an increased permeability over the annulus lamellae and a nonlinear directional dependence such that fluid enters the IVD through the CE more readily than it departs. This is shown through loss of disc height over 16 hours during the day and complete height recovery over 8 hours at night.[3]

2.1.3 Biochemistry of Proteoglycan and Collagen in the IVD

Collagen, a triple-helical protein that functions as the load-bearing constituent of the IVD, has been found in humans and animals to exist in at least 17 different forms.[5] The IVD contains at least seven of these types, although type I and type II are in dominant quantities. The AF contains mostly coarse type I collagen while the NP contains only the finer type II collagen. Cross-linking, which has been found in the disc between collagen molecules, occurs at points

along the fibrillar chains, providing strength and protection to the network.[5] The strength of the highly structured AF results from a dense collagen network, with the highest collagen density, 70-90%, occurring near the outer periphery. In contrast, the loose collagen network of the NP results in its gelatinous, fluent character.

Proteoglycan, a form of macromolecule containing a protein backbone with carbohydrate chains covalently bonded to it, makes up the other main (dry) constituent of the IVD.[5] Each carbohydrate chain, known as glycosaminoglycan (GAG), possesses a negative charge that is responsible for the fixed charge density of the IVD, an important property. The fixed charge density, directly resulting from the concentration of proteoglycans, controls the charged solutes distribution in the IVD, thus controlling the osmotic pressure of the IVD. The fixed charge density of adult NP produces an osmotic pressure of between 0.1 to 0.3 MPa (about 1 to 3 atm), depending on age.[5] It is through this mechanism that the proteoglycans imbibe water and create a swelling pressure, extending the collagen network and balancing applied loads.[6,7] Thus, although the water content of the disc varies throughout the day depending on load activity,[3,6] the ability to imbibe water and function normally is dependent on proteoglycan within the disk.[7,8] The proteoglycan content in the disc decreases with age. At this time, it is unclear if the decrease in content is due to an increased rate of proteoglycan decomposition, a reduced rate of proteoglycan synthesis, or a combination of both.[5,6,9]

2.1.4 Mechanical Testing of the Intervertebral Disc

Historically, mechanical testing has proven important in understanding the properties and constituents of materials; biological tissues included. Thus, the IVD has become the subject of numerous biomechanical tests in an attempt to gain further insight into the functional mechanical behavior of this structure. These studies have involved the IVD tissue of both humans and

animals, typically consisting of creep, relaxation, and dynamic testing methods. A broad overview of biomechanical testing of the IVD has been provided here to assess the current state of understanding and to highlight any deficiencies. Testing performed on the intact IVD is provided initially followed by testing performed on the individual components of the IVD.

An extensive number of studies have taken place investigating the biomechanical properties of the intact IVD. Equally numerous are the objectives that direct these studies, ranging from characterization of disc biomechanical function to studies that measure how load conditions influence synthesis rates or treatments within the disc. In general, these studies tend to provide details concerning the composite behavior of the IVD rather than information specific to one particular component. Table 2.1 summarizes biomechanical studies performed on the intact IVD.

Table 2.1 Biomechanical testing of the intact intervertebral disc.[10-30]

Testing Method	Testing Type	Tissue Source	Model or Objective	Lead Author
Creep	Compression	Human	Viscoelastic	Koeller, W
Creep	Compression	Mouse		Palmer, EI
Creep†	Compression	Mouse	Other	Chin, JR
Creep	Compression	Human		Burns, ML
Creep	Compression	Pig (Porcine)	Viscoelastic	Keller, TS
Creep	Compression	Human	Viscoelastic	Kazarian, LE
Creep	Compression	Human	Frozen Storage	Dhillon, N
Dynamic	Compression	Rabbit		Kroeber, MW
Dynamic	Compression	Rat		MacLean, JJ
Dynamic	Compression	Rat		Ching, CT
Dynamic	Compression	Murine (Mouse)	Proteoglycan Synth	Walsh, AJ
Dynamic	Compression	Sheep (Ovine)	Elastic/Viscoelastic	Johannessen, W
Dynamic/Creep	Compression	Human		Koeller, W
Relaxation	Tension	Human	Viscoelastic	Panagiotacopulos, ND
Relaxation/Creep	Torsion	Monkey	Viscoelastic	Kelley, BS
Other	Torsion	Rat and Mouse	Other	Elliot, DM[25]
Other	Compression	Rat and Mouse	Other	Elliot, DM[25]
Other	Compression	Mouse	Structural Breakdown	Lotz, JC
Other	Compression	Rat	Immobilization Effects	Iatridis, JC
Other	Compression	Porcine	Other	Ohshima, H
Other	Bending	Mouse	Loading on Cell Funct	Court, C
Other	Hydration	Human	Loading Effects on Hyd	McMillan, DW

The table indicates that testing procedures tend to be one of the three traditional methods for studying viscoelastic materials: creep, relaxation, or dynamic testing. The dominance of compression loading over other methods such as torsion, flexion, or extension, may result from attempts to test the IVD and motion segment under loading conditions representative of basic daily function, such as supporting upper body weight. Still, some researchers argue that compression loading combined with either torsion or flexion may be more appropriate in representing daily loading conditions.[31] Although testing has been performed on both human

† Study involving mechanical testing where determination of mechanical properties is known not to be the objective.

and animal specimens, economic and ethical considerations tend to result in the majority of the available data coming from animals.[32]

Attempts have also been made to characterize the behavior of the individual tissue structures within the IVD. Individual testing of IVD components eliminates behavior associated with the composite structure of the IVD, generally providing insight into the specific function of the tissue structure being studied. Although the objectives for performing this type of testing may be as numerous as the objectives for testing the intact IVD, it appears that there are fewer overall data available regarding biomechanical testing of the individual components. This deficiency applies particularly to small animal specimens such as the rabbit, where individual testing of IVD components is made difficult due to the complexity of working with small specimens. Tables 2.2, 2.3 and 2.4 provide a summary of the testing performed on NP, AF, and CE tissues, respectively.

Table 2.2 Biomechanical testing of the nucleus pulposus.[4, 33 – 38]

Testing Method	Testing Type	Tissue Source	Model	Lead Author
Creep	Compression	Dog (Canine)	Viscoelastic	Bradford, DS
Creep	Torsion	Pig (Porcine)	Elastic/Viscoelastic	Van Deursen, DL
Dynamic	Hydrostatic	Rabbit	Loading Frequency Effects	Kasra, M
Relaxation/Dynamic	Torsion	Human	Linear Viscoelastic	Iatridis, JC[4]
Relaxation/Dynamic	Torsion	Human	Viscoelastic	Iatridis, JC[36]
Relaxation/Dynamic	Torsion	Human	Viscoelastic(Aged/Degenerate)	Iatridis, JC[37]
Other	Compression	Human	Other	Urban, JP

Table 2.3 Biomechanical testing of the annulus fibrosus.[34,35,39-44]

Testing Method	Testing Type	Tissue Source	Model	Lead Author
Creep	Torsion	Pig (Porcine)	Elastic/Viscoelastic	Van Deursen, DL
Dynamic	Hydrostatic	Rabbit	Loading Frequency Effects	Kasra, M
Dynamic	Tension	Rabbit	Proteoglycan Synth	Rannou, F
Relaxation/Dynamic	Torsion	Human	Viscoelastic	Iatridis, JC
Relaxation	Compression	Human	Viscoelastic/Biphasic	Iatridis, JC
Relaxation	Tension	Dog (Canine)	Viscoelastic	Huyghe, JM
Constant Strain Rate	Tension	Human	Elastic	Ebara, S
Quasi-static	Tension	Human	Quasi-static	Acaroglu, ER

Table 2.4 Biomechanical testing of the cartilaginous endplate.[45-47]

Testing Method	Testing Type	Tissue Source	Model	Lead Author
Creep	Compression	Baboon	Viscoelastic	Setton, LA
Creep	Compression	Bovine		Van Dieen, JH
Dynamic	Compression	Pig (Porcine)	Other	Ishihara, H

In Table 2.2, it should be noted that testing of the NP has been performed on porcine specimens and human specimens using torsional creep testing and relaxation testing, respectively. While some debate surrounds the appropriate method of testing in order to simulate physiological loading conditions, if the testing objective is characterization of the material in an attempt to create a constitutive model, torsional loading is perhaps a more appropriate choice.[3,36] In simple shear loading, which is approximated by torsional loading, volume is conserved and poroelastic effects[48,49] associated with water migration may be ignored. No previous studies could be located where the focus of the research was torsional creep testing on small animal specimens. While some biomechanical testing has been performed on the AF of small animal specimens, as evidenced in Table 2.3, this information is also limited and no studies could be located involving torsional creep testing. In Table 2.4, it may also be

seen that small animal specimens are absent from data published regarding the biomechanical testing of the CE.

2.2 INTERVERTEBRAL DISC DEGENERATION

2.2.1 Overview and Impact

The intervertebral disc is the largest avascular organ in the human body.[50] With blood supply only available at the periphery, passage of nutrients and waste must take place primarily through diffusion.[3] Motion of the spine also aids in supplying nutrients due to fluid currents created through pumping that takes place as the tissues change shape and volume.[51] This difficult process through which nutrients must be delivered and waste products removed results in a slow regenerative and healing process within the IVD. The onset of disc degeneration occurs when the synthesis rate of matrix proteins and new tissue growth is consistently inadequate in exceeding the rate of cell death and tissue breakdown.[9,52] It has been shown that degeneration of the IVD leads to degeneration of adjacent spinal components and reduced integrity of the spinal motion segment overall.[51,52] Painful IDD may be referred to as a disease since it results in "disability and dysfunction."[52] Thus, the disease state of IDD is defined as "loss of structural and functional integrity of the disc, associated with pain and discomfort."[53]

People all over the world are affected, both directly and indirectly, by back pain attributed to IDD. The impact of IDD may be traced from the individual experiencing reoccurring pain and discomfort, through the employer and healthcare provider affected by lost work and healthcare expenses, respectively, to the healthcare consumer who is ultimately affected by increasing costs

of healthcare coverage. For over 60 years, the highest frequency of musculoskeletal disorders reported has been due to the lower back. Indeed, this has had significant impacts on health care costs and employment compensation claims in that time. Back pain is one of the leading causes for people to obtain medical attention, second only to the common cold.[54] Reports indicate that low back symptoms account for over 14% of first-time visits to physicians.[54] During the course of a year, one study found that spinal and back disorders resulted in the occurrence of over 185 million days of restricted activity; accounting for nearly half of the total number of restricted activity days due to musculoskeletal impairment.[54] Consequently, back pain and problems associated with the IVD may require intervention in order for people to return to work or may it necessitate a job change altogether. IDD is estimated to account directly or consequentially for 90% of surgical spine procedures.[9] With over 30% of compensation payments in the US attributed to lower-back related injuries and considering the economic consequences resulting from lost time and medical costs, the impact of IDD is staggering.[54]

2.2.2 General Features of IDD

Primary degeneration of the IVD is a type of degeneration that occurs as a natural part of the aging process and is a common occurrence among all biological tissues.[6,53] As age increases, the composition of the disc changes as well, and it is believed that these changes precede biomechanical changes in the IVD.[9] Notably, water and proteoglycan content decreases in the NP. At birth, the hydration of the NP may be as high as 90%, while it decreases to near 70% in adults.[3,5,8] The annulus fibrosus remains relatively constant in comparison.[5,53,54,55] The decrease in hydration of the NP is most likely a result of the decrease in proteoglycan content, which decreases from 60% at birth (dry weight) to below 20% beyond middle age.[3,8,53] Decreased water in the IVD results in decreased synthesis rates of proteoglycan, limiting the

ability of the IVD to imbibe water,[8] which perpetuates the degenerative process by further reducing the ability of the IVD to regenerate over time. Particularly with the decrease in concentration of proteoglycan, aggrecan content diminishes significantly,[5] thus limiting the aggregating ability and ensuing molecular weight of the proteoglycan within the NP.[52] It is also believed that the cross-linking ability of collagen is altered since an increased number of collagen cross-links may be observed with age.[52] The resulting degenerated NP is more fibrous and the AF and NP begin to integrate into one another (i.e., become less clearly defined), extensively obscuring the boundary that separates the two components.[51,52] In addition to the collective changes in the NP and AF, thickness irregularity and calcification of the CE has also been noted.[51]

In association with the biochemical changes in the IVD, biomechanical changes occur in the IVD and motion segment as well (e.g., reduced motion segment stability).[6,9] As dehydration in the NP becomes more significant with age, subsequent narrowing of the disc (i.e., reduced disc height) is observed along with increased circumferential bulging of the AF.[52,55] Stiffening of the NP and reduced pressurization[9] accompanies the transition from fluidlike to solidlike behavior, contributing to reduced disc height.[55] In the AF, circumferential tears initiating between adjacent lamellae result in radial tears that traverse inter-laminar boundaries and penetrate the nucleus.[52,53] Figure 2.3 represents a healthy disc and several physical features of IDD.

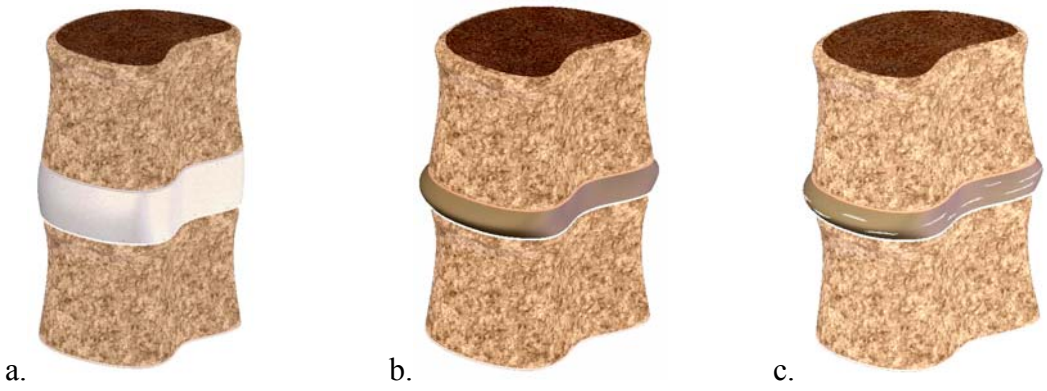

Figure 2.3 Representations of IDD features.
Comparative representations of a healthy disc to discs exhibiting features of IDD are provided as follows: (a) healthy disc, (b) reduced height and bulging, (c) annular lesions.

Secondary degeneration of the IVD represents degenerative changes similar to those of primary degeneration, but the changes occur at an accelerated rate and possibly on a larger scale. It appears that secondary degeneration is a degenerative mechanism that is "triggered" as a result of mechanical or other influences. Although the initiating events and influences are unclear,[9] a number of potential triggers or risk factors for secondary degeneration have been identified that, neglecting age, may increase the likelihood for IDD to occur in an individual. For example, potential risk factors include trauma, high spinal loadings, excessive vibration exposure, immobility, poor posture, and chemical influences such as smoking and alcohol.[53,54] It is also believed that certain individuals may be more susceptible to IDD as a result of genetic predisposition.

In spite of the uncertainty relating to the pathogenesis of secondary degeneration, two possible mechanically influenced pathways have been identified, suggesting direct and indirect processes. Damage resulting from applied loads and strains such as hyperflexion constitute the direct process, while weakening of disc properties in response to certain loading conditions (e.g.,

poor posture, immobilization) constitutes the indirect process.[51] In this way, both excessive loading and immobilization may contribute to secondary IDD. The former mechanism is due to acute or accrued damage of the tissue while the latter may result from a decrease in proteoglycan and collagen production.[51] The plausibility of mechanical damage resulting in degeneration is somewhat obvious. Recently, however, studies have shown that a number of factors negatively affect proteoglycan synthesis such as a lack of mechanical stimulus and nutrition, supporting the argument that immobilization may also contribute to degeneration.[6,51] Studies of the working population revealed a prevalence of increased degeneration among individuals performing heavy physical labor as well as women employees filling sedentary positions.[53] These types of studies, however, do not account for levels of activity outside of work, which is likely to introduce some error into the results. Although certain athletic activities that produce high spinal impact loads or twisting may increase the chance of premature degeneration,[53] it has been shown that people of good physical fitness tend to have lower occurrences of back pain than those leading sedentary lifestyles.[51] In support of these findings, laboratory studies have demonstrated that stimulated production of collagen and proteoglycan may occur at low levels of compression, pressurization, and vibration while higher magnitudes inhibit production.[51] Thus, it appears that a range of loading activity is required to maintain disc health. In spite of this, limited knowledge is currently available in regard to the signaled cellular production of proteoglycan and collagen as a result of mechanical stimuli[51] and further study is required to understand the mechanisms of secondary degeneration.

Primary and secondary degeneration usually occur in parallel, significantly complicating the epidemiology (i.e., study of the progression) of IDD in humans.[3,53] Further, it is difficult to distinguish between inflammatory, traumatic, and age-related degeneration, except possibly

through the resultant healing that is complicated and retarded by the avascularity of the structure.[55] Although some believe IDD begins in the NP and progresses to the AF, counter-evidence indicates that events occurring in the AF may instigate degeneration as well.[55] This obscures the understanding of IDD as multiple and possibly compound mechanisms may initiate its progression, creating the need for more numerous treatments that compliment each degeneration mechanism.

Consequent clinical problems, such as disc herniation, can result from IDD.[9] Disc herniation occurs when the NP is forced partially or fully through a rupture in the AF or the CE, and may become painful particularly when the herniated IVD material intersects the spinal cord.[56] An example of annular herniation is depicted in Figure 2.4. Studies have shown that annular herniation will not occur due to annular compression failure in normal healthy discs, as the AF will contain the NP, even under substantial loads. However, if the IVD is altered and both the NP and AF are abnormal, it is possible that the AF will rupture and the NP will extrude through.[57] Herniation is most likely to occur in middle age while the NP retains some of its fluid-like properties, even though the disc has changed due to IDD.[55] It is believed that this age group is most susceptible to herniation since, during this period of life, the disc is in a transient degenerative stage between well hydrated and relatively dry.[53] The disc fragments of herniation patients from 35 to 45 years of age appear markedly more aged than healthy discs from the same age group.[52,53] For this reason, herniation and alterations to the end-plate are not generally correlated with aging[53] but usually result instead from the secondary degenerative process. Among this age group, professional workers tend to be less likely to experience herniation than laborers and vehicle operators.[53] This may either be due to a reduced risk of traumatic events occurring or a dearth of loads that aggravate degeneration.

Figure 2.4 Depiction of annular herniation.

2.2.3 Pain attributed to IDD

Studies have concluded that low back pain in patients less than 40 years of age may be correlated with degeneration.[52] However, whether or not the degenerative process is a direct source of pain is unknown.[9] Since changes to the IVD may not necessarily result in pain, researchers are confounded as to the true source of the pain.[52,53] It is believed that the pain may result from pressures on adjacent structures due to bulging discs and disc herniation, chemical inflammation produced by breakdown products that "leak" from the IVD, or other modes of mechanical irritation to the nerves at the periphery of the outer AF.[52] While a correlation cannot be made between general features of IDD and pain, tears in the outer AF were shown to be a common observance in painful, symptomatic discs, supporting the belief that some pain may stem from the innervated outer annulus.[53] Nonetheless, given the poorly understood relationship between the degenerative process and clinical symptoms,[9] the need for further studies relating pain to IDD is evident.

2.2.4 Animal models of IDD

Animal models have traditionally been used in medical research as an economic and ethical alternative to the study of humans. Some of the earliest animal models of IDD utilized rabbits and typically involved surgically induced trauma to the AF, which may have or may not have penetrated the NP.[50] If the NP were penetrated during this type of procedure, prolapse of the NP would immediately result.[50,58] Secondary degenerative changes were noted following such studies where acute disc herniation was present. Specifically, a gradual loss of proteoglycans and subsequent dehydration was detected.[50] Similar changes were noted in studies limited to partial penetration of the AF, which suggests these degenerative changes were triggered by the traumatic event, in general, rather than the specifics of the IVD injury.[50] Spontaneous degeneration models are also useful to the study of IDD. To better understand spontaneous degeneration mechanisms, models utilizing animals that are seemingly predisposed to disk degeneration such as the canine breed that includes the basset hound and dachshund have been studied.[50] In addition to the study of disease pathomechanisms, animal models provide bases for measuring tissue properties, evaluating IDD treatments, and studying IVD matrix interactions.[9,32] Thus, the objective has become the development of specific, reproducible degeneration models in order to reduce the number of variables associated with the degeneration process, particularly if these models are to be used as a platform for studying IDD treatments rather than the progression of IDD itself.

A number of factors are involved in the selection of appropriate animal models for IDD. These factors generally depend on the availability of the animal, issues related to handling and care of the animal during experimentation, and similarities between the animal and humans from an anatomical and physiological perspective.[50] However, compromises are necessary since no

model is ideal and the relevance of a model to humans must be justified. Convenient size, reduced care cost, and imaging capability are strengths of existing small animal models such as rats and rabbits.[9,32] Further, allometric scaling (i.e., scaling of organism proportions due to growth) of disc geometry from one species to another is directly proportional to the one-fourth power of body mass, allowing extrapolation from small animal models to human discs.[32] Of particular interest to the current study, a reproducible model of IDD has been developed in rabbits using a partial penetration annular stab with a 16-gauge hypodermic needle.[59] Using magnetic resonance (MR) imaging, radiography (x-ray), and histological indicators, this model has been shown to produce progressive degenerative changes in the rabbit IVD similar to those seen in humans.[59] At present, supplemental studies and development of "infrastructure" (e.g., custom MR imaging devices for rabbits) are underway, intended to facilitate this model as a platform for the study of novel, minimally invasive tissue engineering treatments.

2.2.5 Treatments of IDD

Given the major clinical problem that IDD presents, numerous treatments are currently in place to address this issue. However, the treatments in practice today are commonly aimed at treating and correcting secondary effects associated with IDD rather than slowing the progression of IDD or producing regenerative mechanisms to restore disc health.[59] Conservative, non-surgical treatments such as forms of physical and traction therapy are often prescribed as an initial measure.[52] In one study, the majority of herniation patients (63%) subjected to conservative forms of treatment such as traction therapy experienced herniation recession.[53] In the event that conservative treatments are ineffective, surgical techniques such as spinal fusion or disc arthroplasty may be employed.[9,52] Fusion has been the mainstay procedure for nearly a century and consists of removing the degenerated disc (discectomy) and fusing the two adjacent

vertebrae together.[60] A shortcoming of this invasive technique is that it reduces mobility and transfers stresses to the adjacent discs, which may potentially cause accelerated failure of the adjacent discs in turn.[60] Disc arthroplasty involves replacing a faulty disc with a prosthetic disc, thus preserving the motion capabilities of the original disc.[9] However, disc arthroplasty is also an invasive procedure and issues relating to device wear and compatibility with the surrounding tissue present other shortcomings. With the exception of clinical trials, disc arthroplasty procedures are uncommon, particularly in the United States as many of these devices await approval by the Food and Drug Administration (FDA).[59,60]

The development of minimally invasive treatments aimed at halting the progression of IDD and regenerating the disc are expected to reduce medical costs, recovery time and post-treatment restriction, thereby reducing economic and employer compensatory impact, and improving quality of life as an end result. Some examples of novel, minimally invasive tissue engineering treatments currently under development include gene therapy, molecular therapy, cell therapy, application of growth factors, and biochemical therapy approaches.[9,61,62] These techniques show promise of slowing the degeneration process and prompting healing by altering the biological processes within the disc or interfering with the way the disc responds to mechanobiological events.[9] As an example of biochemical therapies, injections of tiaprofenic acid into the outer AF of a porcine model produced an increase of proteoglycans in the NP, demonstrating the ability to stimulate repair of the IVD.[50] Recently, molecular therapy approaches have also been shown to favorably alter the course of IDD in the rabbit model previously detailed in section 2.2.4.[63,64]

2.2.6 Evaluation of Treatment Efficacy

In order to determine the functionality of a tissue engineering treatment and compare the effectiveness of multiple treatments to one another, metrics of success are necessary. Treatments are applied to systems of living models, such as animal models of IDD, and relevant experimentation is performed in order to obtain outcome measure data. Typical experimental outcome measures include MR imaging, x-ray, computed tomography, histology, and gene expression.[9,59] MR imaging is the most feasible and commonly used method for IDD testing and prognosis.[9] It is capable of obtaining a measure of the water content of the NP, thus providing a quantifiable metric for evaluating biochemical alterations within the NP.[52,53] However, while MR imaging and the other success metrics indicated might be capable of determining water content, proteoglycan and collagen synthesis rates, or cell health, they are unable to provide information regarding whether the original biomechanical behavior of the disc tissue is restored. Thus, biomechanical function is another useful outcome measure for the study of treatment effectiveness. To this end, the establishment of databases and mathematical models[9] describing tissue behavior are needed to provide quantifiable, functional benchmarks of success for approaches to the treatment of IDD.[64]

2.3 VISCOELASTICITY

2.3.1 Foundational Work and Preliminaries

The theory of viscoelasticity is a relatively new science, with much of its advancement taking place in the second half of the last century. In 1878, Ludwig Boltzmann published his superposition principle as a fully general, integral statement of linear viscoelasticity.[65] This

would prove to be crucial to the development and understanding of viscoelastic theory and is now a fundamental principle. In 1910, E.N. da C. Andrade published "On the Viscous Flow in Metals, and Allied Phenomena," detailing the creep behavior of lead and establishing the first creep law.[66] The creep model presented in this work would later be used to describe the creep behavior of many other materials, from asphalt to amorphous polymers. In 1961, John D. Ferry published Viscoelastic Properties of Polymers, a work that remains a fundamental reference for studies in viscoelasticity to date. These works and the development of their underlying theory have been a necessity to the current study.

In order to understand the details of viscoelastic theory, certain preliminary variables and terminology must be introduced. Rheology, defined as the study of the deformation and flow of matter, is the science within which the study of viscoelastic solids and fluids may be classified.[67] In general, a viscoelastic material displays behavioral traits borrowing from both elastic solids and viscous fluids[68] and possesses a time-dependent deformation such that "the stress may depend on both the strain and the rate of strain together, as well as higher time derivatives of strain."[69] Further, these traits may vary, depending on testing conditions such temperature, although temperature dependence is not necessarily considered a defining requirement of viscoelastic materials.[70]

There are numerous ways to define the concept of strain. In general, strain is a measure of local deformation in a material defined as the ratio of the change in length of a dimensional parameter to the initial length of a reference dimensional parameter. For example, longitudinal (i.e., axial) strain is defined as the deformation of a stressed element in a particular direction divided by the original element length in the same direction.[71] Consider the stressed element in Figure 2.5a with original length represented by l_o and deformation represented by δ. The

longitudinal strain, ε, becomes $\varepsilon = \delta / l_o$. The result is a dimensionless parameter since units of *length / length* cancel. The stress, σ, applied to the element in Figure 2.5a is defined as a tensile stress.

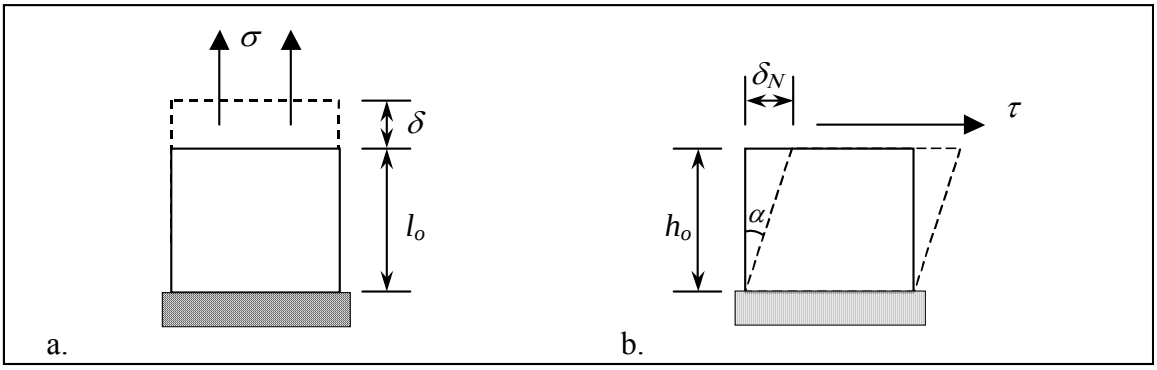

Figure 2.5 Depiction of longitudinal strain (a) and shear strain (b).
Solid element lines indicate the undeformed state. Dashed element lines indicate the deformed state.

Shear strain is defined as the ratio of orthogonal deformation in a stressed element to the original reference length of the element.[72] Consider the stressed element in Figure 2.5b with reference length represented by h_o, deformation in the direction normal to h_o (i.e., shear deformation) represented by δ_N, and the resulting right triangle with angle, α. The shear strain, γ, becomes $\gamma = \delta_N / h_o = \tan(\alpha)$.[69,72] Again, the result is a dimensionless parameter since units of *length / length* cancel. Note that for infinitesimal strains, tan(α) may be replaced by the angle, α, as is usually the case within the context of elasticity theory. However, caution must be exercised when using this assumption, as larger strains often associated with the study of viscoelastic materials will make it invalid. The stressed element in Figure 2.5b additionally depicts the condition of simple shear deformation, described by Ferry as "the most important type of deformation in studies of viscoelastic bodies"[69] since the volume remains constant under these

conditions and also due to the ability to deform both solids and fluids in this manner.[69] The lateral stress, τ, applied to the element in Figure 2.5b is defined as shear stress. It should be noted that substantial changes in the specimen dimensions must be compensated for when determining stress and strain[69] but this effect is minimized in torsional shear studies where the original dimensions are approximately constant.

The strain, stress and time data obtained through specific experiments performed on viscoelastic materials are often presented in terms of variables related to the type of experiment. The creep compliance, determined using the creep method of testing, is defined as the time-dependent strain divided by the constant applied stress. Likewise, the relaxation modulus produced by the stress relaxation method of testing, is defined as the time-dependent stress divided by the constant applied strain.[73] Additional details pertaining to methods of testing viscoelastic materials are supplied in Section 2.3.3.

As a final point, it is worth mentioning the use of physical models in the development of viscoelastic theory. Early studies of viscoelasticity often involved representing materials as spring-damper combinations to aid in visualization of the material response mechanism.[69] However, it is difficult to ascertain physical insight about features of complex materials from such spring-damper models[73] so this treatment will be avoided in the current context.

2.3.2 Viscoelastic Solids and Viscoelastic Fluids

Viscoelastic materials may usually be separated into two subgroups, viscoelastic solids and viscoelastic fluids. A viscoelastic solid is a material that, while undergoing creep deformation, reaches an equilibrium strain such that the rate of deformation ceases in time.[70] In this case, the creep rate or strain rate is zero. This behavior is depicted on a plot of strain versus time in Figure

2.6a. A common example of a viscoelastic solid is a cross-linked polymer. In this type of material, an equilibrium strain is reached when the random polymer chains have been stretched to their maximum orientation and the cross-links will not permit the chains from slipping passed one another.[70] A viscoelastic fluid is a material that, while undergoing creep deformation, reaches a point in time when the deformation occurs at a constant velocity. Thus, a steady creep rate (or strain rate) has been reached. This behavior is plotted on axes of strain versus time in Figure 2.6b. A common example of a viscoelastic fluid is an amorphous polymer, where no cross-linking occurs between the polymer chains. Thus, as the polymer chains are deformed from their random orientation to the fully oriented state, they begin to slip passed one another since nothing is present in the material to restrict this type of relative motion between chains.[69] A limiting recoverable strain per unit stress is reached, so that after steady state deformation is achieved, the recovery becomes independent of the time of creep.

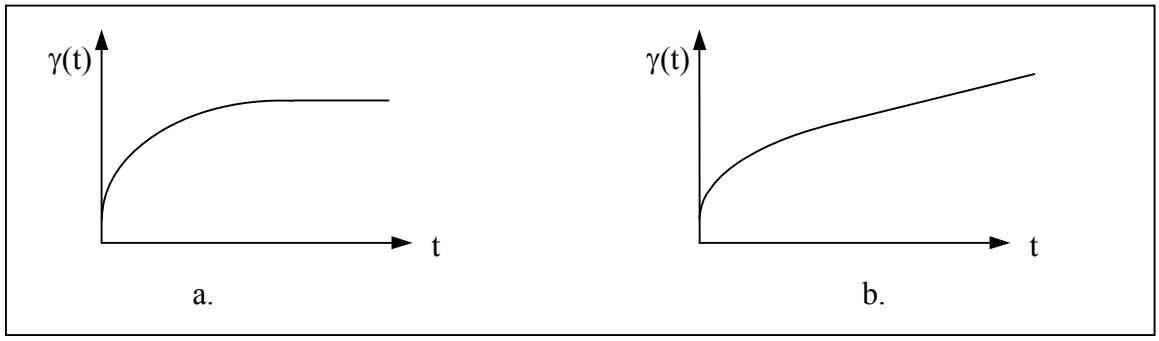

Figure 2.6 Ideal strain behavior of (a) viscoelastic solids and (b) viscoelastic fluids with time.

2.3.3 Common Mechanical Testing Techniques

In order to obtain information about the mechanical behavior of viscoelastic materials, it is necessary to perform experimental testing on these materials. Three types of mechanical testing techniques regularly performed on viscoelastic materials are creep testing, stress relaxation testing, and dynamic (oscillatory) testing. Understanding of these test methods is important since they are also common test methods for the biological specimens of interest to this study.

Creep testing consists of the "instantaneous" application of a stress that is held constant, such that material deformation occurs over time. The stress application termed "instantaneous" is an idealization but should occur in the shortest period of time permitted by the test instrument, usually on the order of 10^{-3} to 10^{-2} seconds.[69] Experimental creep results are typically provided in terms of compliance, a time-dependent ratio of strain to stress.[69] Specifically relating to shear creep experiments, the shear creep compliance, J(t), is expressed as,

$$J(t) = \frac{\gamma(t)}{\tau}, \tag{2.1}$$

where $\gamma(t)$ is the time-dependent shear strain and τ is the constant applied shear stress.

Upon the completion of the creep portion of the experiment, the recovery step follows. In the recovery step, the constant stress of the creep experiment is removed and the material is permitted to return to its original unoriented or maximum entropy state. Portrayal of a creep and recovery step for viscoelastic solid is provided in Figure 2.7a.

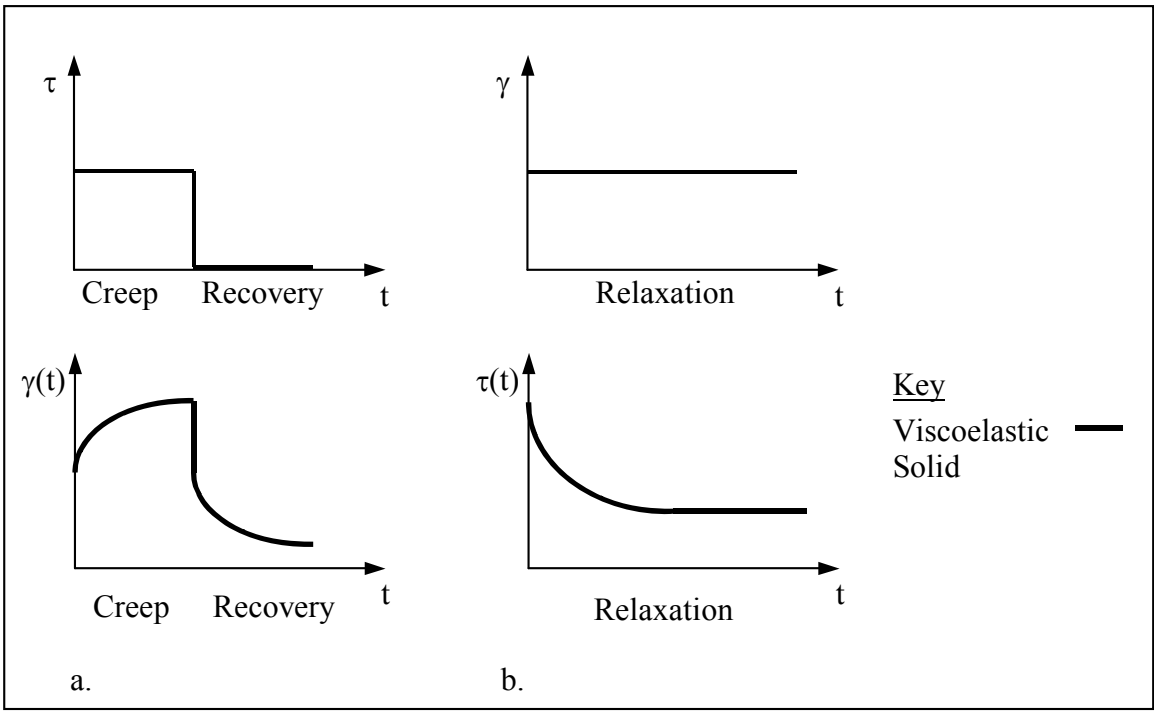

Figure 2.7 Typical behavior of a viscoelastic solid in (a) creep and (b) stress relaxation.[73]

Depending on whether the material is a viscoelastic solid or fluid, the recovery may or may not fully return the specimen to its original shape prior to the application of stress. Fully recoverable deformation, characteristic of viscoelastic solids, is deformation incurred during an experiment that returns to zero strain at the completion of the recovery step.[70] Non-recoverable (permanent) deformation is deformation incurred during the creep portion of an experiment that remains a finite strain after the recovery step has taken place and the recovery strain rate has essentially decayed to zero. For a linear viscoelastic fluid, the non-recoverable deformation, J_η, increases linearly with the time of creep as $J_\eta = t/\eta$, where η is the shear viscosity. A viscoelastic material that possesses some fluid-like properties will have a tendency to incur permanent deformation.

Stress relaxation testing consists of the "instantaneous" application of a constant deformation and the resulting stress is measured over time. In general, the required stress for maintaining this deformation decays monotonically in time for viscoelastic materials.[70] Typical stress relaxation behavior of a viscoelastic solid is depicted in Figure 2.7b. At long times, the equilibrium stress level achieves a positive finite value for viscoelastic solids and decays to zero for viscoelastic fluids.[70] Specifically relating to shear stress relaxation experiments, the shear relaxation modulus is expressed as G(t), which is the time-dependent ratio of stress to strain. However, the shear creep compliance is generally not equal to the inverse of the shear stress relaxation modulus since the load application is different in time.[69,70] Rather, specific interrelations exist that relate these and other quantitative measures for viscoelastic materials.[69]

Although there is some overlap between testing methods and each should theoretically be capable of fully characterizing the viscoelastic response of a material, each method invariably has shortcomings.[70] During the creep experiment, the near-instantaneous application of the stress initially results in creep ringing, which is essentially an oscillation of the material due to inertial effects. It is for this reason that creep data collected prior to one second of test time is often discarded, as the creep ringing produces inaccuracies in the creep response of the material.[69] Stress-relaxation testing suffers from similar limitations due to inertial effects. In addition, departure from linear viscoelasticity and ultimate failure of the material are long-time limitations of creep and stress-relaxation testing.[69] As Ferry stated, "creep and stress relaxation experiments are limited only by the patience of the investigator, the precision of his apparatus, and the chemical stability of the material; they are always preferred for effects at long times."[69]

The objective of dynamic testing is to characterize a material at very short times in order to supplement long-time information about the material obtained through creep or stress relaxation

testing.[69,70] Unlike the transient loading that is applied to a material during creep and stress relaxation testing, dynamic testing requires that periodic loading be applied to a material, during which time the inertia of the entire instrument-specimen system is accounted for to obtain the material response.[74] Depending on the testing frequency, the stress oscillates sinusoidally to yield the maximum energy stored per cycle and the energy dissipated per cycle. The storage compliance, $J'(\omega)$, represents the maximum energy stored per cycle while the loss compliance, $J''(\omega)$, represents the energy dissipated per cycle. Summed together, J' and J'' make up the real and imaginary components, respectively, of the complex shear compliance, $J^* = J' - iJ''$.[70] It may also be shown that $J^* = 1/G^*$, where $G^* = G' + iG''$ is the complex shear modulus. Again, interrelations of the Boltzmann superposition principle must be used to obtain G(t) and J(t) from these dynamic parameters.[70]

2.3.4 Linear Viscoelasticity

Identification of the range of linear viscoelastic response is important in that interrelations exist within this range associating functions such as the creep compliance to the relaxation modulus.[75] This permits the comparison and interpretation of data collected using different experimental methods, which proves useful for materials like nucleus pulposus tissue that has been tested mainly through techniques other than creep. In turn, analysis of a material is simplified within the linear range. With this in mind, it may be desirable to approximate the behavior of a nonlinear material as linearly viscoelastic under certain circumstances, as in the case of amorphous high polymers.[75] Although nonlinear effects may generally be neglected if the stresses are sufficiently small,[69] this does not always suit the experimental objectives.

Nonetheless, understanding of linear viscoelasticity is necessary in that it provides a fundamental basis for progression to the theory of nonlinear viscoelasticity.[72]

The simplest expression of linearity in a viscoelastic material is adherence to the Boltzmann superposition principle.[70] In essence, the Boltzmann superposition principle states the following: In a linear system, the aggregate response of a viscoelastic material to a strain history is the sum of all responses of the material to a sequence of individual and incremental strain histories.[68,73] This may be phrased mathematically as

$$\gamma(t) = \sum_{\theta_i=-\infty}^{\theta_i=t} \sigma_i J(t-\theta_i), \tag{2.2}$$

where $\gamma(t)$ is the strain history at time t, σ_i represents the incremental stresses applied at times θ_i, and J(t) is the viscoelastic compliance function.[68-70,74] Taking the limit as time approaches zero for the stress increments produces the Boltzmann superposition in integral form,

$$\gamma(t) = \int_0^{\sigma(t)} J(t-\theta)d\sigma = \int_{-\infty}^{t} J(t-\theta)\frac{d\sigma(\theta)}{d\theta}d\theta.^{[70,73]} \tag{2.3}$$

This is of importance since the response of a material to an arbitrary load history may be found once the response of that material to a step stress is known experimentally.[73] A more specific expression of the Boltzmann superposition relates the recovery strain to the creep strain

$$\gamma_r(t) = \gamma_{creep}(t) - \gamma_{creep}(t-\theta).^{[72]} \tag{2.4}$$

This form has been used successfully by Plazek to experimentally verify the adherence of a 23% cellulose nitrate solution to the Boltzmann superposition and prove the applicability of the principle.[76] The superposition principle is demonstrated graphically in Figure 2.8.

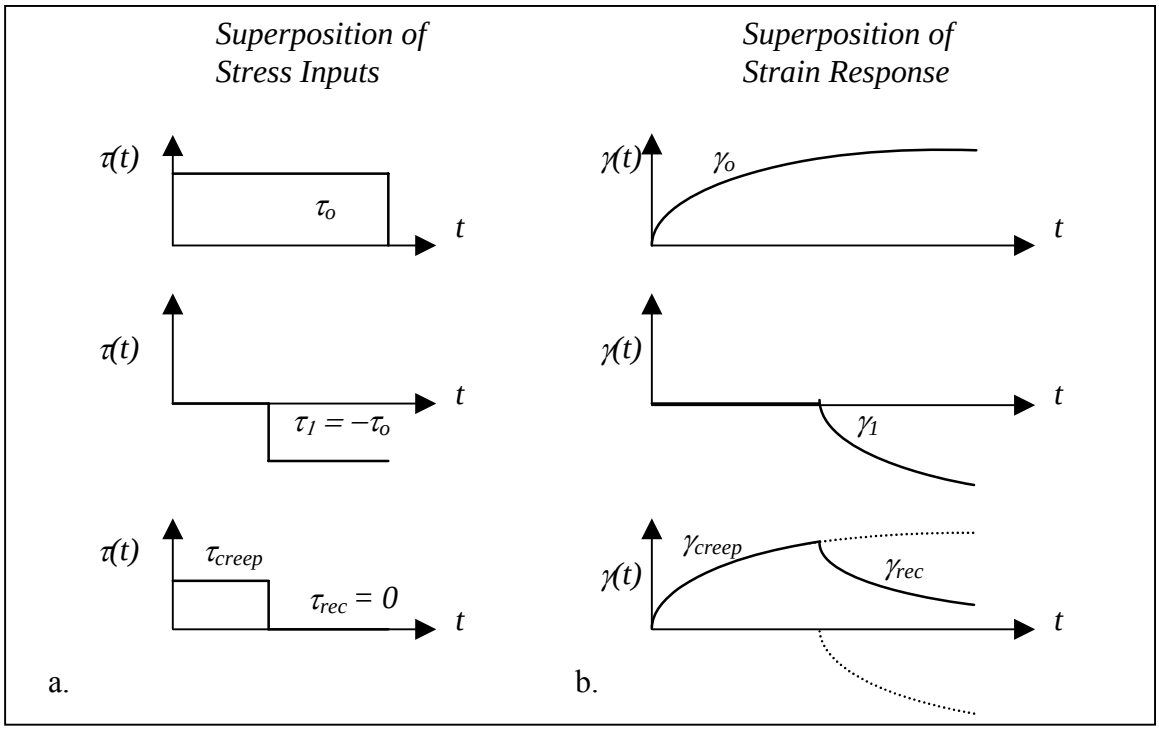

Figure 2.8 Demonstration of Boltzmann superposition principle.
In the column to the left (a), the superposition of stress inputs is shown. The initial creep stress, τ_o, is assumed to continue for the entire duration of the experiment. For the recovery, an equal and opposite stress, τ_1, is applied so that the summation of τ_o and τ_1 is zero stress. The superposition of stresses resulting in the creep and recovery experiment is shown at the bottom of the left column. A similar pattern follows for the superposition of the strain response in the column to the right (b). Figure adapted for creep from Lakes.[73]

Another criterion for linearity, as indicated by Lakes, is independence of the experimentally determined creep function, J(t), from stress when plotted on axes of compliance versus time (Figure 2.9a). This is necessary for viscoelastic linearity, although it is not a sufficient criterion.[73] That is to say that, while this occurrence cannot guarantee linearity, its absence directly indicates the presence of viscoelastic nonlinearity. Restating this criterion, the creep strain is directly proportional to the applied stress at a given time when plotted on axes of strain vs. time (Figure 2.9b). Thus, an experiment performed at some multiple, n, of the initial stress ($\tau_2 = n\tau_1$) will produce a strain response at a multiple, n, of the initial strain ($\gamma_2 = n\gamma_1$).[70]

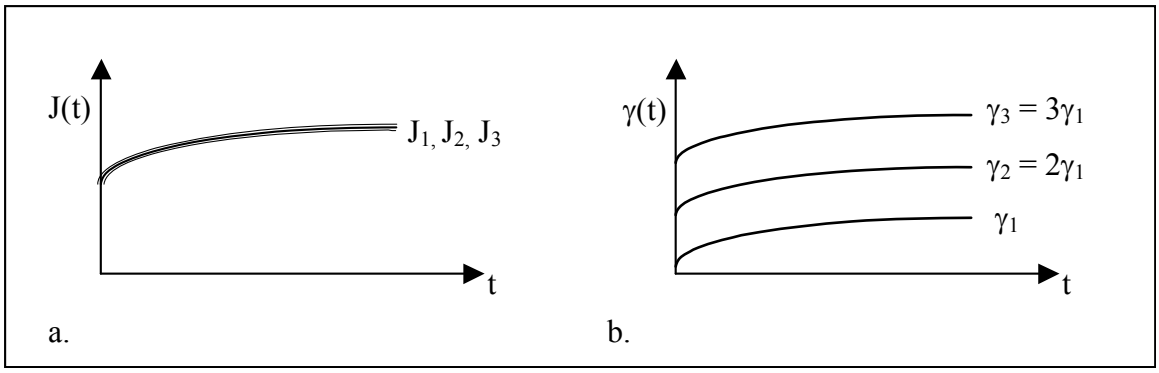

Figure 2.9 Plots of (a) compliance and (b) strain versus time for a linear viscoelastic material.
At left (a), the compliance curves for the material are independent of the applied stress so they are all identical. At right (b), the strain curves are unique and differ by a factor, n, of the applied stress.

Clearly, as Lakes points out, multiple experiments are necessary to distinguish linear from nonlinear viscoelasticity. Although axes of strain versus stress are less frequently studied in viscoelastic materials, a series of creep experiments performed at different stresses may be used to indicate or refute linearity by plotting isochronals (lines of data taken at a constant time) on these axes. A given material is linearly viscoelastic if the isochronals are straight, isolated lines (Figure 2.10a) and nonlinearly viscoelastic if curved, isolated isochronals are present (Figure 2.10b).[73] Further, if the isochronals all line up on top of one another (non-isolated), whether curved or straight, the material is not viscoelastic but of some other form independent of time instead such as purely elastic.

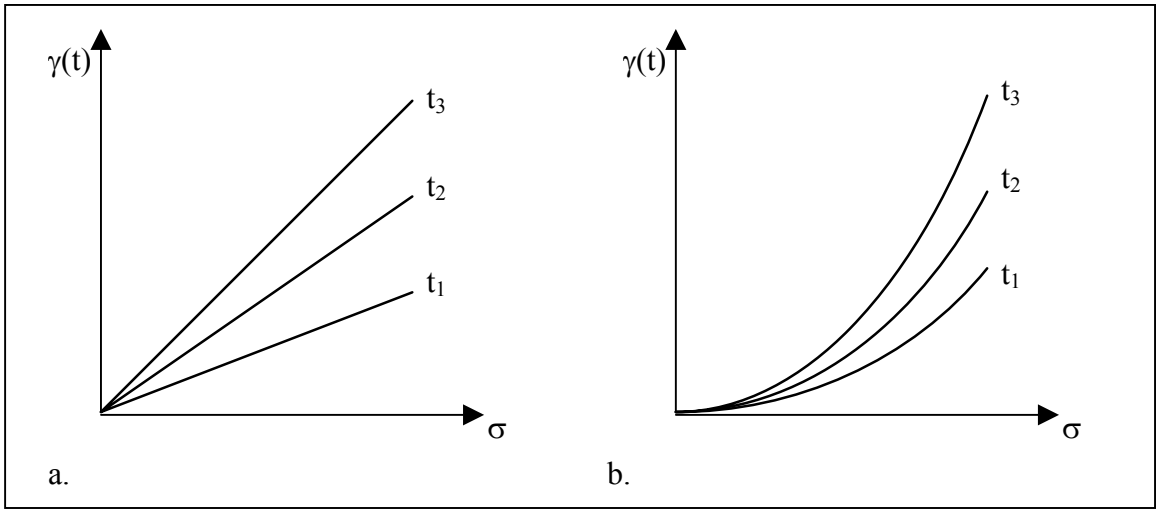

Figure 2.10 Isochronal data for (a) linear and (b) nonlinear viscoelastic materials.
On axes of strain versus stress, straight lines indicate viscoelastic linearity and curved lines indicate nonlinearity.[73]

2.3.5 Nonlinear Viscoelasticity

In general, nonlinear viscoelastic behavior encompasses any viscoelastic behavior that deviates from linear viscoelasticity. As a result, the Boltzmann superposition principle and interrelations among viscoelastic functions no longer apply. It was previously stated that a common example of nonlinear viscoelasticity is the dependence of the creep behavior of a material on the applied stress. This complicates analysis since stress and time are generally not separable variables when this occurs.[69] Nonlinear viscoelasticity may be manifested in other forms as well. For example, a material may fundamentally be linear viscoelastic, except when yielding damage is accrued that alters the material stress response.[77] Yielding is a nonlinear viscoelastic phenomena that occurs in viscoelastic materials as a result of damage or breakdown of the material structure. On compliance versus time plots with linear axes, the onset of yielding may be identified by positive acceleration of the curve, as seen in Figure 2.11a, which indicates the accumulation of damage at an increasing rate.[73] In a polymer, this increasing rate of damage

usually represents the breaking of a secondary structure, such as van der Waals interactions. As stresses in the material cause individual polymer chains to rupture, fewer and fewer chains remain that must support the applied load, causing each new chain rupture to occur more quickly than the previous.[78] This will eventually lead to ultimate failure of the material. For log-log plots of compliance versus time, a slope of unity indicates steady state viscous flow.[69] Therefore, a slope greater than unity on log-log axes, as seen in Figure 2.11b, may be used to identify the presence of yielding. Mathematically, this may be obtained from the expression of shear creep compliance for linear amorphous polymers (viscoelastic fluids), giving

$$J(t) = J_g + J_d\psi(t) + \frac{t}{\eta}\ , \tag{2.5}$$

where t/η is the permanent (viscous) deformation term.[70] In the long time limit ($t\rightarrow\infty$), $\psi(t)$ becomes unity and $J_g + J_d$ may be replaced by a single constant. For viscous flow, we neglect the constant term, leaving the permanent deformation approximately proportional to the compliance,

$$J(t) \cong \frac{t}{\eta}\,. \tag{2.6}$$

Taking the common log of each side and rearranging produces

$$\log J(t) = \log t - \log \eta\,, \tag{2.7}$$

which is plotted as a straight line with a slope of unity on log-log axes of compliance versus time.[70,78]

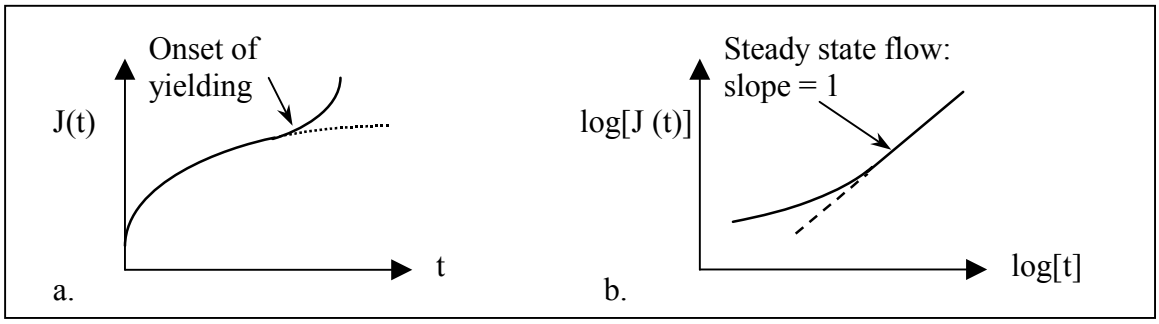

Figure 2.11 Compliance vs. time plots of yielding behavior on (a) linear and (b) log-log axes.

In general, a material will appear to be more compliant after yielding has taken place than it had prior to yielding at the same stress. This softening is due to permanent damage of the material structure.[77] In certain cases, mending may occur in the material, which repairs the bonds or chains that have been broken due to yielding. In this instance, if a material that has experienced yielding is given sufficient recovery time to rest, or if it is only subjected to low stresses for short periods of time, mending may occur as evidenced by the approach of the material compliance back to its original pre-yield compliance.[78]

Another form of nonlinearity, designated the term factorization by Thor Smith and commonly known as quasilinear viscoelasticity (QLV), allows the compliance function to depend on stress by accounting for nonlinear elastic stress - strain behavior.[80,79] Despite debate of its applicability, this form of nonlinearity is frequently used to model the viscoelastic behavior of soft biological materials.[81] The compliance function, now depending on stress as well as time, may be separated into a function of stress and a function of time, producing

$$J(t,\sigma) = J_t(t)g(\sigma), \tag{2.8}$$

where $J_t(t)$ is independent of stress.[80,81] The corresponding constitutive relation becomes

$$\varepsilon(\sigma,t) = \int_0^t J_t(t-\tau)\frac{d\varepsilon}{d\sigma}\frac{d\sigma(\tau)}{d\tau}d\tau\,.^{(73,81)} \tag{2.9}$$

In the creep experiment, discerning between intrinsic, elastic nonlinearity within the material and time dependence can be achieved using a log-log plot of strain versus time (Figure 2.12), where the creep curves must all have the same slope and shape, shifting vertically along the ordinate at varying levels of stress in order for QLV to be present.[81]

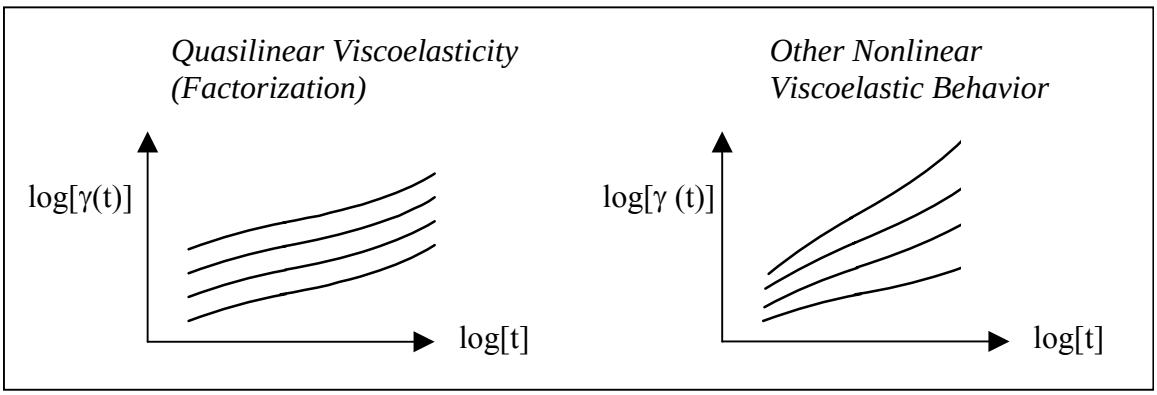

Figure 2.12 Depiction of QLV in creep compared to more general nonlinearity.
In QLV theory, creep curves shift vertically along ordinate by a factor but original slope and shape is maintained.

Unfortunately, separable nonlinearity for which QLV applies and other, less complex modes of nonlinear response are limited to a relatively narrow selection of materials or material responses.[81] The necessity for a more general nonlinear constitutive model has brought about the nonlinear superposition method (also referred to as the modified superposition) and Schapery's nonlinear viscoelastic theory.[80] In the compliance formulation, the nonlinear superposition is

$$\varepsilon(t) = \int_0^t J(t-\tau,\sigma(\tau))\frac{d\sigma}{d\tau}d\tau\,, \tag{2.10}$$

which permits a stress dependent creep function and history dependent effects to be modeled.[73] However, it is based on the assumption that the rate of recovery is the same as the rate of creep, which may not be true for all materials.[73] The Schapery model, which relies on irreversible thermodynamics in its derivation, is formulated for creep as follows:

$$\varepsilon(t) = J_0 g_0 \sigma(t) + g_1 \int_0^t J(\zeta(t) - \zeta_\tau(\tau)) \frac{dg_2\sigma(\tau)}{d\tau} d\tau \,, \tag{2.11}$$

where ζ and ζ_τ are reduced time variables, J_0 is independent of time, and g_0, g_1, and g_2 are stress dependent material properties.[73,82] The assortment of parameters in the Schapery model permits broad applicability, although this also lends itself to increased modeling tedium.[73,80] Despite shortcomings of both the nonlinear superposition method and Schapery theory, these models have been successfully used to describe the behavior of soft tissues and provide a general context for modeling nonlinear viscoelastic materials.

2.3.6 Andrade Creep

The Andrade creep model represents a particular mode of creep, where the delayed compliance term varies with time to the one-third power. The original creep model, applied to wires of lead, copper and other ductile materials, assumes the form of

$$l = l_0 (1 + \beta t^{1/3}) e^{kt} \,, \tag{2.12}$$

where l is the length at time, t, l_0 is the initial length, and β and k are stress dependent material constants.[66,83] Cellulose nitrate was later shown by Van Holde to creep according to

$$\varepsilon = \varepsilon_0 + \beta' t^{1/3} \,, \tag{2.13}$$

where ε is the elongational strain at time, t, ε_0 is the instantaneous strain, and β' is a characterizing coefficient.[76] Note that for infinitesimal strains and k equal to zero, equation

2.13 and the original Andrade model (equation 2.12) are equivalent. Modifying the shear creep compliance in equation 2.5, $J(t) = J_g + J_d\psi(t) + \frac{t}{\eta}$, the Andrade model has been applied to linear amorphous polymers in the form

$$J(t) = J_g + J_d\psi(t) + \beta t^{1/3} + \frac{t}{\eta}.^{(76)} \tag{2.14}$$

Recalling that $\Psi(t)$ approaches unity at long times, a single constant, J_A, may replace J_g and $J_d\Psi(t)$ for steady-state creep, producing

$$J(t) = J_A + \beta t^{1/3} + \frac{t}{\eta}.^{(72,80)} \tag{2.15}$$

Since the instantaneous compliance, J_A, is constant, and the $\beta t^{1/3}$ term is completely recoverable,[69] permanent deformation is attributed exclusively to the viscous processes term, t/η. At short times and in the limit of infinite viscosity ($\eta \to \infty$), the viscous term may be neglected. Thus, equation 2.15 produces a straight line of slope, β, and intercept, J_A, when plotted on axes of compliance versus cube root of time. At long times where viscous processes become dominant, slight positive curvature of the creep curve is displayed (Figure 2.13).

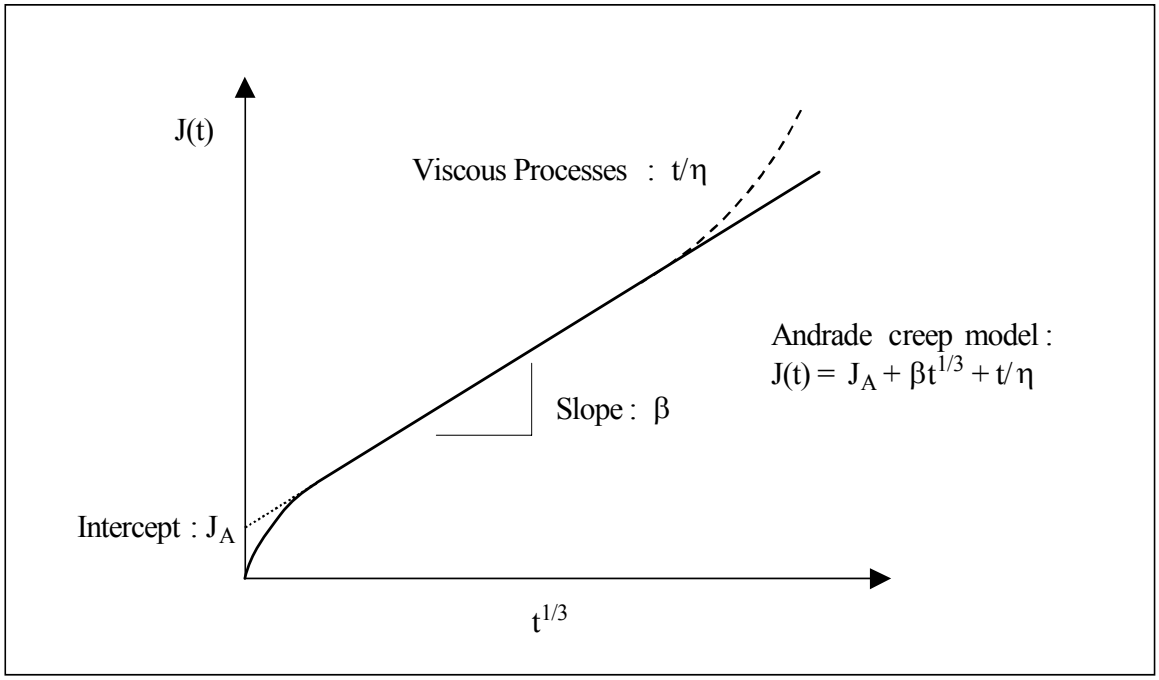

Figure 2.13 Depiction of the Andrade creep model (in form of equation 2.15).
Model parameters are identified by plotting creep data on axes of compliance vs. cube root of time. The slope, β, is the slope of the straight line data on the given axes. The Andrade intercept, J_A, is the resulting value if the straight line data were extended to an imaginary intercept with the ordinate. If viscous processes are present, the data will curve upward silightly at long times. The viscous term, t/η, may be determined by subtracting the recoverable compliance, $J(t) = J_A + \beta t^{1/3}$ from the total creep compliance data.

While attempts have been made to explain the mechanism of Andrade creep, a definite justification has yet to be proven. In general, the pervasiveness of Andrade creep at large strains suggests a broad mechanism rather than precise atomic processes.[85,86] One proposed physical theory suggests that the $t^{1/3}$ term represents aggregate transient creep behavior, where the aggregate is composed of randomly distributed weak and strong "centers" or regions (e.g., dislocations, cross-linkages, interconnections, cells, etc.).[87] Further, as a creep experiment progresses, weak linkages rupture and the stress is transferred to strong linkages that sustain the load, the progression rate at which may be determined by a viscous medium or other general flow process.[87] A more recent analytical theory, expanding upon the idea of distributed weak

and strong regions, relies upon the commonly accepted notion of thermal activation controlled deformation. This theory uses thermal activation energy to establish that the creep strain rate is proportional to the strain by a power of negative two, or

$$\dot{\gamma} \propto \gamma^{-2}.^{(85)} \tag{2.16}$$

Rewriting equation 2.16 produces

$$\frac{d\gamma}{dt} \propto \frac{1}{\gamma^2}. \tag{2.17}$$

It follows from equation 2.17 that

$$t \propto \int \gamma^2 d\gamma. \tag{2.18}$$

Thus, integrating and solving for γ, it may be seen that the strain is proportional to the cube root of time, or

$$\gamma \propto t^{1/3}.^{(85)} \tag{2.19}$$

3.0 SPECIFIC AIMS

3.1 ESTABLISH PROCEDURE FOR TESTING RABBIT NP TISSUE

- Employ creep testing method
- Justify employed methods
- Evaluate methods against other available methods

3.2 BUILD DATABASE OF RABBIT NP TISSUE CREEP BEHAVIOR

- Determine general creep behavior at multiple stresses
- Determine if creep behavior is linearly viscoelastic or nonlinearly viscoelastic
- Quantify critical (yield) strain of tissue

3.3 APPLY CONSTITUTIVE MODEL TO DESCRIBE TISSUE BEHAVIOR

- Determine a constitutive model that approximates tissue creep behavior
- Evaluate model for goodness of fit
- Evaluate model against other available models
- Attempt to predict tissue behavior using model

4.0 EXPERIMENTAL METHODS

4.1 INSTRUMENTATION

4.1.1 AR1000 Rheometer

The testing was performed using an AR1000 Rheometer (TA Instruments, New Castle, DE), which is an instrument capable of performing creep, dynamic, and flow experiments on both fluids and solids through various attachable test geometries. Figure 4.1a provides a front view of the complete instrument while Figure 4.1b provides detail of the Peltier plate and attached geometry. The instrument applies a torsional shear load to the specimen causing it to deform or flow, depending on the desired test procedure. The advantage of shear loading is the volume of the specimen is constant throughout the duration of the experiment.[4,69] General features of the AR1000 rheometer with relevance to this research are the Peltier plate, drag cup motor, spindle and air bearings, and angle detection sensor. An understanding of how these components function will result in a better understanding of the capabilities and limitations of the rheometer as a whole.

a. 

b. 

Figure 4.1 (a) AR 1000 Rheometer. (b) Detail of Peltier plate with 6 mm conical geometry.

The Peltier plate is the component responsible for controlling the temperature of the tissue specimen. Through the application of a voltage, the plate relies on the Peltier effect to produce a temperature differential between the junctions of two dissimilar metals, acting as a heat pump.[78,88] Multiple junctions are used to heat or cool the surface of the plate. A flow of water through the internal channels of the plate serves as a heat sink, removing excess heat from the plate.[88] A temperature transducer located at the center of the plate is used to precisely measure and maintain the desired temperature.[88] The operating range of the Peltier plate on the AR1000 rheometer is between –10 ºC and 99 ºC.[88]

The drag cup motor, capable of producing a precise torque regardless of the angular position, is used to apply the constant torque necessary for creep testing.[70] The drag cup motor is coupled to the spindle of the rheometer, a shaft that passes from the drag cup motor to the location where the geometry attaches for testing. The spindle is suspended and positioned radially by low-friction air bearings. Due to surface imperfections in the air bearings, the

bearing serves as a degenerate turbine and produces a low but measurable torque.[70] The instrument must be rotationally mapped during setup to account for this by countering the torque produced by the air bearing with the drag cup motor. A high-resolution optical encoder detects the angular position of the spindle. It consists of a light source that is shone through a rotating disk and into a photoelectric sensor to deliver an angular resolution of 0.62 micro-radians.[88]

4.1.2 Cone and Plate Geometry

Two specialized geometric components, interfacing directly with the test specimen, comprise the cone and plate of the rheometer. As the name implies, the geometry consists of a cone shaped platen and a flat plate, between which the specimen is situated (Figure 4.2a). The cone angle may be a maximum of 0.1 rad (approximately 6º) and the cone apex is intended to meet precisely with the plate surface. For practical purposes, the apex is truncated and the truncation height is the height that the cone is positioned above the plate such that the cone would intersect the surface of the plate at the imaginary apex. The experimental setup of this research uses a Peltier plate to serve the plate function and a custom-made stainless steel cone with the following dimensions: 6 mm base diameter, 2º cone angle, and 20 μm truncation, corresponding to an approximate sample volume of 2 mm^3.

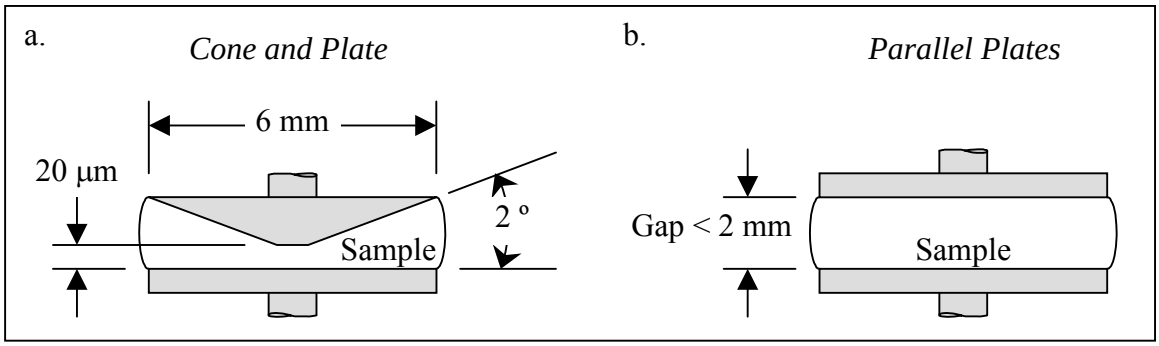

Figure 4.2 Representation of (a) cone and plate geometry and (b) parallel plate geometry.
The gap height of the cone is the height that the apex of the cone is truncated. This is necessary so that the imaginary tip of the apex ceases at the surface of the plate. In the figure, the gap height is 20 μm. With parallel plates, the gap height may vary up to a maximum of 2 mm.

One of the most desirable features of the cone and plate setup is that the shear stress distribution throughout the specimen is approximately constant, resulting in a homogeneous shear strain.[67,78] This is attractive since events within the material behavior may be initiated at particular values of strain, the precise determination of which is facilitated by a homogeneous shear strain throughout the specimen. The simplicity of the working equations is also a useful quality associated with the cone and plate. The shear stress, τ, may be calculated using the equation

$$\tau = \frac{3T}{2\pi R^3}, \tag{4.1}$$

where T is the applied torque and R is the base radius of the cone.[67] The shear strain, γ, may be calculated from

$$\gamma = \frac{\phi}{\alpha}, \tag{4.2}$$

where ϕ is the angular displacement and α is the cone angle. Thus, if the shear strain were to equal unity and assuming the cone angle to be 2º, then the corresponding angular displacement,

ϕ, may easily be found to be 2º of rotation. Similarly, the shear rate, $\dot{\gamma}$, is obtained from

$$\dot{\gamma} = \frac{\omega}{\alpha} = \frac{\dot{\phi}}{\alpha}, \tag{4.3}$$

where ω is the angular velocity.[67]

Given the advantages of the cone and plate, a disadvantage is that the specimen must be situated within the small gap that results from a shallow cone angle (the maximum gap height at the edge is approximately 0.1 mm for a 6mm, 2º cone). Deforming the specimen to fit within this gap creates considerable installation deformation and makes it difficult to fixture stiff specimens, which may be more inclined to slide out from underneath rather than deform under the considerable applied pressure. Since the gap must be completely filled around the periphery of the cone, it is pertinent that the specimen be prevented from sliding out. As a result, it may be necessary to use an alternate geometry such as two parallel plates instead of a cone and plate (Figure 4.2b). Although parallel plates may have fewer conveniences than the cone and plate, a gap between the plates of up to 2 mm in height is permissible,[70] thus easing the fixturing process.

4.2 PRE-EXPERIMENTATION SETUP

4.2.1 Instrument Setup and Calibration

Before testing a specimen, it is necessary to verify that the instrument is calibrated and configured in the same state each time to minimize error that may result from slight differences in setup. Details of this procedure are provided here to assist the experimenter in achieving results consistent with the current setup employed. In order to ensure proper interfacing with the

specimen, the Peltier plate and stainless steel cone are cleaned with acetone or soap and water to remove surface residue. The inertia of the instrument and geometry are calibrated in order to compare this value with the previously determined value. This ensures that no significant alterations have occurred that are unperceivable to the operator. The instrument is rotationally mapped to identify the angular positions of degenerate torques that result from the air bearing. The rotational mapping is performed using a single-iteration precision mapping. The geometry gap height is re-zeroed each time to ensure a precise 20 μm gap that may otherwise deviate from detaching and reattaching the geometry. The gap is zeroed using a friction mode that gradually lowers the rotating cone to the plate until the cone stops due to the friction of coming into contact with the plate. Following this, the spindle head is shifted upward to position the cone at 4.5 cm from the plate for subsequent specimen placement.

4.2.2 Specimen Preparation and Installation

Skeletally mature, healthy, New Zealand white rabbits are sacrificed and the lumbar spines are freshly harvested (approved by University of Pittsburgh IACUC). Sectioning the respective L5 and L6 vertebral bodies centrally and perpendicular to the spinal axis using bone cutters isolates the L5-L6 disc. The disc and spinal segment are wrapped in sterile plastic and frozen at –20 ºC. On the day of testing, a spinal segment is individually thawed at room temperature for about 1 hr. Excess tissue is removed using sharp and blunt dissection to clearly expose the IVD. Favoring one of the vertebral bodies, a full transverse incision is made through the disc using a No. 10 scalpel blade. The vertebral bodies are separated and the larger disc portion containing the NP is retained (Figure 4.3). The transition between the NP and AF is traced using the scalpel blade to facilitate extraction. The NP is excised using a lab spatula and transferred to the

rheometer where it is placed in the center of the Peltier plate. Slight positioning adjustments are made to ensure the NP is completely centered. The 6 mm cone is then positioned at its 20 μm gap height, compressing the specimen between the plate and cone. Following this, it must be verified that the specimen completely fills the geometry gap and bulges evenly from under the cone (Figure 4.4). At this time, mineral oil may be applied to the specimen (Figure 4.5) or the humidity chamber doors may be replaced and humidification begun, depending on the specific testing procedure, thus completing specimen installation.

Figure 4.3 Axial cross-section of rabbit intervertebral disc.

Figure 4.4 Photograph of fixtured NP specimen. Geometry gap is completely filled.

Figure 4.5 Photograph showing fixtured NP with mineral oil applied.

4.3 EXPERIMENTAL TESTING PROCEDURES

4.3.1 Variable Stress Testing

Testing was performed with the objective of determining the general behavior of the tissue under typical creep testing methods. Following specimen fixturing and prior to the start of testing, a slight coating of mineral oil was applied to the specimen around the periphery of the cone (Figure 4.5). The temperature of the Peltier plate was set to 25 ºC. Creep was begun at a shear stress of 2 Pa and maintained for 1000 s. The zero-stress recovery step immediately followed and was maintained for a duration of 1000 s. Pairs of creep and recovery steps were subsequently repeated for stresses of 6Pa, 18Pa, 54Pa and 162Pa in increasing order (Table 4.1). The stresses were chosen since 2 Pa was essentially the lowest applicable stress for the selected cone geometry and each additional stress value increased by a factor of 3 over the previous. On log-log axes of strain versus time, the resulting data from each consecutive stress increase would be separated along the ordinate by about 0.5 logarithmic units.

Table 4.1 Variable stress testing procedure.

Experiment Step	Applied Creep Stress (Pa)	Duration (s)
Creep and Recovery 1	2	1000 (each)
Creep and Recovery 2	6	1000 (each)
Creep and Recovery 3	18	1000 (each)
Creep and Recovery 4	54	1000 (each)
Creep and Recovery 5	162	1000 (each)

4.3.2 Consecutive Creep Testing at 6 Pa Stress

The objective of the consecutive creep testing was to identify mechanisms possibly promoting a general reduction in compliance with each consecutive creep run at the same stress. Plausible events taking place within the tissue that could create a change in compliance were identified including a change in hydration, a structural alteration mechanism (i.e., general decay, failure of cross-links or bonds, etc.), or additive memory (loading-history) effects associated with incomplete recovery. It was surmised that repeated application of creep and recovery steps at the same stress level would provide insight regarding experimental repeatability and highlight trends associated with changes in compliance level. In order to recover out any installation effects, a pretest recovery was performed on the specimen prior to the start of actual creep testing. Initially, the duration was dependent on the observed rate of recovery, requiring the recovery rate to effectively slow to zero. The pretest recovery was ended when the linear plot of recovery versus time reached a plateau. After testing the first four specimens, the duration of the pretest recovery was changed to a set time of 4850 s (80 min.) due to inconsistencies in observing the recovery rate, particularly at shorter times. The duration was then changed again and finalized to depend on the observed rate of recovery once a minimum of 4850 s had passed. After the pretest recovery, a creep step was performed at a stress of 6 Pa for 300 s and a 3000 s recovery

followed. The pairs of creep and recovery steps were repeated 34 times. Two of the specimens were tested with altered recovery step durations of 31800 s (8 hrs. 50 mins.) to separate effects related to general time from effects associated with the number of creep steps performed. The procedures applied to each specimen are provided in Table 4.2 below.

Table 4.2 Procedural summary for consecutive creep testing.
Overview of consecutive creep testing procedure. Specimens are listed in order of increasing pre-test recovery time.

Specimen	Pre-test recovery time	Creep stress	Creep duration	Recovery duration	Total creep steps	Pre-test recovery duration criteria
rab17	116 s	6 Pa	300 s	3000 s	26	Recovery Rate
rab20	680 s	6 Pa	300 s	31800 s	4	Recovery Rate
rab18	2315 s	6 Pa	300 s	31800 s	4	Recovery Rate
rab19	4725 s	6 Pa	300 s	3000 s	22	Recovery Rate
rab22	4850 s	6 Pa	300 s	3000 s	34	4850 s (~ 80 min)
rab24	8731 s	6 Pa	300 s	3000 s	34	Recov. Rate (> 80 min)
rab26	14654 s	6 Pa	300 s	3000 s	34	Recov. Rate (> 80 min)
rab25	22519 s	6 Pa	300 s	3000 s	34	Recov. Rate (> 80 min)

4.3.3 Mineral Oil Dye Testing

The objective of the mineral oil dye testing was to determine whether mineral oil, in spite of its non-physiological nature, was a suitable method of preventing the specimen from dehydrating. The experiment designed to address this issue consisted of coloring the mineral oil and observing whether it leached into the specimen or altered the specimen by some other physical means. The colorless mineral oil was dyed red using Oil Red O, an oil soluble dye often used in staining fat lipids for histology studies. After filtering to remove excess dye particles, the dyed mineral oil was drawn into a 1.0 mL syringe. A rabbit NP tissue specimen was excised from a thawed IVD and placed on a glass microscope slide, simulating the specimen installation procedure for the rheometer. Approximately 0.1 to 0.2 mL of the dyed mineral oil were placed in several drops

around the periphery of the NP specimen and a microscope cover slide placed over top, spreading the mineral oil evenly around the tissue. Aside from convenience, the microscope slide and cover slide served to replicate the testing environment of the specimen in the rheometer when using the mineral oil. The similarities follow: the top and bottom surfaces of the compressed specimen were covered by a relatively non-porous medium and the thin edge height that remained was in contact with the mineral oil. Immediately following installation and for several days thereafter, the specimen was viewed under an Eclipse E800 microscope (Nikon, Melville, NY) at magnifications of 4x and 10x. Observations were recorded and photomicrographs captured.

4.3.4 General Humidity Chamber Setup and Testing

The objective of developing and using a humidity chamber to perform tests on specimens was two-fold. Primarily, trial use of a humidity chamber was expected to provide insight into methods of sustaining specimen hydration. In order to evaluate the use of mineral oil, a performance comparison with the competing approach was necessary. According to the literature, the humidity chamber appears to be preferred for mechanical testing of the IVD and NP tissue since full immersion in a saline bath, also used in hydrating biological tissue, produces substantial specimen swelling.[4,6,7,23,37,89] A secondary objective for using a humidity chamber was the possibility of added experiment control. Relative humidity is the ratio of moisture content in a gaseous environment to the maximum moisture that may be sustained by the environment at the existing temperature. Based on this definition, the theory behind use of a humidity chamber to prevent dehydration is as follows: as a gaseous environment approaches 100% relative humidity, the evaporation potential of water in that environment approaches zero. However, it is plausible that large water droplets in the air (i.e., mist) could also settle onto the

specimen, contributing to increased specimen hydration. Therefore, the ability to control or adjust specimen hydration is expected to permit direct study of how hydration affects the NP viscoelastic behavior.[23,90]

The humidity chamber prototype employed in the current study consisted of an acrylic glass (PMMA) chamber with removable doors to allow for ease of specimen installation, dual air inlets, flexible transport passages, a bypass valve, a condensate trap, and an ultrasonic humidifier. These features may be seen in Figure 4.6. The humidifier employed was a "Cool Spray" model 671 ultrasonic humidifier (Sunbeam, Jarden Corp., Rye, NY), possessing controls to adjust both humidity output and mist output, the latter of which apparently controlled droplet size. Ultrasonic humidifiers are desirable for this application since the humidity output rate is approximately independent of the ambient humidity content.[91] By design, the chosen humidifier operates at a fixed airflow output velocity and so a bypass valve was necessary to control the air velocity entering the chamber. To prevent excess condensate from entering the chamber, a condensate trap and drain was placed in series with and upstream of the chamber. Dual chamber inlets split the airflow entering the chamber to further reduce the velocity and to avoid placing the spindle directly in line with the flow. Due in part to the bypass valve and dual inlets, the airflow velocity entering the chamber was effectively reduced to levels comparable with ambient air currents. In addition, humidity levels of up to 99.5 % were measured using a probe-type hygrometer (Hygrodynamics, American Instrument Co., Silver Spring, MD).

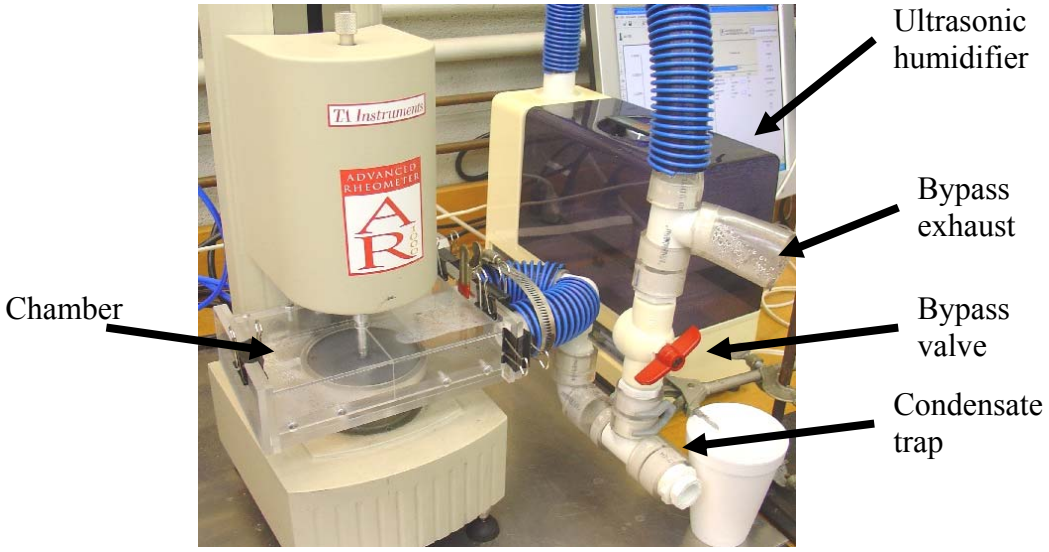

Figure 4.6 Rheometer setup with prototype humidity chamber and supporting subsystems.

The humidity chamber was operated in four modes during testing: installation, equilibration, active humidification, and passive humidification. During the installation mode, the specimen was fixtured beneath the cone of the rheometer and a small amount (< 0.1 ml) of physiological saline (0.15 M NaCl) was applied to the periphery of the NP tissue. This moistening was done to equilibrate the swelling pressure differential in the tissue and prevent proteoglycan disturbances following the fixturing compression of the specimen.[7] It is assumed that no leaching of the proteoglycans or NP swelling occurred from the application of the saline since only a light surface coating was applied. The doors were replaced and the humidity chamber was first purged for 5 to 10 s at maximum humidifier output to rapidly increase the humidity in the chamber to near 100%, after which point the humidifier was set to a predetermined low humidity-output level necessary for actively maintaining the humidity in the chamber. The specimen was permitted an unlimited duration pre-test recovery until the recovery rate dropped below 0.00002 (1/s).

The equilibration mode was an iterative process used to stabilize the compliance level of the specimen. This was done by performing a series of short creep and recovery steps followed by adjustment of the humidifier. Typically, a relatively stable compliance level could be attained within the first three iterations. Once the compliance level stabilized and the final recovery step was sufficiently slow, the next mode could be entered. Following equilibration mode, either active or passive humidification could be performed. Active humidification required the humidifier settings established during the equilibration mode be maintained. If the humidifier tank became low during this time, a reservoir in the base of the humidifier permitted the tank to be removed and refilled while continuing operation. For the passive humidification mode, the humidifier need only be switched off. For this reason, it was convenient to incorporate both active and passive humidification modes into the testing of a particular specimen. Wet towels or sponges could be placed inside the humidity chamber during specimen installation that would help to maintain the humidity level during the passive mode. The humidity level was generally maintained at about 98% for two hours or more before finally beginning to decrease. The procedure applying to the equilibration mode and accompanying modes are detailed in Table 4.3. A schematic representation of the equilibration mode procedure is provided in Figure 4.7.

Table 4.3 Humidity chamber operation modes and corresponding testing procedures.

Mode	Step	Duration	Notes
Installation	Pre-test recovery	Unlimited	Continue until $\dot{\gamma} < 2\text{x}10^{-5}\ s^{-1}$
Hydration and Humidity Equilibration	6Pa Creep	60 s	Repeat 6 total cycles, final recovery until $\dot{\gamma} < 2\text{x}10^{-5}\ s^{-1}$
	Recovery	180 s	
	Event: Adjust humidifier if necessary		
	6Pa Creep - reverse torque for even tests	60 s	Repeat 6 total cycles, final recovery until $\dot{\gamma} < 2\text{x}10^{-5}\ s^{-1}$
	Recovery	180 s	
	Event: Adjust humidifier if necessary		
	6Pa Creep - reverse torque for even tests	60 s	Repeat 6 total cycles, final recovery until $\dot{\gamma} < 2\text{x}10^{-5}\ s^{-1}$
	Recovery	180 s	
	Event: Adjust humidifier if necessary		
Active Humidification	Design creep and recovery steps to suit experimental needs	--	Perform final recovery until $\dot{\gamma} < 2\text{x}10^{-5}\ s^{-1}$
Passive Humidification	Design creep and recovery steps to suit experimental needs	--	Perform final recovery until $\dot{\gamma} < 2\text{x}10^{-5}\ s^{-1}$

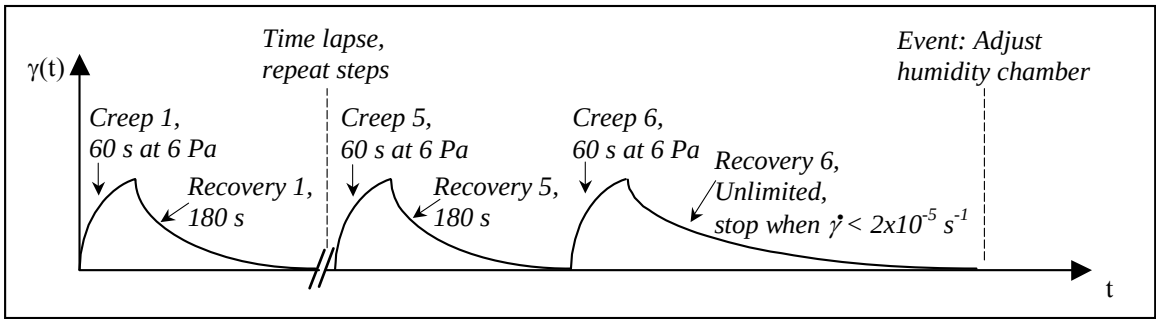

Figure 4.7 Representation of initial procedure for the equilibration mode.
The figure provides the first of three sets of procedures in the equilibration mode. Initially, 60 s creep and 180 s recovery steps are repeated 6 times. During the final recovery step, the duration is permitted to continue until the recovery strain rate is less than $2\text{x}10^{-5}\ s^{-1}$. At this point, the material is sufficiently recovered. Following the final recovery, the output level of the humidity chamber may be adjusted. This entire procedure is essentially repeated two more times, with the exception that the applied torque is reversed for even numbers of the creep test. Following the equilibration mode, general testing procedures may be performed in the active or passive humidification modes.

4.3.5 Variable Temperature Testing

The objective of the variable temperature testing was to determine the effects of temperature on the viscoelastic behavior of the NP tissue. This testing was performed while using the humidity chamber during the active humidification mode. In general, testing consisted of a series of creep and recovery steps with subsequent changes in temperature following the end of each recovery step. The testing procedures used are summarized in Table 4.4 and Table 4.5.

Table 4.4 Temperature ramp up (or down) testing procedure between 25 ºC and 40 ºC.

Procedure	Step	Duration	Notes
Temperature ramp up from 25 ºC to 40 ºC (Temperature ramp down from 40 ºC to 25 ºC is same but in reverse, starting at 40º)	6Pa Creep – start test at 25 ºC	60 s	(+) Increment temp to 30 ºC at end of recovery step
	Recovery	180 s	
	Allow 2 minutes for temperature equilibration		
	6Pa Creep – start test at 30 ºC	60 s	(+) Increment temp to 35 ºC at end of recovery step
	Recovery	180 s	
	Allow 2 minutes for temperature equilibration		
	6Pa Creep – start test at 35 ºC	60 s	(+) Increment temp to 40 ºC at end of recovery step
	Recovery	180 s	
	Allow 2 minutes for temperature equilibration		
	6Pa Creep – start test at 40 ºC	60 s	(-) Reset temp to 25 ºC following end of creep step
	Recovery	unlimited	
	Perform unlimited recovery until $\dot{\gamma} < 2\text{x}10^{-5}\ s^{-1}$ for full recovery		

Table 4.5 Temperature ramp-up ramp-down testing procedure between 25 ºC and 40 ºC.

Procedure	Step	Duration	Notes
Temperature ramp up from 25 ºC to 40 ºC and back down to 25 ºC	6Pa Creep – start test at 25 ºC	60 s	(+) Increment temp to 30 ºC at end of recovery step
	Recovery	180 s	
	Allow 2 minutes for temperature equilibration		
	6Pa Creep – start test at 30 ºC	60 s	(+) Increment temp to 35 ºC at end of recovery step
	Recovery	180 s	
	Allow 2 minutes for temperature equilibration		
	6Pa Creep – start test at 35 ºC	60 s	(+) Increment temp to 40 ºC at end of recovery step
	Recovery	180 s	
	Allow 2 minutes for temperature equilibration		
	6Pa Creep – start test at 40 ºC	60 s	(=) Maintain temp at 40 ºC
	Recovery	180 s	
	6Pa Creep – start test at 40 ºC	60 s	(-) Decrement temp to 35 ºC at end of recovery step
	Recovery	180 s	
	Allow 2 minutes for temperature equilibration		
	6Pa Creep – start test at 35 ºC	60 s	(-) Decrement temp to 30 ºC at end of recovery step
	Recovery	180 s	
	Allow 2 minutes for temperature equilibration		
	6Pa Creep – start test at 30 ºC	60 s	(-) Decrement temp to 25 ºC at end of recovery step
	Recovery	180 s	
	Allow 2 minutes for temperature equilibration		
	6Pa Creep – start test at 25 ºC	60 s	Perform full recovery until $\dot{\gamma} < 2x10^{-5}\ s^{-1}$
	Recovery	unlimited	

4.4 POST-EXPERIMENTAL PROCEDURES

4.4.1 Data Extraction and Processing

Data collected during testing was automatically transferred from the AR1000 control unit to a computer via serial cable and saved to the hard disk as a file containing all necessary testing information such as initial temperatures, calibration data, and individual test steps. Data was preliminarily viewed both in tabular format and graphically with the TA Advantage data analysis

program (TA Instruments, New Castle, DE) in order to determine if the testing was successful and to perform basic checks. For more complex analyses, data was exported into text files, either containing the whole series of experimental steps in a single file or a single step per file, and imported into Excel (Microsoft Corp., Redmond, WA) or Matlab (The MathWorks Inc., Natick, MA).

4.4.2 Quasilinear Viscoelasticity (QLV) Statistical Analysis

The objective of the QLV statistical analysis was to determine if the NP creep behavior is approximately modeled by QLV theory. Assuming the NP behavior may be described by a general power law, $\gamma(t) = At^n$, taking the logarithm of both sides and manipulating gives the equation $\log[\gamma(t)] = n\log[t] + \log[A]$, where n is the log creep rate obtained from the slope of the creep curve on log-log axes of strain versus time.[81] QLV theory requires that $d[\log \gamma]/d[\log t]$ be approximately constant. Thus, to determine if the material obeys QLV, the slope of the creep curve must be independent of the applied stress on log-log axes of strain versus time.

Ten values of *log(strain)* and *log(time)* centralized about times of 3, 10 and 100 s comprised the data used in the analysis. For each specimen, approximate log-log slopes were calculated at stresses of 6, 18, 54, and 162 Pa by the slope of a linear regression through the ten *log(strain)* versus *log(time)* data points. The slope effectively produced $n = d[\log \gamma]/d[\log t]$. At each stress, the mean log-log slope between all the specimens was calculated and a multivariate analysis of variance (M-ANOVA) was performed using SAS PROC ANOVA (SAS Institute Inc., Cary, NC). The M-ANOVA was chosen since it permits assessment of differences among two or more dependent variables with less error than univariate techniques.[92] If the mean slopes are determined to be equal, then the null hypothesis, *Ho*, is accepted and no strong statistical

argument is made. If the null hypothesis is rejected and the alternate hypothesis, *Ha*, is accepted, then the mean slopes are not equal and a strong statistical argument may be made that the NP tissue does not obey QLV. In order for the null hypothesis to be rejected, the statistical significance, p, must be less than 0.05 or $p < 0.05$.

It should be noted that the log-log slopes at stresses of 2 Pa were omitted from the analysis due to issues associated with installation memory effects. In addition, slopes at times of 10 s and 100 s were omitted from the statistical analysis in order to eliminate yielding effects that were occasionally observed at sufficiently long times and sufficiently large strains. For example, yielding or yield-like behavior was observed during a 162 Pa creep test within 10 s so these times were considered sufficiently long in the context of this specific analysis.

4.4.3 Critical Strain Yield Analysis

The objective of the critical strain yield analysis was to determine the strain value where the onset of yielding occurs, since yielding in the specimen was observed at approximately the same level of strain in preliminary creep measurements. Recall, the presence of yielding may be indicated by a positive acceleration of the creep curve on linear axes of strain (or compliance) versus time. Thus, to determine the presence of strain-versus-time inflection points (i.e., points of concavity change where the creep curve begins to accelerate positively), graphical and tabular data were used to identify the relative minimums in the creep velocity versus time. The onset of yielding and corresponding relative minimum velocity, $\omega(t_y)$, is depicted in Figure 4.8. Note that this procedure may also be performed using the strain rate, which is related to the creep velocity by a factor, $1/\alpha$, where α is the cone angle. Since this method only requires the time and strain

at which the relative velocity or strain rate minimum occurs rather than the actual value, either variable is suitable.

Once the relative minimum was identified, the time and strain at that which it occurred was recorded to mark the initiation of yielding. The mean and standard deviation of the yield strain were determined from the sample data taken and the Student's t-distribution was used to determine the mean critical strain at 95% confidence. Thus, for a confidence level, C, the statistically determined mean critical strain will be within the range,

$$\tilde{\gamma}_{crit} = \bar{\gamma}_{crit} \pm t_{(\nu,p/2)} s \Big/ \sqrt{n} \ ,^{(92)} \qquad (4.4)$$

where $\tilde{\gamma}_{crit}$ is the true mean critical strain, $\bar{\gamma}_{crit}$ is the sample mean critical strain, n is the number of samples, $\nu = n - 1$ is the number of degrees of freedom, $p = 1 - C$ is the significance, s is the standard deviation of the sample, and $t_{(\nu,p/2)}$ is determined from the Student's t-distribution chart.

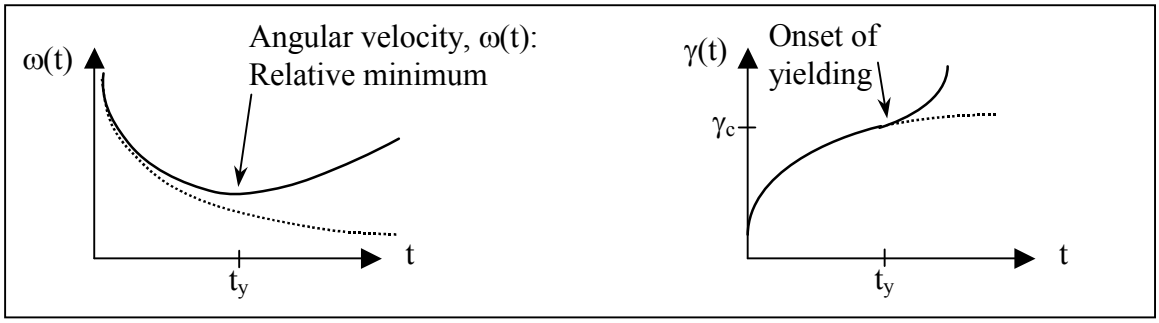

Figure 4.8 Depiction of relative minimum velocity to obtain yield onset time, t_y.
Yield onset time, t_y, was determined by the occurrence of a relative minimum. The critical strain, γ_c, was determined by cross-referencing the yield onset time with the strain occurring at that time.

4.4.4 Computer Assisted Curve Fitting Method

Initially, the Andrade creep model was fit to the creep data using the manual curve fitting method detailed in Appendix A. The objective of using a computer program to aid in fitting the Andrade model to the NP tissue data was to improve upon the quality of fit obtained via the manual fitting method with the intent of quantifying the goodness of fit through more concrete outcome measures. Further, it was believed that the computer aided fitting would allow greater flexibility in modifying the fitting equation to search for a better fit. Compliance, strain, and time data were imported into the Matlab Curve Fitting Toolbox. An exclusion rule was created in the program that excluded data points less than 10 s from calculation of the model parameters. This was done with the interest of modeling only the steady-state (or secondary) creep phase. It was previously determined through graphical analysis that the strain rate at 6 Pa stress becomes effectively constant at about 10 s, indicating the onset of steady-state creep. From equation 2.15, the Andrade creep model, $J(t) = J_A+\beta t^{1/3}+t/\eta$, was fit to the creep data, where J_A is the Andrade intercept, β is the Andrade slope, and η is the viscosity. This was accomplished by setting up a nonlinear regression custom equation in the program with no data smoothing, weighting, or robustness adjustments. In addition to the Andrade model, the more general Nutting creep model was applied to the data, where the 1/3-power of time in the Andrade model is replaced with the n^{th}-power of time, or

$$J(t) = J_A+\beta t^n+t/\eta. \quad (4.5)$$

Model parameters with 95% confidence bounds and fit statistics were generated for each model and data set. The R^2 value and sum of squared error (SSE) value were compared for each fit.

4.4.5 **Model Extrapolation Analysis**

An extrapolation analysis was performed to determine if the Andrade, Nutting, or other model types could extrapolate data best. This analysis was performed using model parameters fit to only the first 30% of the experimental data time range. Similar to fitting the Andrade and Nutting models to the entire data range in Matlab, fits were performed for data between 10 s and 300 s using nonlinear least squares regression by minimizing the overall residual modeling error in the time interval. The remaining 700 s of data were extrapolated using the models. Results of the extrapolation analysis were compared graphically. The two additional models used in the attempt to extrapolate data were of logarithmic and exponential form, found to describe other forms of creep behavior.[66] The logarithmic model is represented by the equation

$$J(t) = J_0 + B\log(t) + \frac{t}{\eta}, \tag{4.6}$$

where the parameter B is the slope of the straight line creep curve plotted as compliance (linear axis) versus the common log of time (log axis). The exponential model is of the form

$$J(t) = J_0 + C(1 - e^{-dt}) + \frac{t}{\eta}, \tag{4.7}$$

where the parameters *C* and *d* are general characterizing parameters.[66]

4.4.6 Test for Boltzmann Superposition Principle Adherence

The Boltzmann superposition principle was applied to the creep data with the objective of predicting the recovery and establishing whether the NP tissue creep behavior could be approximated as linearly viscoelastic. The recovery strain was predicted with an equation based on the Boltzmann superposition principle and employed the Andrade creep model. The form of the Boltzmann superposition used was $\gamma_r(t) = \gamma_{creep}(t) - \gamma_{creep}(t-\theta)$ (equation 2.4 from Section

2.3.4), where t is the independent time variable and θ is the duration of the creep experiment. Assuming that instead of stopping the initial creep stress at time t = θ, an additional creep stress of equal magnitude and opposing direction is applied at that time, then the sum of the two stresses is zero starting at time, t = θ. Recalling from the definition of the shear creep compliance that $\gamma(t) = \tau J(t)$ and inputting this into equation 2.4, it may be seen that

$$\gamma_r(t) = \tau J(t) - \tau J(t-\theta). \quad (4.8)$$

Substituting the Andrade creep model (equation 2.15) into equation 4.8 for J(t) and simplifying, the recovery strain prediction equation is obtained,

$$\gamma_r(t) = \tau\beta[t^{1/3} - (t-\theta)^{1/3}] + \tau\theta/\eta. \quad (4.9)$$

The prediction was performed initially using the manually fit Andrade parameters and then compared with the Andrade parameters determined via the computer-assisted fitting. The recovery was also predicted using the Nutting model with parameters determined through the computer assisted fitting, where the 1/3 power was replaced with *n* in equation 4.9, producing the Nutting form of the prediction equation,

$$\gamma_r(t) = \tau\beta[t^{n} - (t-\theta)^{n}] + \tau\theta/\eta. \quad (4.10)$$

Once the recovery strain was predicted, it was plotted on axes of strain versus time along with the actual recovery strain for visual comparison. Percent error was calculated between the actual and predicted recovery strain at each time increment and plotted versus time for each prediction. The percent error was calculated by

$$\%Error = 100 * \left(\frac{AcceptedValue - TestedValue}{AcceptedValue} \right), \quad (4.11)$$

where the data points represented the accepted value and the prediction was tested. In addition, the SSE and R^2 values were calculated for each specimen prediction and average values were determined to quantify the overall prediction accuracy.

4.4.7 Analysis of Isochronal Creep Data on Linear Axes of Strain Versus Stress

The objective of the isochronal creep analysis was to determine if the lines of isochronal data (data at constant time) were linear or curved, serving as another indicator of whether the material was linearly or nonlinearly viscoelastic. Isochronal data points were plotted on linear axes of strain versus stress at times of 10.18, 30.25, 60.56 and 101.5 seconds. The slope of each isochronal line represented the creep compliance of the specimen at that particular time for the different levels of applied stress. Recall that if the isochronal lines are linear, the compliance is constant for all of the applied stresses at that particular time and the material is linearly viscoelastic. If the isochronal lines are curved, then the compliance is dependent on the applied stresses at that particular time, implying that the material is nonlinearly viscoelastic. For each set of isochronal data points, a linear regression and a second order polynomial regression were fit to the data producing linear and curved variants of isochronal lines. The R^2 and adjusted-R^2 values of each fit were compared as a measure of whether the lines of isochronal data were linear or curved. The adjusted-R^2 value adjusts for the number of terms in the model since the standard R^2 always increases as the number of model terms increase. In addition, the coefficients of the regression terms and concavity of the isochronal lines were compared.

4.4.8 Analysis of Isochronal Data on Log-Log Axes of Strain Versus Stress

Upon establishing nonlinear viscoelasticity in the specimen via curved isochronals (on linear axes of strain versus stress), it becomes necessary to determine whether the nonlinearity is

separable from the time-dependent component of deformation. This may be revealed using a plot of the isochronal data on log-log axes of strain versus stress. In this case, if the lines of isochronal data are straight and all have the same slope, the material may be said to possess an inherently nonlinear component that is independent of time.

To better understand this, first consider what is implied by a linear isochronal data line on standard linear axes of strain versus stress. For an applied stress, τ, and a creep strain response, $\gamma_c(t)$, the line of slope, K, goes through the origin and may be approximated by the equation

$$\gamma_c(t) = K(t)\tau. \tag{4.12}$$

Now, let the isochronal data be curved rather than linear, while still passing through the origin. Initially, it is reasonable to assume the curved line is approximated by the equation

$$\gamma_c(t) = K(t)\tau^m, \tag{4.13}$$

where higher orders of stress, τ^m, are accounted for to produce the curved shape.[93] Taking the common log of both sides produces an equation of the form

$$\log(\gamma_c) = m\log(\tau) + \log(K). \tag{4.14}$$

If the result is a straight line of slope, m, when plotted on log-log axes of strain versus stress, the power law of equation 4.13 is appropriate. If the slope, m, of an isochronal line is the same for all of the isochronal lines (i.e., if the lines are parallel) when plotted on log-log axes of strain versus stress, then the higher order stress component, τ^m, is independent of time.[93]

In order to determine the value of *m* from the experimental data, the creep strain, γ_c, must be calculated from the experimentally determined strain, γ, and the instantaneous strain, γ_o, where $\gamma_c = \gamma - \gamma_o$. This, in turn, requires the determination of the instantaneous strain, γ_o, from the relation $\gamma_o = J_o\tau$ (assuming the instantaneous elastic deformation of the material is ideal).[93] For relatively low applied stresses and initial strains, $\gamma_o = J_o\tau$ is an acceptable approximation in

many polymeric materials. However, for larger strains, a nonlinear approximation (e.g., exponential) may be more appropriate.[93] In reality, these quantities representing the instantaneous response, γ_o and J_o (sometimes referred to as the glassy compliance, J_g), are mathematical idealizations and exhibit a time-dependent response as well.[94]

Given the innate error that results from combining the assumptions relating to γ_o, the value of J_A supplied by the computer-assisted curve fits of the Andrade creep model to 6 Pa data was believed to provide the best estimate for J_o. Therefore, γ_c for each line of isochronal data was obtained from the difference in the measured strain and the product of the applied stress with the Andrade intercept compliance, $\gamma_c = \gamma - J_A\tau$. The slope, *m*, was obtained at times of 10.18, 30.25, 60.56, 101.5, 301.4, 851.9, and 1009 s by fitting the power law in equation 4.13 to the isochronal data in an Excel spreadsheet. Observations regarding parallelism of the slope were recorded. For slight deviations within experimental error, the slope, m, was assumed to be approximately constant[93] and the average slope was calculated.

4.4.9 Strain Prediction at Stresses of 18 Pa and 54 Pa

Creep strain was predicted for tests performed at stresses of 18 Pa and 54 Pa. Model parameters were established from lines of isochronal data and from compliance data of 6 Pa creep tests. The objective was to provide a comparison between linear viscoelastic and QLV strain formulations of the Andrade creep model. The linear viscoelastic formulation is obtained from equation 2.1, $J(t) = \gamma(t)/\tau$, and equation 2.15, $J(t) = J_A + \beta t^{1/3} + t/\eta$, giving

$$\gamma(t) = \tau(J_A + \beta t^{1/3} + t/\eta), \qquad (4.15)$$

where J_A, β, and η are independent of stress. Although it was not explicitly stated, equation 4.15 is the strain formulation of the Andrade creep model input into the Boltzmann superposition principle (equation 2.4) used for prediction of recovery in Section 4.4.6.

The QLV strain formulation of the Andrade creep model was derived in the following manner. Starting with the Andrade creep model from equation 2.15, $J(t) = J_A + \beta t^{1/3} + t/\eta$, a more general form was sought such that equation 2.15 could also be dependent on stress. Preliminary analysis indicates that, on axes of compliance versus cube root of time, the creep curve is approximately linear with a slope, β, which varies with alterations in the applied stress. According to Ferry, similar behavior has been documented by Van Holde for Andrade creep of nitrocellulose, where the viscoelastic behavior is not linear.[69] Assuming that the slope is dependent on stress, $\beta = \beta(\tau)$, we obtain

$$J(t,\tau) = J_A + \beta(\tau)\, t^{1/3} + t/\eta \qquad (4.16)$$

Recall that t/η is responsible for all permanent deformation acquired during a creep experiment and β is fully recoverable. It is reasonable to assume that the viscosity, η, is independent of the stress and approximately constant since the strain (shear) rates associated with the creep deformation are generally low in the absence of yielding. Validity of this assumption has also been observed preliminarily in the experimental data. To facilitate algebraic manipulation, assume that the time, t, is sufficiently small such that viscous effects may be neglected, $t/\eta \cong 0$. Then, the stress dependent creep compliance becomes

$$J(t,\tau) = J_A + \beta(\tau)\, t^{1/3}. \qquad (4.17)$$

Based on the assumption of an ideally elastic instantaneous strain, $J_o = \gamma_o/\tau$,[93,94] the Andrade intercept compliance is independent of stress, where $\gamma_A = J_A\tau$ produces

$$\gamma(t,\tau) = \gamma_A + \tau\beta(\tau)t^{1/3}. \qquad (4.18)$$

This is comparable to the form used by Van Holde in equation 2.13, $\varepsilon(t) = \varepsilon_o + \beta' t^{1/3}$.[69,76] Subtracting out γ_A using $\gamma_c(t,\tau) = \gamma(t,\tau) - \gamma_A$ and rewriting equation 4.18 produces

$$\gamma_c(t,\tau) = \tau\beta(\tau)t^{1/3}. \tag{4.19}$$

Equation 4.19 is reminiscent of a nonlinear strain formulation attributed to Nutting,

$$\gamma_c(t,\tau) = \gamma(t,\tau) - \gamma_o = A\tau^m t^n,^{(66,93)} \tag{4.20}$$

where the power, n = 1/3, makes equation 4.20 specific to Andrade in the current context. Then, by setting $\gamma_c(t,\tau)$ in equation 4.19 equal to $\gamma_c(t,\tau)$ in equation 4.20 results in

$$\gamma_c(t,\tau) = A\tau^m t^{1/3} = \tau\beta(\tau)t^{1/3} \tag{4.21}$$

Canceling out the cube root of time, $t^{1/3}$, from the expression and solving for $\beta(\tau)$ gives

$$\beta(\tau) = A\tau^{m-1}, \tag{4.22}$$

where the coefficient, A, and the power, m, are constants and, thus, independent of stress. Referring back to equation 4.20 and setting $At^{1/3} = K(t)$ produces the power law used in equation 4.13 of Section 4.4.8, $\gamma_c(t,\tau) = K(t)\tau^m$. Since the time-dependent viscoelastic behavior of equation 4.13, K(t), is separable from the nonlinear elastic stress response, τ^m, the resulting model is representative of QLV behavior. Then, substituting equation 4.22, $\beta(\tau) = A\tau^{m-1}$, into equation 4.16 produces the QLV compliance formulation of the Andrade creep model,

$$J(t,\tau) = J_A + A\tau^{m-1} t^{1/3} + t/\eta. \tag{4.23}$$

It should be noted that the rheometer is unable to discriminate between stress dependences in the compliance data. Therefore, measured compliance values may be interpreted as $J(t) = \gamma(t)/\tau$ or as $J(t,\tau) = \gamma(t,\tau)/\tau$ without loss of generality of the actual data. According to $J(t,\tau) = \gamma(t,\tau)/\tau$, the QLV strain formulation of the Andrade creep model becomes

$$\gamma(t,\tau) = \tau J_A + A\tau^m t^{1/3} + \tau t/\eta, \tag{4.24}$$

which may be rewritten with $\tau J_A = \gamma_A$ as

$$\gamma(t,\tau) = \gamma_A + A\tau^m t^{1/3} + \tau t/\eta. \quad (4.25)$$

In order to perform the prediction of the strain using the linear viscoelastic (equation 4.15) and QLV (equation 4.24) formulations of the Andrade creep model, it was necessary to determine parameters for each of the models. Parameter values for J_A, β, and η were obtained from the results of Section 4.4.4, the computer assisted fit of the Andrade creep model to 6 Pa compliance data over the entire data range. The parameters J_A and η were the same for both the formulations. For the linear model, the β value was assumed to be independent of stress and the value determined from the fit to the 6 Pa compliance data was used in the prediction of strain for 18 Pa and 54 Pa. For the QLV model, it was assumed that the value obtained for $\beta(\tau) = \beta(6\text{ Pa})$ was unique to the 6 Pa creep experiment and different values of $\beta(\tau)$ would be obtained at other stress levels. Since it was determined from equation 4.22, $\beta(\tau) = A\tau^{m-1}$, that A and m are constants for QLV behavior, the 6 Pa value of $\beta(\tau)$ aided in determining the constant, A. Recall that the lines of isochronal data plotted on log-log axes of strain versus stress must be approximately parallel (and straight) in order to fit the form of equation 4.14, $\log(\gamma_c) = m\log(\tau) + \log(K)$. The m^{th} power of stress in equation 4.13, $\gamma_c(t) = K(t)\tau^m$ and equation 4.14 was determined from the slope of the isochronal data lines, as demonstrated in Section 4.4.8. The parameter, A, was then calculated and the parameters input into the models for strain prediction at 18 Pa and 54 Pa stresses. The models were compared using fit statistics (e.g., R^2, SSE) and graphically.

4.4.10 Analysis of Consecutive Creep Testing Data

An attempt was made to quantify the change in compliance observed between the first and second creep step, as well as the change from second to third and third to fourth creep steps. The objective of this analysis was to gain insight into the mechanism creating the change in compliance. Percent error, using equation 4.11, was calculated between each creep step from the experimental compliance levels at 300 s. Upon evaluating the error between two consecutive runs, the preceding compliance level was considered to be the "accepted value" since it had already been established and the ensuing compliance level was considered the "tested value." Percent error of the initial compliance change (from creep 1 to creep 2) was plotted versus pre-test recovery time to investigate effects associated with the length of recovery time prior to the start of testing. Note that, in this context, "pre-test recovery time" encompasses the elapsed time following installation of the specimen and leading up to the first full creep test whether data was being collected or not. This is acceptable because the rheometer torque was set to zero during this time, thus permitting the spindle to drift and the specimen to recover. Additionally, percent error of the initial compliance change was plotted versus the ending compliance level at 300s for the first creep step in order to investigate the possibility that observed changes in compliance level were dependent on the initial compliance level. The mean and standard deviation were also calculated for the percent error between each step from the first through the fourth step. However, it is necessary to note that, since percent errors determined using equation 4.11 are non-additive, the use of the mean (average) percent error in this context is provided as a qualitative measure of the overall error.

4.4.11 Analysis of Heat Transfer Through NP Tissue at 40 ºC

To accompany the temperature ramp testing of the tissue, a brief heat transfer analysis was performed to validate the assumption of a constant temperature distribution in the specimen. In other words, an attempt was made to verify that temperature gradients in the specimen were negligible although the ambient temperature surrounding the specimen was 22 ºC and the temperature of the Peltier plate was set to 40 ºC. This was accomplished using both analytical (hand calculations) and numerical (finite element) methods. General assumptions and thermal conductivities of the hand-calculation analysis are summarized in Table 4.6 while Figure 4.9 provides a schematic diagram. For the finite element analysis (FEA), detailed solid models of the stainless steel cone, aluminum shank, and mounted NP tissue sample were created using SolidWorks (SolidWorks Corp., Concord, MA). The FEA was performed using COSMOS, an integrated software module with the Solidworks program. Due to the low criticality of the analysis, Cosmos was chosen over other, more sophisticated FEA programs for efficiency. The FEA assumptions, boundary conditions, and model parameters are summarized in Table 4.7.

Table 4.6 Hand calculations: Basic simplifying assumptions and thermal conductivities used.

Basic Simplifying Assumptions	Thermal Conductivities
1-D conduction (neglect surrounding air)	k_{ss} = 15 W/m.K
Steady-state (neglect transient effects)	$k_{NP} = K_{water}$ = 0.631 W/m.K
Temperature of aluminum is 25 ºC	
S.S. cone and NP are both 6mm diameter right cylinders	
Thermal conductivity of NP is approx. same as water	

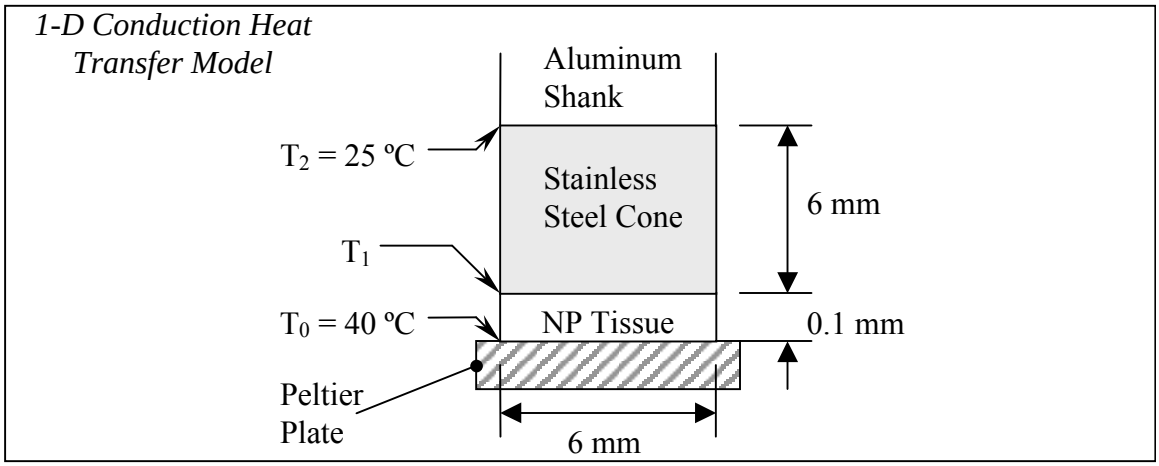

Figure 4.9 Schematic of 1-D conduction analysis.

Table 4.7 3-D FEA model: Assumptions, boundary conditions, and model parameters.

Component	Element Size and Type	Material and Thermal Conductivity	Boundary Conditions (BC)	General modeling assumptions
Aluminum shank	2.54 mm (0.1”) Tetrahedral	6061 Al: k_{Al} = 150 W/m.K	BC1: Specified temp. at Al shank top, T_t = 22 ºC BC2: Contact with cone BC3: Convection on all remaining outer surfaces	1. Steady state heat transfer 2. Bonded interface between any two materials (ideal contact boundary conditions) 3. Thermal conductivity of NP approx. equal to water 4. Ambient convection temperature (22º C) 5. Negligible convective heating and radiation from Peltier plate
Stainless steel cone	1.14 mm (0.045”) Tetrahedral	316 SS: k_{ss} = 15 W/m.K	BC1: Contact with shank BC2: Contact with NP BC3: Convection on all remaining outer surfaces (ignored cone fastening holes)	
NP tissue	0.16 mm (0.0063”) Tetrahedral	Water: $k_{NP} = K_{water}$ = 0.631 W/m.K	BC1: Specified temp. at NP-Peltier plate interface, T_p = 40ºC BC2: Contact with cone BC3: Convection on NP periphery	

5.0 RESULTS

5.1 VARIABLE STRESS TESTING DATA SET (N = 9)

5.1.1 General Observations

Figure 5.1 and Figure 5.2 show representative creep and recovery data on log-log axes of strain versus time. This data is also displayed on linear axes of strain versus time in Figure 5.3 and Figure 5.4. For each increase in stress by a factor of three, the strain is seen to increase by about 0.5 logarithmic units, as expected since $\log(3) \approx 0.5$. The log(strain) versus log(time) slopes of the curves are approximately the same for the 6, 18, and 54 Pa creep tests. The 162 Pa creep test also maintains approximately the same log-log slope as the other curves until it begins yielding, at which point it accelerates positively upwards. On linear axes of strain versus time, this behavior is intensified. The integrity of the 2 Pa creep run is suspect, as indicated by the artifact (slight downward perturbation) of unknown origin seen at about 300 s.

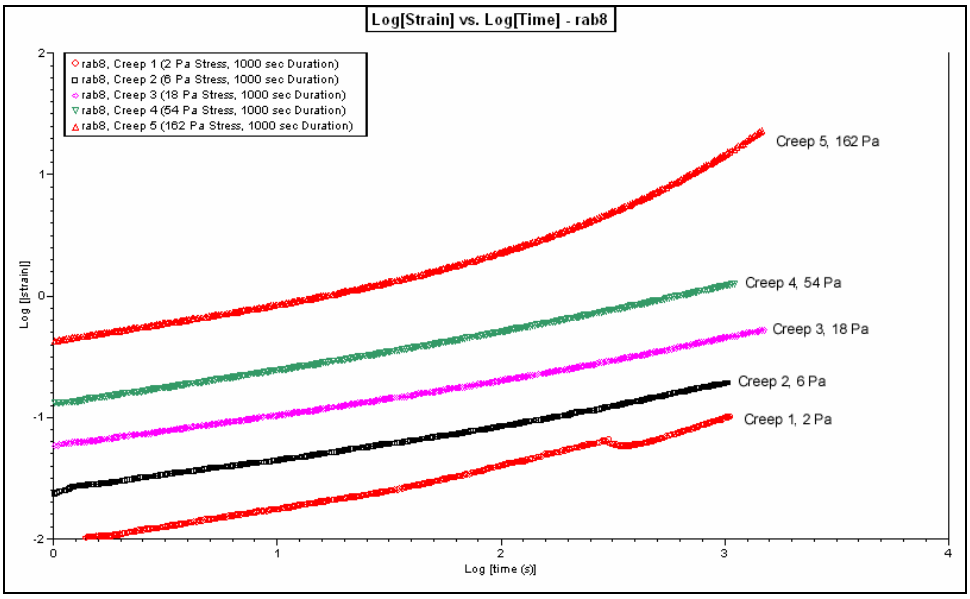

Figure 5.1 Creep data showing strain (absolute value) plotted versus time on log-log axes.
At about 300 s, a slight downward perturbation of unknown origin may be seen for the 2 Pa creep run. This behavior is an artifact and is not representative of actual material behavior. In addition, yielding may be observed for the 162 Pa creep run, starting at about 200 s.

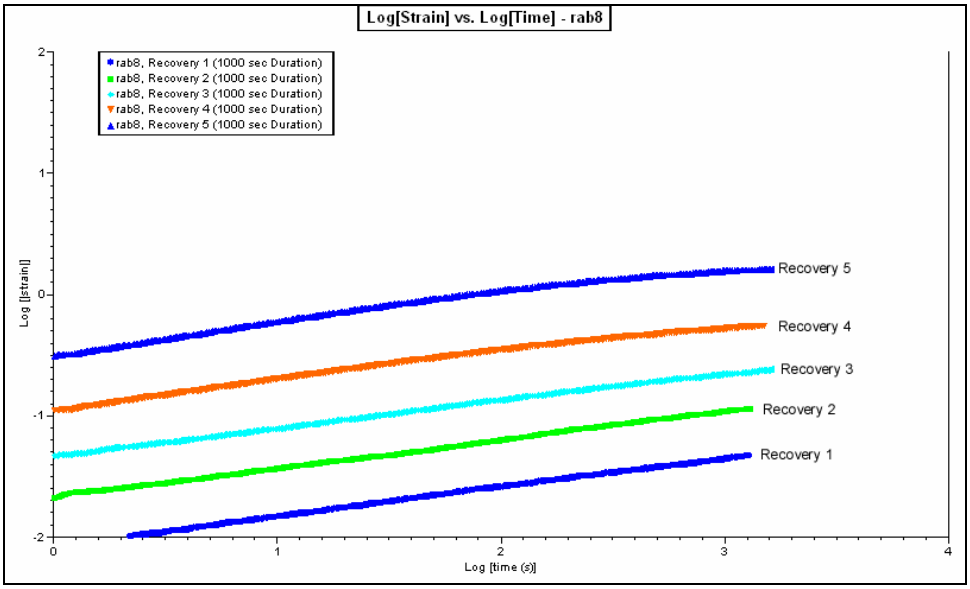

Figure 5.2 Recovery data showing strain (absolute value) plotted versus time (log-log axes).

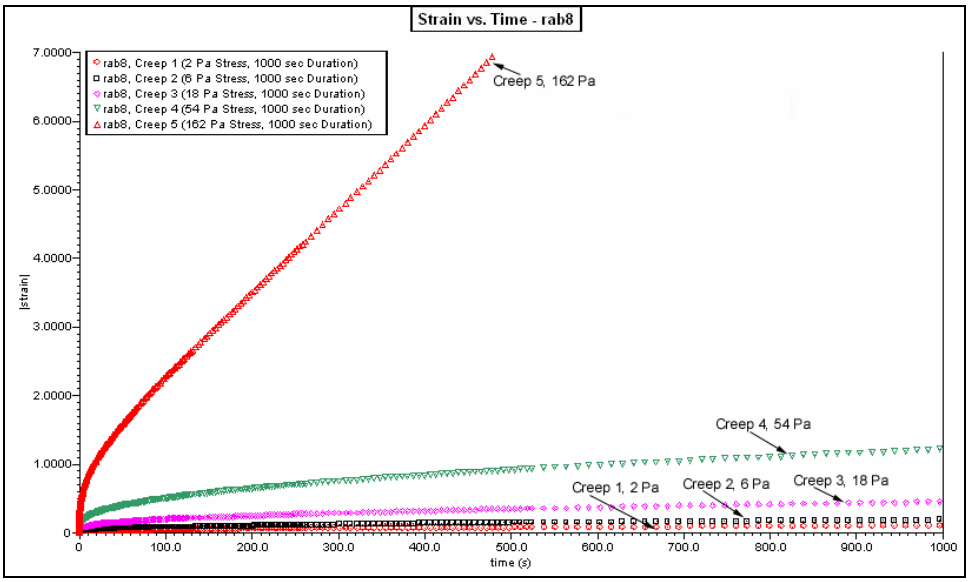

Figure 5.3 Creep data showing strain (absolute value) plotted versus time on linear axes.
Yielding is displayed for the 162 Pa creep run as a positive acceleration of the creep curve.

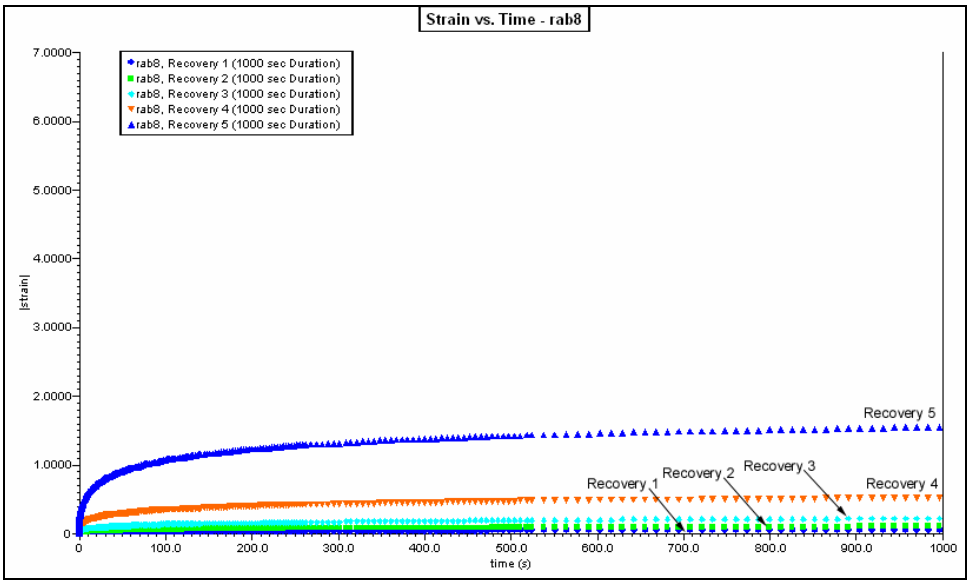

Figure 5.4 Recovery data showing strain (absolute value) plotted versus time on linear axes.

The representative creep and recovery data are also displayed on axes of compliance versus time. Figure 5.5 and Figure 5.6 show the data plotted on log-log axes while Figure 5.7 and Figure 5.8 show the data on linear axes. The data from the 2 Pa creep test is not displayed. The compliance data resembles the strain data, except the strain from each pair of creep and recovery steps is normalized by the corresponding creep stress. Recall that, by definition, compliance is the ratio of the time-dependent strain to the applied stress. Since the recovery stress is always zero, the rheometer calculates recovery compliance as the absolute value of the recovery strain divided by the associated creep stress. For example, the recovery compliance following the 6 Pa creep run is the recovery strain divided by the creep stress (6 Pa). On the log-log axes of compliance versus time, yielding is again identified for the 162 Pa stress through observation of a slope greater than unity. Recall that a slope of unity on log-log axes of compliance versus time indicates steady-state flow. In addition to the yielding, the specimen appears to display nonlinear viscoelastic behavior in general. This is identified by the unique creep curves for each stress both on linear and log-log axes of compliance versus time. However, disregarding the yielding of the 162 Pa creep run, the nonlinearity displayed by the other runs is not very severe. Further investigation is required to determine if this behavior may be approximated as linear.

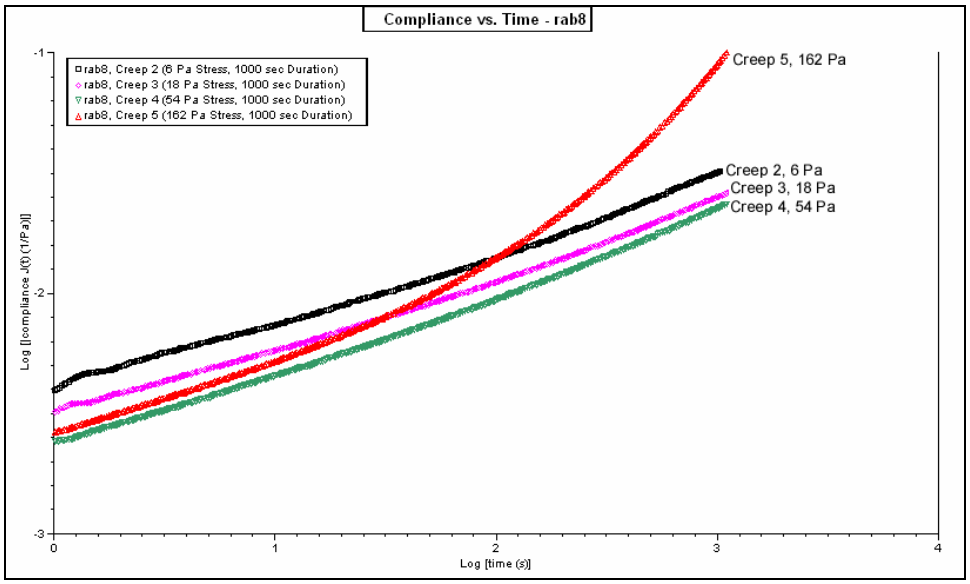

Figure 5.5 Creep data plotted on log-log axes of compliance versus time.

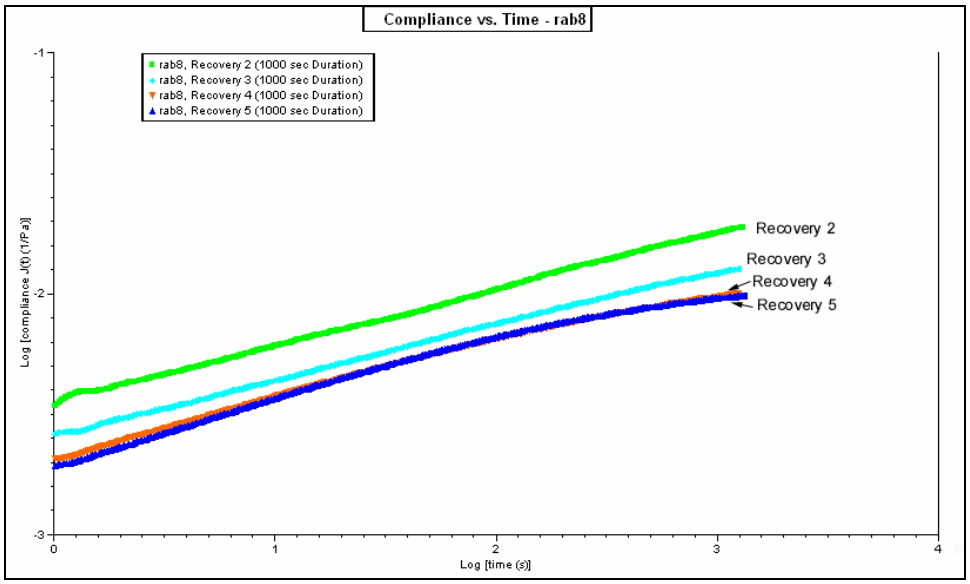

Figure 5.6 Recovery data plotted on log-log axes of compliance versus time.

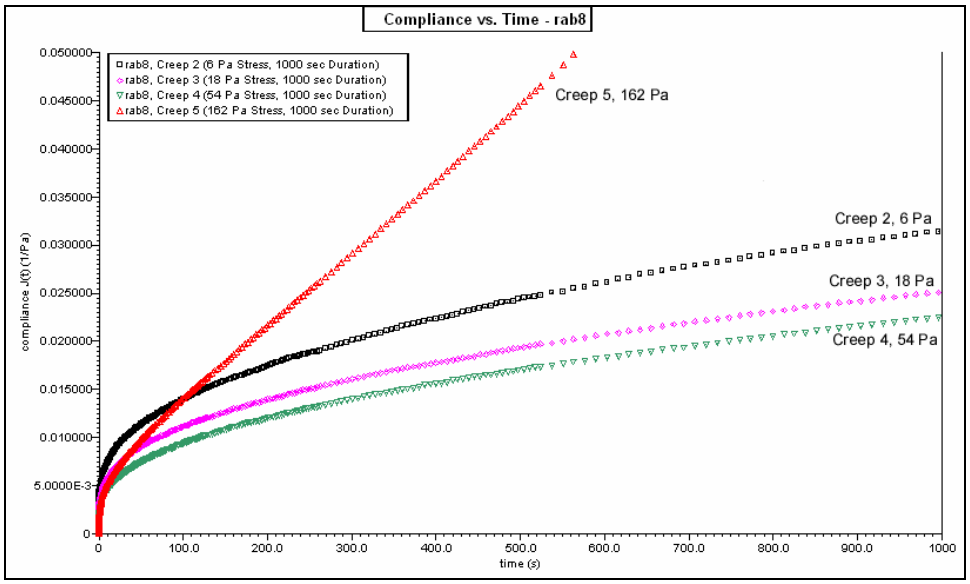

Figure 5.7 Creep data plotted on linear axes of compliance versus time.
Slight nonlinearity is evidenced by the unique creep compliance curves at each stress and strong nonlinearity is evidenced by the onset of yielding at the 162 Pa stress.

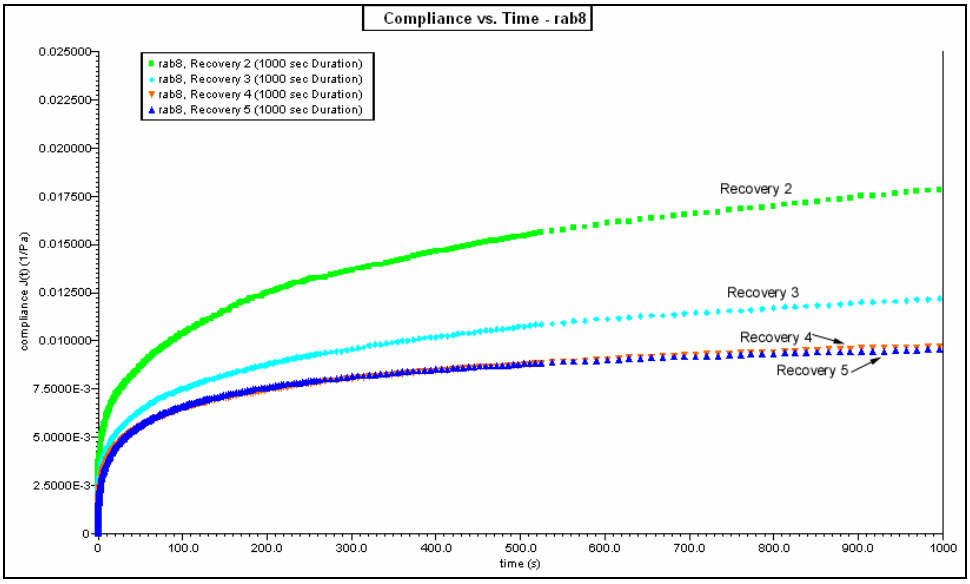

Figure 5.8 Recovery data plotted on linear axes of compliance versus time.

5.1.2 Creep Steps Performed at 2 Pa Shear Stress

Intermittently, an unusual phenomenon was observed for creep steps performed at 2 Pa such that tissue initially creeping in the positive direction would reverse and begin creeping in the negative direction despite the positive torque applied. This was an artifact of installation deformation or large stresses from a previous experiment that were not fully recovered and is not representative of actual material behavior at a 2 Pa shear stress. The behavior may be seen on log-log axes of strain versus time in Figure 5.9 and on linear axes in Figure 5.10. In the inset of Figure 5.10, the first 10 s of the strain data reveal that, at a 2 Pa shear stress, the material begins creeping in the positive direction but reverses and becomes negative thereafter.

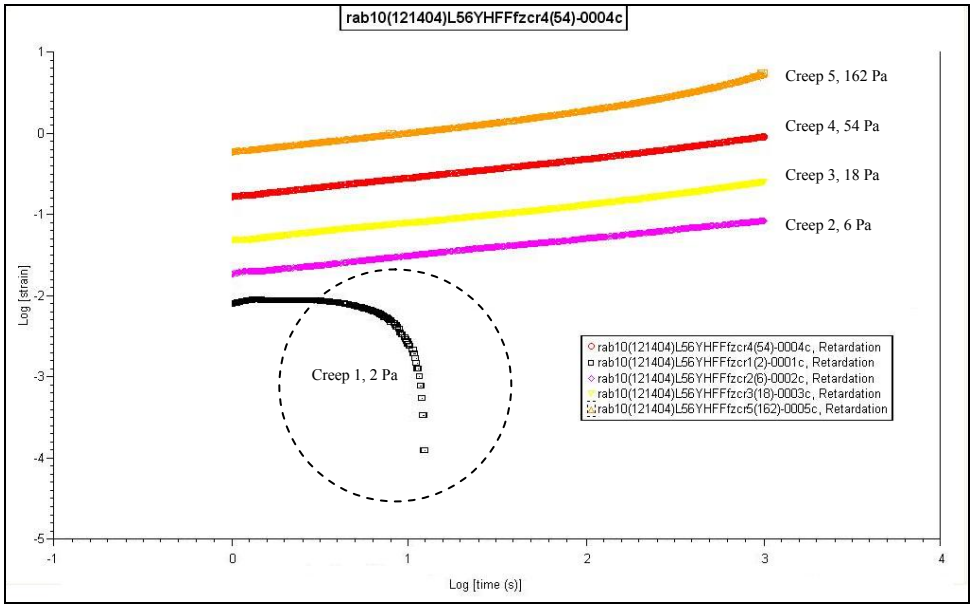

Figure 5.9 Plot of strain vs. time (log-log) portraying reversal of creep direction.
For the 2 Pa creep run, the reversal of creep direction is an artifact and is not representative of actual material behavior. It is believed that this behavior is a result of memory effects in the material due to installation deformation that has not been fully recovered out.

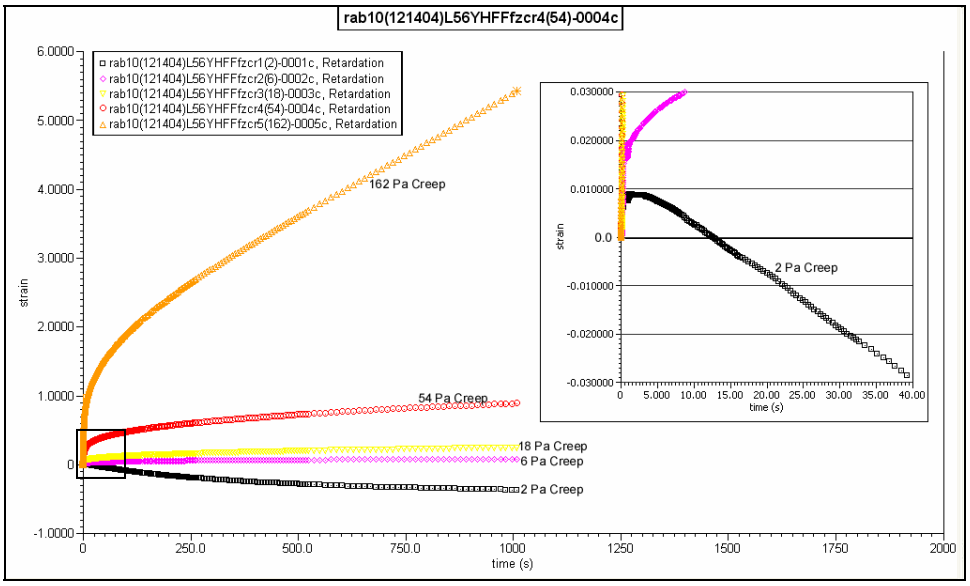

Figure 5.10 Linear plot showing creep strain versus time.
The 2 Pa stress creep run may be seen to change creep direction and result in negative strain values. In the inset, the change in creep direction is more clearly visible. This is not representative of actual material behavior.

5.1.3 Quasi-Linear Viscoelasticity (Factorization) Statistical Analysis Results

In the statistical analysis of the creep rate to determine if the tissue displayed quasi-linear viscoelasticity, creep rate variation from specimen to specimen was reduced by utilizing values at low levels of strain and at short times, where viscous processes were assumed to be negligible. This, in turn, reduced the standard deviation between the calculated creep rates and provided for a more realistic statistical comparison. Creep rates obtained at strains and times between 2 to 4 s are provided in Table 5.1 along with calculated statistical variables used in the analysis. The mean creep rates at each stress and corresponding standard deviations are shown in Figure 5.11. At lower stresses of 6, 18, and 54 Pa, the data was not statistically significant (i.e., $p >> 0.05$). At an applied stress of 162 Pa, the statistical significance was $p = 0.053$. These results and other outcome data of the multivariate analysis of variance (M-ANOVA) may be found in Table 5.2.

Table 5.1 Calculated creep rates from 2 to 4 seconds and statistical analysis variables.

	Creep Rates Corresponding to Applied Stress				Mean Stress Difference from 6 Pa		
Specimen	6 Pa	18 Pa	54 Pa	162 Pa	DF1 (18-6)	DF2 (54-6)	DF3 (162-6)
rab 4	0.264984	0.281167	0.275002	0.493574	0.016183	0.010018	0.22859
rab 6	0.252541	0.252471	0.227243	0.248902	-0.00007	-.025298	-0.00364
rab 8	0.255848	0.262914	0.277469	0.291565	0.007066	0.021621	0.03572
rab 9	0.223504	0.174739	0.216134	0.261775	-.048765	-0.00737	0.03827
rab 11	0.31799	0.272655	0.293704	0.322577	-.045335	-.024286	0.00459
rab 12	0.284327	0.230132	0.262588	0.381016	-.054195	-.021739	0.09669
rab 13	0.218933	0.251898	0.28235	0.259735	0.032965	0.063417	0.0408
rab 14	0.240028	0.2465	0.257781	0.265212	0.006472	0.017753	0.02518
rab 15	0.217587	0.230019	0.218059	0.237465	0.012432	0.000472	0.01988
mean	0.25286	0.244722	0.256703	0.306869	0.244722	0.256703	0.306869
std dev	0.033185	0.031386	0.029231	0.082919	0.031386	0.029231	0.082919

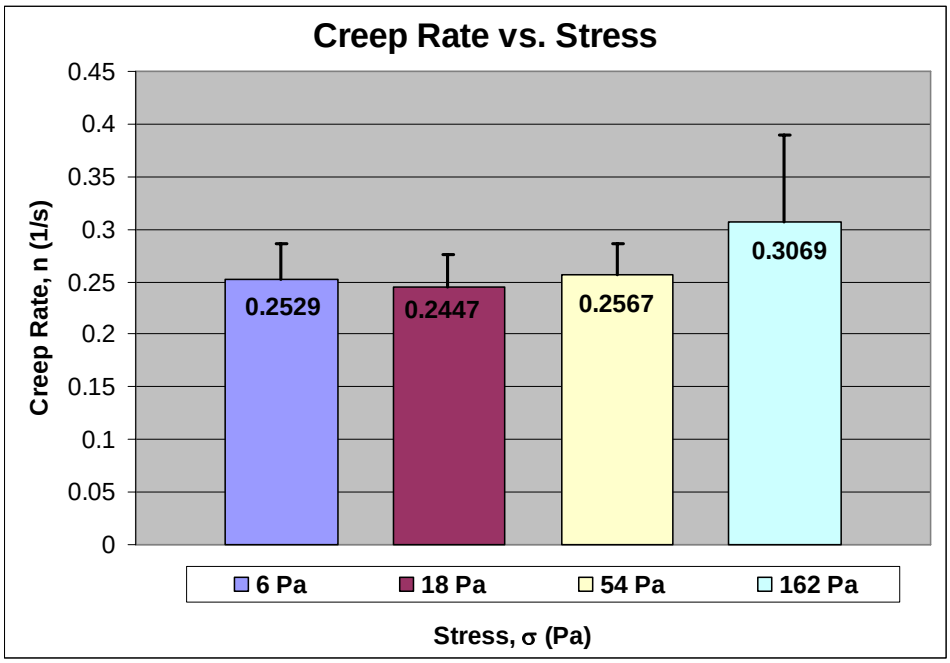

Figure 5.11 Mean creep rates at each applied stress and the associated standard deviation.
Data was statistically insignificant to suggest that mean creep rates differed at stresses of 6, 18, and 54 Pa, which is suggestive of quasilinear viscoelastic behavior. However, data was significant in indicating the mean creep rate differed for the 162 Pa stress, which is suggestive of more general nonlinear behavior.

Table 5.2 Statistical outcome data of QLV M-ANOVA. Statistical significance, *p*, is in bold.

Statistical Analysis Procedure: Multivariate Analysis of Variance (M-ANOVA)					
Dependent Variable: DIFF18 (Mean difference of 18 Pa and 6 Pa slopes)					
Source	Degrees of Freedom	Anova SS	Mean Square	F Value	**Pr > F, (*p*)**
INTERCEPT	1	0.00059613	0.00059613	0.57	**0.472**
Error	8	0.00836924	0.00104615		
Dependent Variable: DIFF54 (Mean difference of 54 Pa and 18 Pa slopes)					
Source	Degrees of Freedom	Anova SS	Mean Square	F Value	**Pr > F, (*p*)**
INTERCEPT	1	0.00013292	0.00013292	0.16	**0.6971**
Error	8	0.00652866	0.00081608		
Dependent Variable: DIFF162 (Mean difference of 162 Pa and 54 Pa slopes)					
Source	Degrees of Freedom	Anova SS	Mean Square	F Value	**Pr > F, (*p*)**
INTERCEPT	1	0.02625232	0.02625232	5.15	**0.053**
Error	8	0.04081855	0.00510232		

5.1.4 Critical (Yield) Strain Analysis

In the critical strain analysis, a total of twelve creep runs from nine rabbits were investigated for the presence of yielding. In four of the creep steps, no relative minimum velocity could be identified within the time scale of testing, suggesting that no yielding was present within these creep runs. However, the possibility remains that some or all of these specimens may have been on the verge of yielding at the completion of the creep run although a positive identification of yielding could not be made. In the remaining eight creep runs, yielding was positively identified resulting in a mean critical strain of $\gamma_{crit} = 2.79$ with a standard deviation of ± 1.05. The critical strain values for the individual specimens and other relevant data are provided in Table 5.3. Using the two-tailed Student's t-distribution at 95% confidence, the true mean of the critical strain was statistically determined to be 2.79 +/- 0.88. Restated, for a large population ($N \rightarrow \infty$)

of rabbit NP tissue tested using the methods applied here, there is a 95% probability that the mean critical strain is within the range of 1.91 to 3.67.

Table 5.3 Relevant critical strain data at time of yield inflection point.

Specimen Number	Stress, σ (Pa)	Time, t_y (s)	Strain, γ_c	Min. velocity, $\dot{\theta}_{min}$ (rad/s)	Min. velocity, $\dot{\theta}_{min}$ (deg/min)
rab4	18	111.3	1.4907	1.92E-04	0.6590
rab4	54	31.07	3.0636	1.82E-03	6.264
rab4	162	3.366	3.773	1.95E-02	67.07
rab6	162	9.357	4.0295	5.44E-03	18.70
rab8	162	206.4	3.5817	3.36E-04	1.154
rab12	54	98.24	1.1409	1.20E-04	0.4118
rab12	162	8.742	2.4619	5.66E-03	19.45
rab13	162	38.44	2.8126	1.25E-03	4.283
sample mean	-	63.36	2.79	4.29E-03	14.75
sample std dev	-	70.85	1.05	6.55E-03	22.51

Figure 5.12 displays two creep runs on linear axes of compliance versus time, where one creep run shows the slight presence of yielding while the other shows no yielding. The creep velocity versus time is plotted in the inset of Figure 5.12. Figure 5.13 shows the same data plotted on log-log axes of strain versus time. While it is difficult to precisely identify the onset of yielding on both log-log and linear axes of creep strain (or compliance) versus time, the location of the relative minimum on the plot of creep velocity versus time may be identified much more clearly, as seen within the plot inset. In addition, no minimum velocity may be identified for the other creep run as is expected since a positive acceleration of the creep compliance is clearly absent versus time. Thus, the palpable relative minimum located within the velocity versus time plot provides a suitable measure of the onset of yielding.

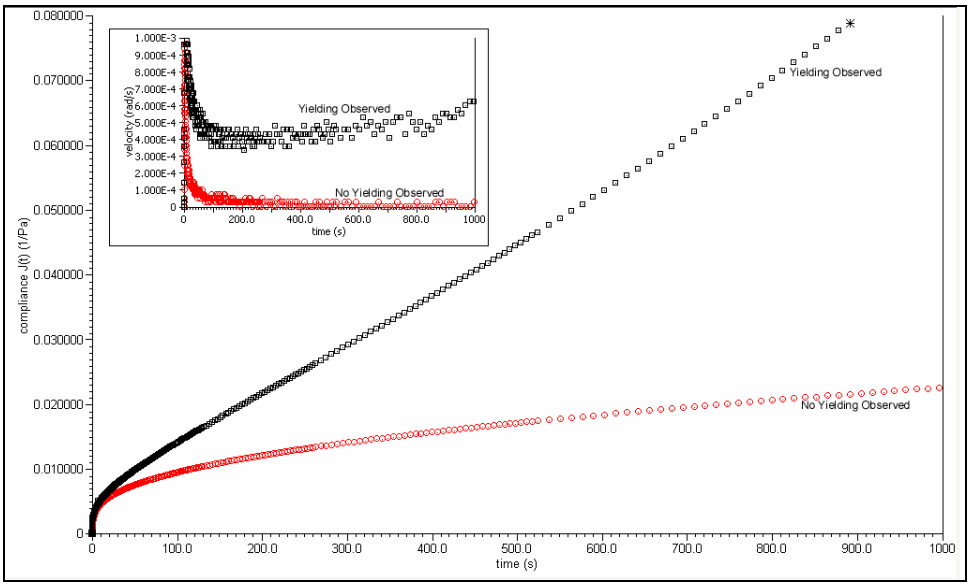

Figure 5.12 Yielding and non-yielding behavior on linear axes of creep compliance vs. time.
Creep compliance curve data displaying yielding is represented by black squares and non-yielding data is represented by red circles. The same data are provided in the inset plot on linear axes of angular creep velocity versus time. The start time of yielding occurs in the inset at the relative minimum in the creep velocity.

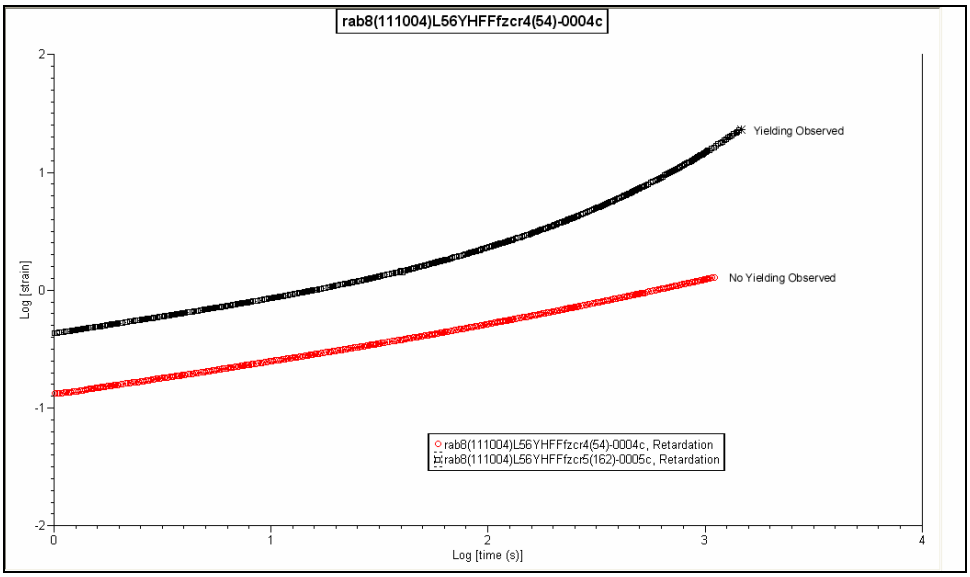

Figure 5.13 Log-log plot of strain versus time showing yielding and non-yielding.

5.2 MODELING ANALYSIS (N = 5)

5.2.1 General Andrade Creep Model Fitting

In order to successfully fit constitutive models to the data and obtain meaningful results, it is first necessary to determine what data is acceptable for fitting and what data is undesirable. This is particularly necessary when few background materials are available indicating the appropriate models to start with, the methods for application of such constitutive models, or how to progress the improvement of the model, especially in creep and for small animal specimens as is the case of the current study. Acceptable, representative data was data that was free of artifacts and relatively well behaved. Specific undesirable qualities included data that exhibited creep reversal (or grossly enhanced creep) during the 2 Pa applied stress, abnormal oscillations, or an over-eagerness to display yielding at lower stresses. For example, one specimen that was rejected displayed yielding during the 18, 54, and 162 Pa tests, during the last of which it began to yield within three seconds of the start of creep. In addition, the 2 Pa creep test was discarded from all analyses and eliminated from future testing so the 6 Pa creep data was used as a starting stress for modeling the data. Ultimately, only 5 specimens of the 9 available from the variable stress testing data set were selected and utilized for fitting.

5.2.2 Computer Assisted Curve Fits

Curve fits were performed using the Matlab Curve Fitting Toolbox for both the Andrade creep equation and the more general Nutting creep equation, where $t^{1/3}$ is replaced with t^n. Table 5.4 provides model parameters and fit statistics for the Andrade creep equation. The fits are plotted with actual data in Figure 5.14. The mean R^2 value of the Andrade model fit for the five specimens was 0.9996, suggesting a strong fit for each of the specimens. The mean SSE value

was 3.849×10^{-6}. The curve fits applied using the Nutting equation are shown in Table 5.5. The fit statistics indicate a strong fit with a mean R^2 value of 0.9996 and a mean SSE of 3.44×10^{-6}.

Table 5.4 Andrade creep model fit statistics and parameters from curve fitting program.

Specimen	R^2	SSE	Slope, β ($\times 10^3$) [$Pa^{-1}.s^{-1/3}$]	Andrade Const., J_A ($\times 10^3$) [Pa^{-1}]	Viscosity, η ($\times 10^{-6}$) [Pa.s]
1 (Rab 8)	0.99979	2.82×10^{-6}	2.499	1.900	0.2024
2 (Rab 9)	0.99947	2.77×10^{-7}	0.5360	0.8912	0.6527
3 (Rab 12)	0.99951	7.22×10^{-6}	2.315	0.1109	0.1173
4 (Rab 13)	0.99944	6.71×10^{-6}	2.015	1.354	0.1184
5 (Rab 15)	0.99980	2.22×10^{-6}	2.586	2.924	0.3973
Mean	0.99960	3.85×10^{-6}	1.9902	1.4360	0.2976
Std Dev	0.00018	3.00×10^{-6}	0.8418	1.0594	0.2290

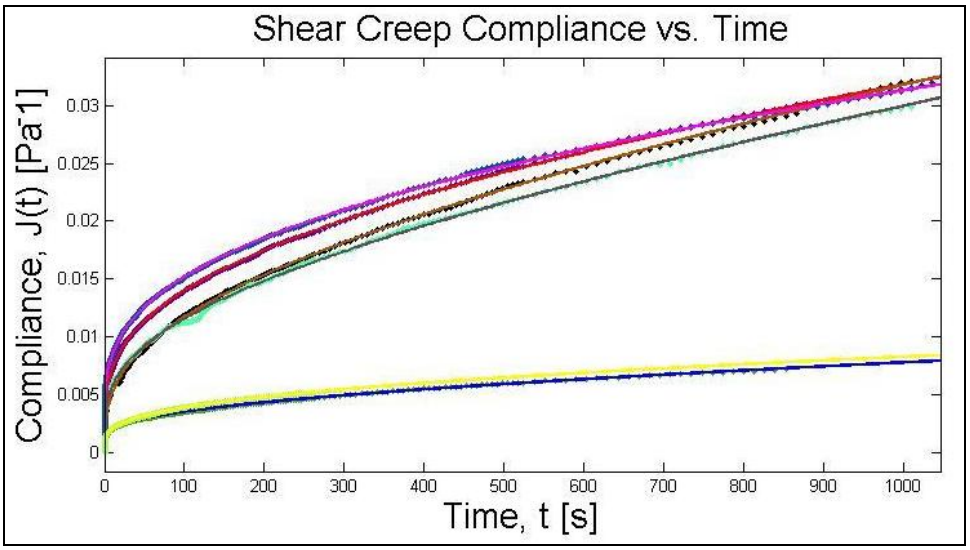

Figure 5.14 Andrade creep fits (lines) and associated data (dots) on linear axes.

Table 5.5 Nutting model fit statistics and parameters obtained with curve fitting program.

Specimen	R^2	SSE	Slope,β ($x10^3$) [$Pa^{-1}.s^{-n}$]	Andrade Const., J_A ($x10^3$) [Pa^{-1}]	Viscosity, η ($x10^{-6}$) [Pa.s]	Nutting Power, n
1 (Rab 8)	0.99984	$2.06x10^{-6}$	1.605	3.352	0.5227	0.4056
2 (Rab 9)	0.99954	$2.40\ x10^{-7}$	0.3113	1.255	1.7346	0.4255
3 (Rab 12)	0.99951	$7.09\ x10^{-6}$	1.908	0.7459	0.1352	0.3641
4 (Rab 13)	0.99953	$5.69\ x10^{-6}$	1.083	2.908	0.2142	0.4375
5 (Rab 15)	0.99981	$2.13\ x10^{-6}$	2.221	3.490	0.6481	0.3574
Mean	0.99965	$3.44\ x10^{-6}$	1.4257	2.3502	0.6510	0.3980
Std Dev	0.00016	$2.84\ x10^{-6}$	0.7511	1.2636	0.6418	0.03596

5.2.3 Comparison of Andrade and Nutting Models

In addition to individual fit statistics, comparison of the parameters obtained for the Andrade and Nutting creep models results in yet another evaluation of goodness of fit. The R^2 values for the Nutting model were consistently improved over the Andrade R^2 values, but by less than 0.01%. In comparing the SSE values, the Nutting model resulted in an average SSE improvement of 15%. Figure 5.15 shows the SSE value of both the Andrade and Nutting models for each specimen.

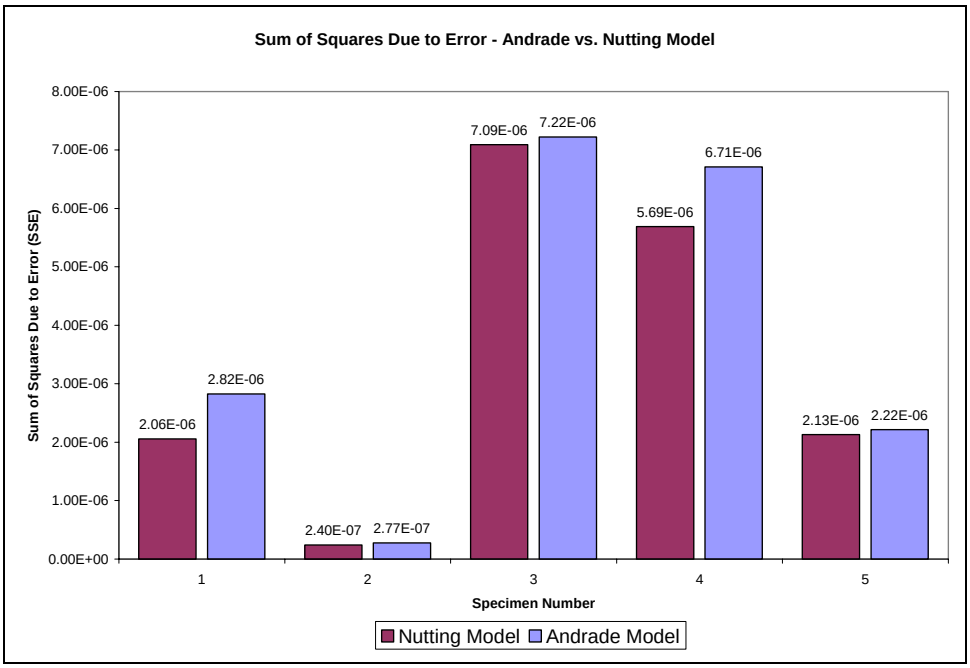

Figure 5.15 Comparison of SSE between Andrade and Nutting models.

The 95% confidence bounds for predicting compliance of both the Nutting and Andrade models are compact at ± 1% and ± 1.1% of the actual creep compliance, respectively. In other words, 95% of the compliance values predicted by either the Nutting or Andrade models would fall within about ± 1.5% of actual data. Figure 5.16 shows an enlarged segment of the actual compliance data, model curves, and associated model confidence bounds. A slight improvement in the confidence bounds of the Nutting model over the Andrade model may be seen at approximately 0.1%.

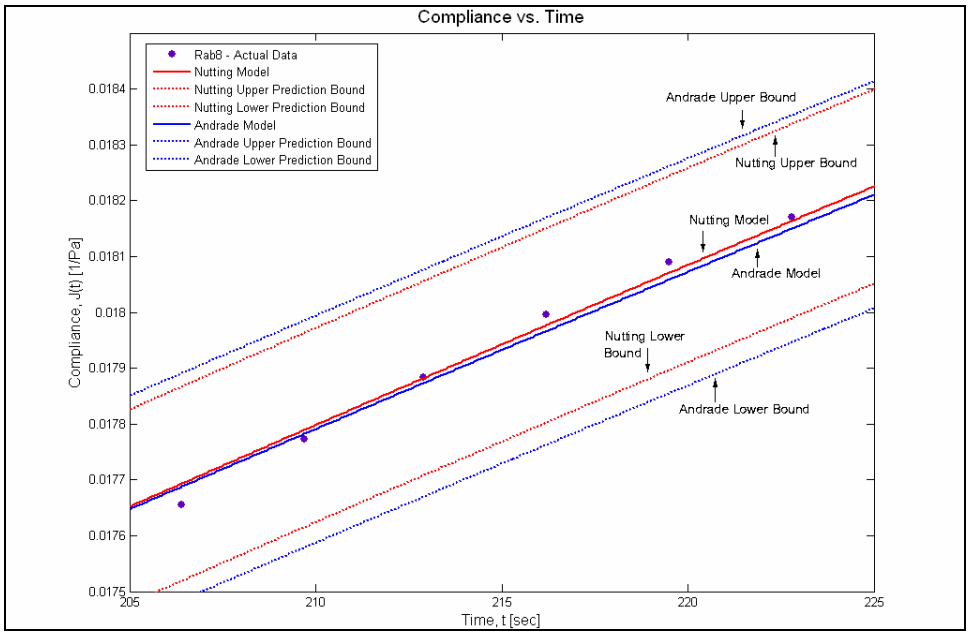

Figure 5.16 Compliance vs. time plot of data with Andrade and Nutting models.
Various components are represented as follows: actual data (coarse dots), Andrade model curve (blue solid line), Nutting model curve (red solid line), and associated model confidence bounds (fine dashed lines).

5.2.4 Extrapolation of Entire Data Range as a Measure of Model Performance

Using model parameters obtained from the first 300 s of data with nonlinear least squares regression, which minimized the modeling error over the indicated range, the models were used to extrapolate the remaining 700 s of data. Results of the extrapolation analysis are provided in Figure 5.17 through Figure 5.21. The attempt to extrapolate data using the logarithmic and exponential models was only performed for the first two specimens since it was immediately obvious that neither of these two models were suitable.

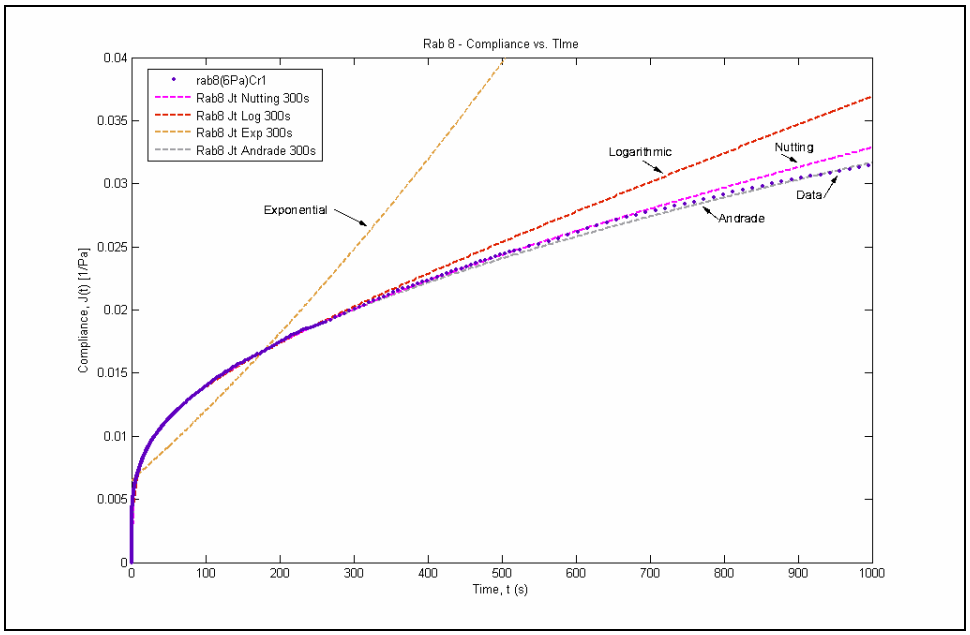

Figure 5.17 Extrapolation of model based on first 300 s of data for *rab 8*.

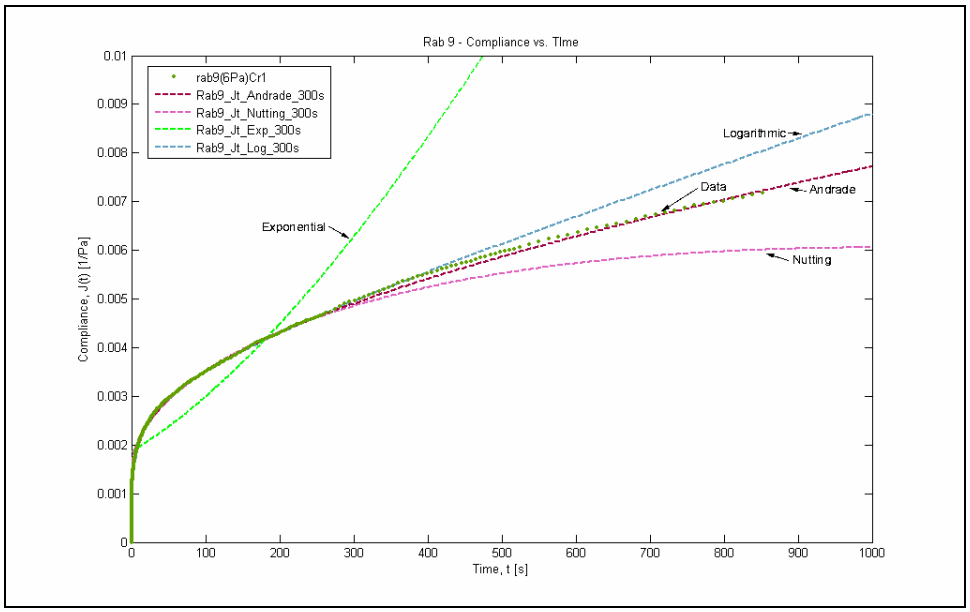

Figure 5.18 Extrapolation of model based on first 300 s of data for *rab 9*.

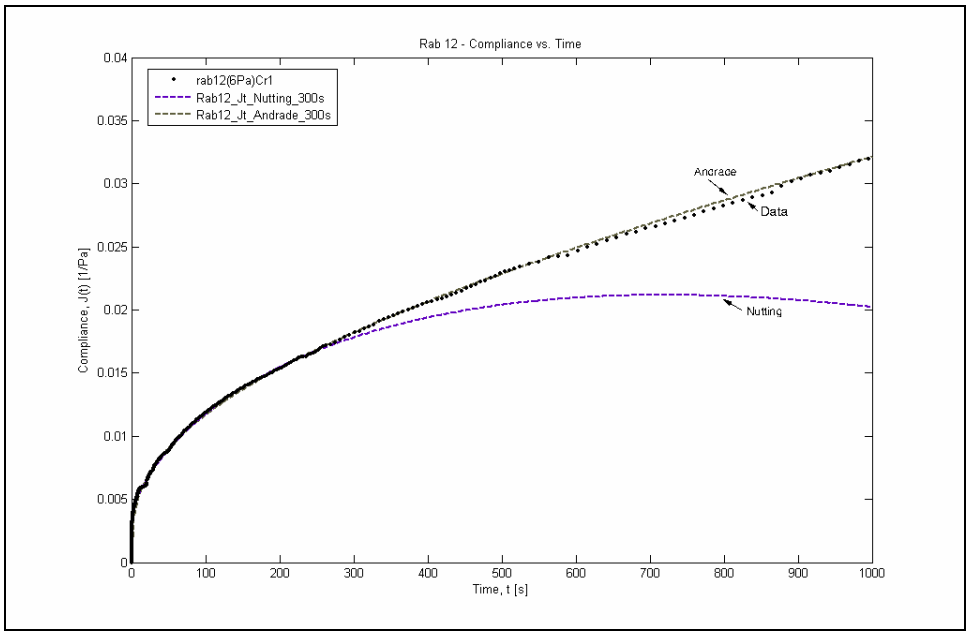

Figure 5.19 Extrapolation of model based on first 300 s of data for *rab 12*.

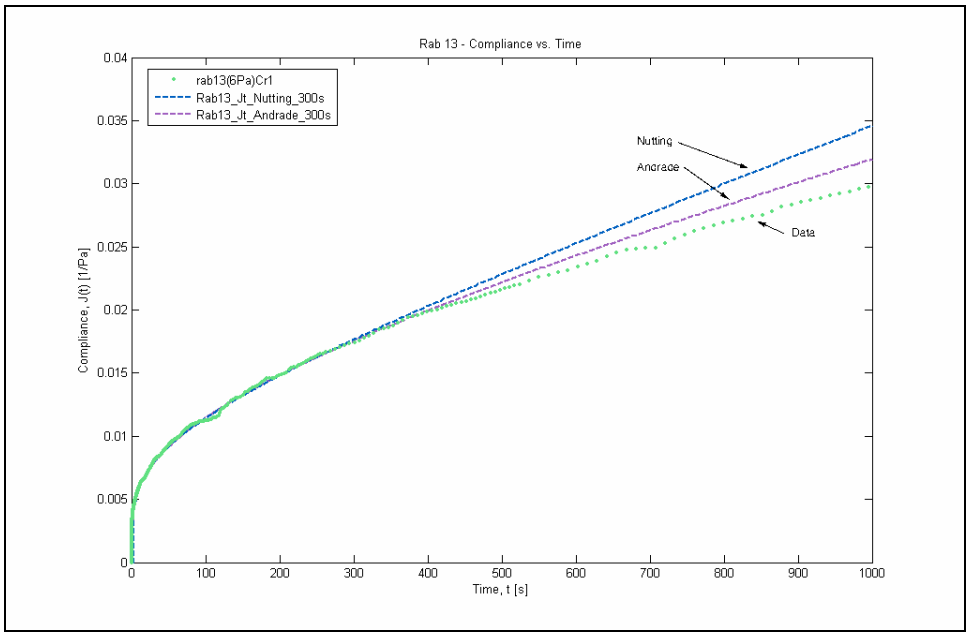

Figure 5.20 Extrapolation of model based on first 300 s of data for *rab 13*.

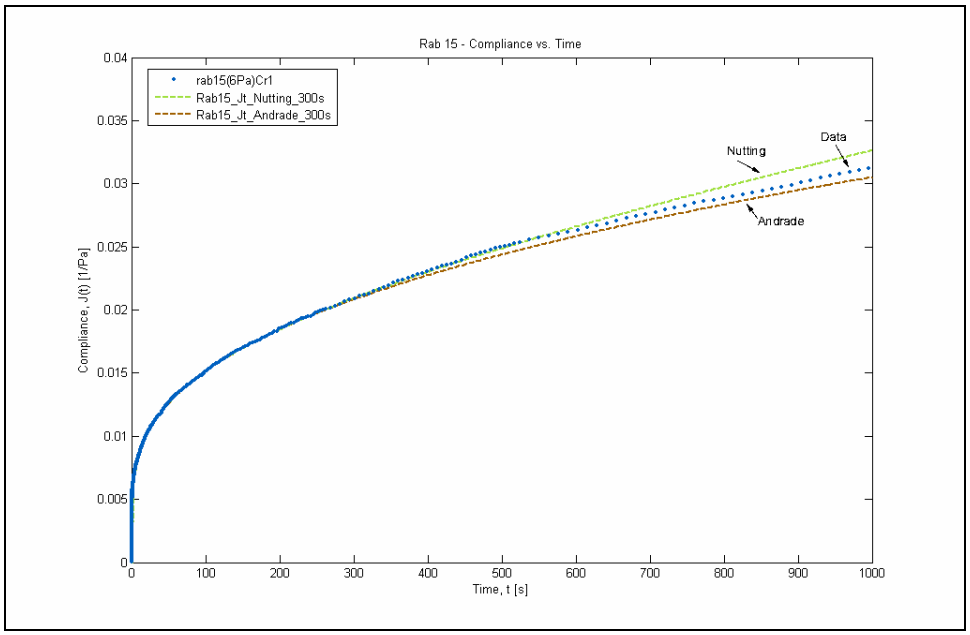

Figure 5.21 Extrapolation of model based on first 300 s of data for *rab 15*.

5.2.5 Boltzmann Superposition Principle Adherence

The attempt to predict recovery based on the Boltzmann superposition principle produced varied results but, in general, the recovery was not predicted well. The prediction using the computer fit Andrade model resulted in an average R^2 value of 0.8484 and standard deviation of 0.1859. The corresponding average SSE was 0.01401 with a standard deviation of 0.00791. Prediction results using the Nutting model, consequently, have been omitted since it produced increased prediction error over the Andrade model. Figures 5.22 through 5.26 show plots of both the predicted and actual data on axes of strain versus time. The R^2 and SSE values for the individual specimens are provided in the figure captions.

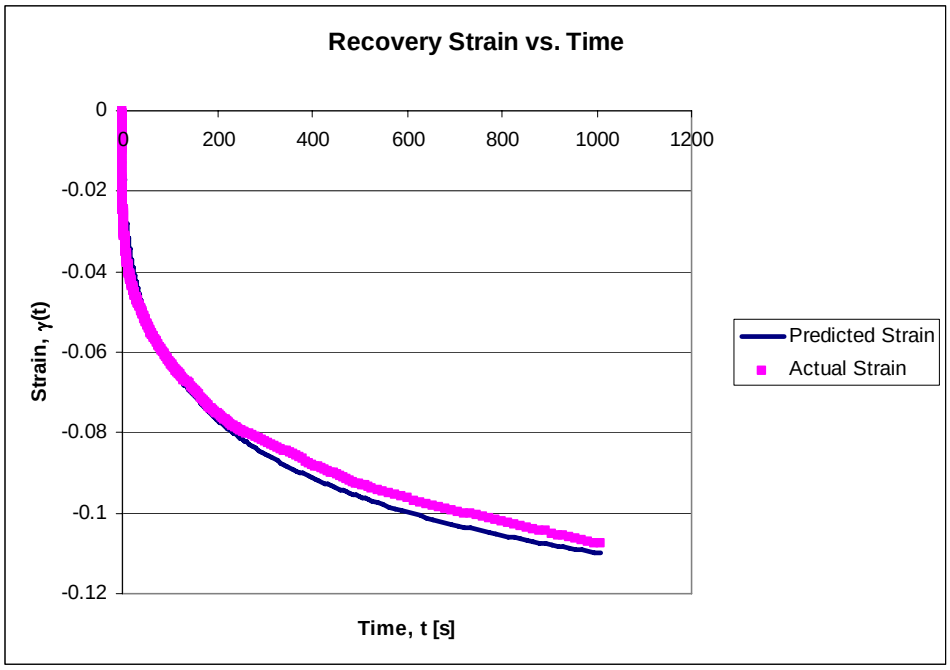

Figure 5.22 Actual and predicted recovery for *Rab 8*. R^2 = 0.9816, SSE = 0.00518.

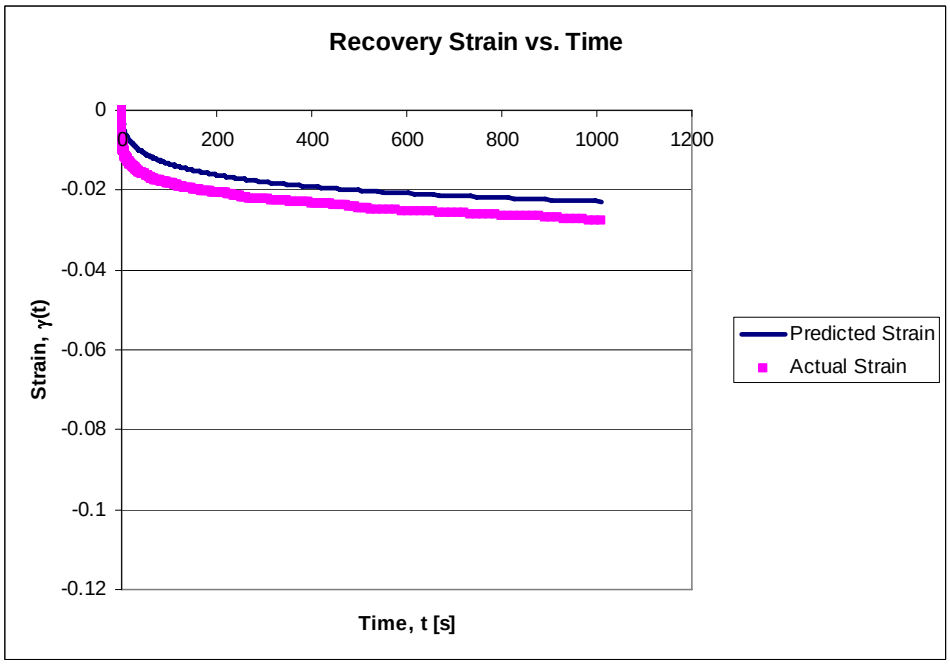

Figure 5.23 Actual and predicted recovery for *Rab 9*. R^2 = 0.5264, SSE = 0.00770.

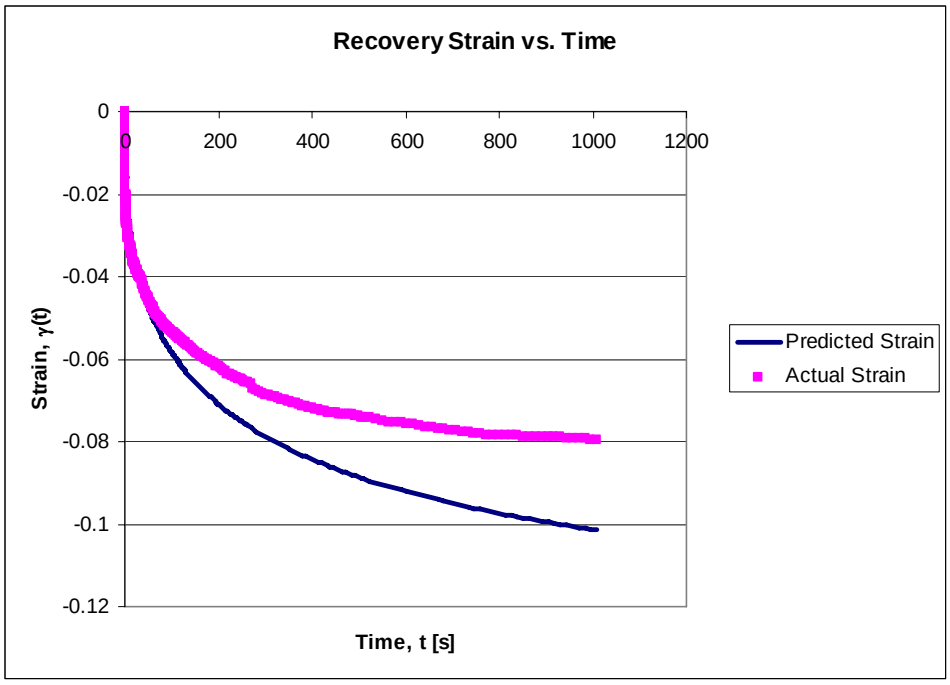

Figure 5.24 Actual and predicted recovery for *Rab 12*. R^2 = 0.8551, SSE = 0.02495.

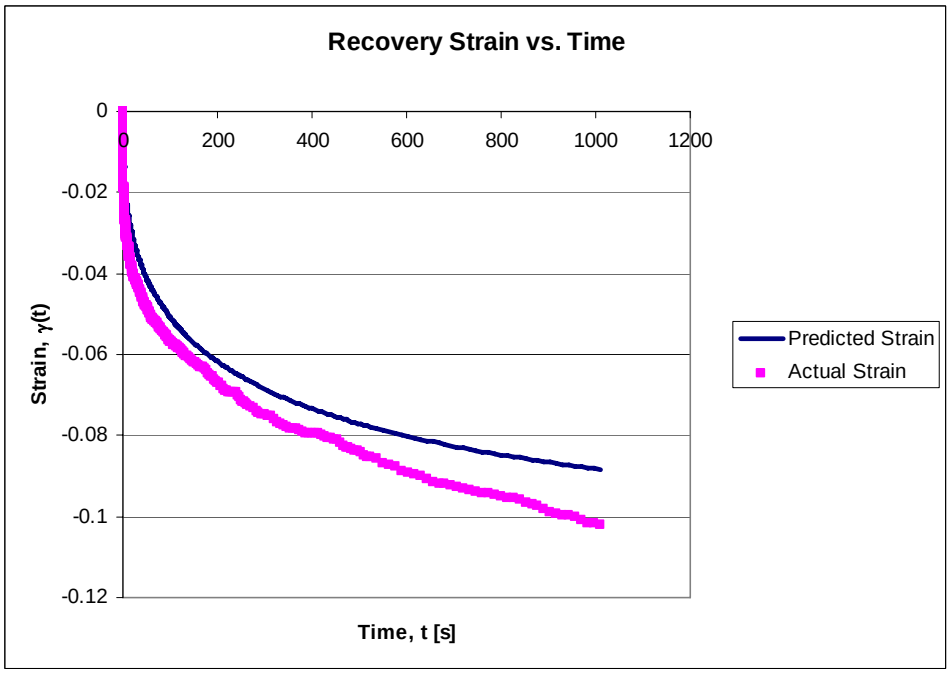

Figure 5.25 Actual and predicted recovery for *Rab 13*. R^2 = 0.9304, SSE = 0.01748.

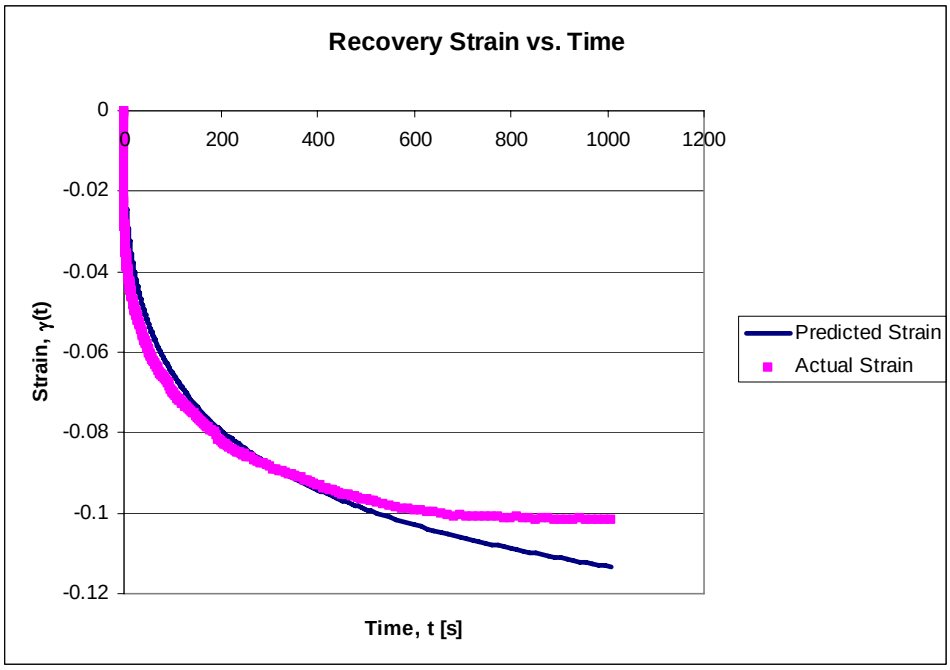

Figure 5.26 Actual and predicted recovery for *Rab 15*. R^2 = 0.9483, SSE = 0.01472.

5.2.6 Isochronal Data Analysis on Linear Axes

Isochronal data points were plotted on linear axes of strain versus stress at times of 10.18, 30.25, 60.56 and 101.5 seconds. For each data set, a linear regression and a second order polynomial were fit to the data. The R^2 and adjusted-R^2 values of each fit were compared as a measure of whether the lines of isochronal data were linear or curved (i.e., include higher order terms). Numerical results regarding isochronal data at 10.18 seconds are provided in Table 5.6. Results for isochronal data at greater times are provided in Appendix B since linearity is most likely to occur at short times. It may be seen that the polynomial fits produce a higher adjusted-R^2 value than the linear fits, with the exception of Rab 15, indicating that the lines of isochronal data are curved. The polynomial fits for Rab 15 showed slightly concave curvature, suggestive of an increased stiffness with increasing stress at a given time, which was atypical of the remaining

four specimens analyzed and all other specimens in general. Graphical results of the isochronal data analysis on linear axes are shown in Figures 5.27a through 5.31a. Given that yielding was identified in Rab 12 at a stress of 162 Pa within 10.18 s, the 162 Pa stress data point was ignored for this specimen. Intrinsic viscoelastic nonlinearity of the tissue is thus implied although more data points may further validate this argument since the curvature of the lines is minor.

Table 5.6 R-squared and adjusted R-squared values for isochronal data regressions.
R^2 and R^2_{adj} values for linear and quadratic regressions performed on isochronal data at 10.18 s are provided. The regressions are for isochronal data plotted on linear axes of strain versus stress. The quadratic fit has predominantly higher R^2_{adj} values indicating that the isochronal lines are curved rather than straight. This suggests that the tissue is intrinsically nonlinear viscoelastic. A comprehensive table in Appendix B includes R^2 and R^2_{adj} values at times of 10.18, 30.25, 60.56, and 101.5 s.

Specimen	Time	Linear Fit R^2	Quadratic Fit R^2	Linear Fit R^2_{Adj}	Quadratic Fit R^2_{Adj}
Rab 8	10.18 s	0.9962	0.9978	0.9962	0.9967
Rab 9	10.18 s	0.9923	0.9999	0.9923	0.9999
Rab 12	10.18 s	0.9869	0.9999	0.9913	0.9999
Rab 13	10.18 s	0.9922	0.9999	0.9922	0.9998
Rab 15	10.18 s	0.9936	0.9955	0.9936	0.9933
Average	-	0.9922	0.9986	0.9931	0.9979
Std Dev	-	0.0034	0.0020	0.0019	0.0029

5.2.7 Isochronal Data Analysis on Log-Log Axes

Isochronal data points were plotted on log-log axes of strain versus stress at times of 10.18, 30.25, 60.56, 101.5, 301.4, 851.9, and 1009 s. For each data set, a power law regression was fit to the data and the slope of the line corresponding to the value of the power, m, was recorded. The average slope was calculated to account for slight deviations, although the slopes of the isochronal data lines were approximately constant in general. Results of the determination of the

power, m, are provided in Table 5.7. Graphical results of the isochronal data analysis on log-log axes are shown in Figures 5.27b through 5.31b.

Table 5.7 Stress power, m, obtained using isochronal data on log-log axes of strain vs. stress.

Time	Stress power, m, corresponding to specimen number				
	Rab 8	Rab 9	Rab 12	Rab 13	Rab 15
10.18 s	0.6902	1.0738	1.1793	1.163	0.3395
30.25 s	0.7386	1.1109	1.2235	1.1564	0.4655
60.56 s	0.7704	1.1325	1.2389	1.1581	0.5155
101.5 s	0.7898	1.1613	1.2728	1.1724	0.5477
301.4 s	0.8164	1.0176	1.0347	1.1572	0.5857
851.9 s	0.8296	1.0057	1.0361	1.177	0.6055
1009 s	0.8373		1.0142	1.1836	0.6038
Average	0.7818	1.0367	1.0733	1.1668	0.5233
Std Dev	0.0532	0.0218	0.0426	0.0109	0.0957

a.

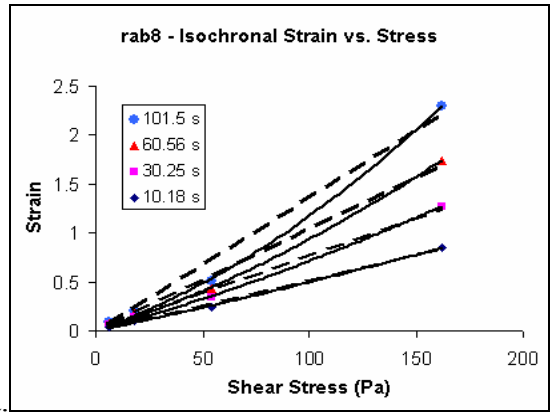

b.

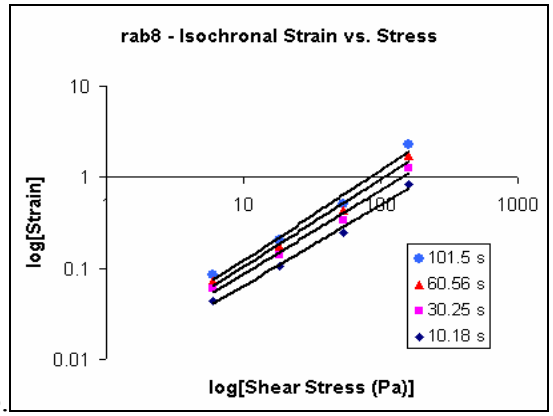

Figure 5.27 Isochronal data for *Rab 8* on (a) linear and (b) log-log axes of strain vs. stress.

a.

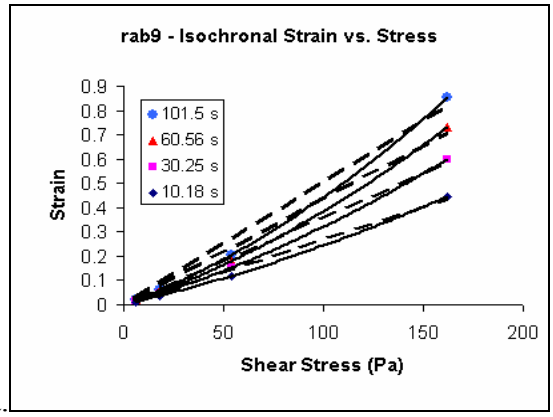

b.

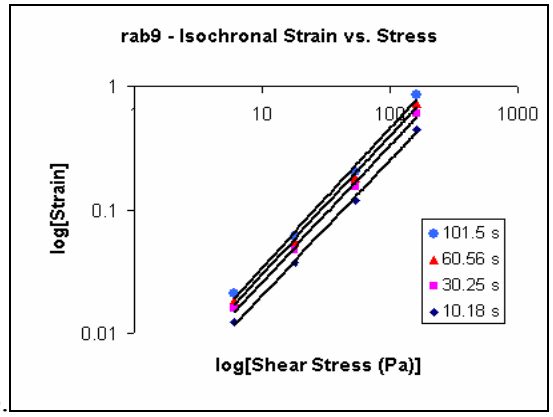

Figure 5.28 Isochronal data for *Rab 9* on (a) linear and (b) log-log axes of strain vs. stress.

a.

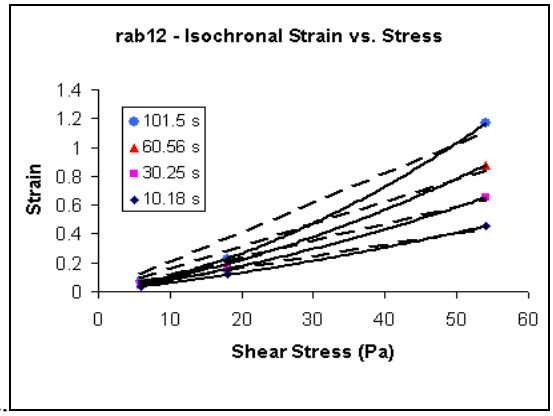

b.

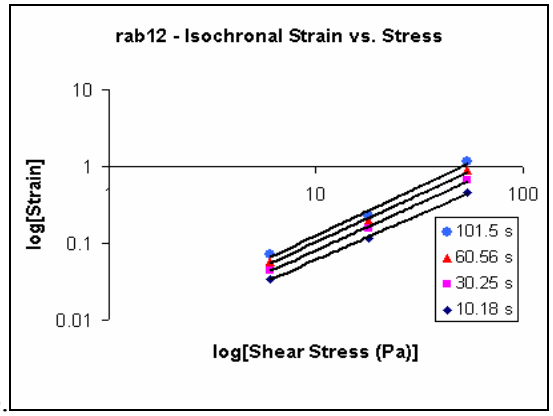

Figure 5.29 Isochronal data for *Rab 12* on (a) linear and (b) log-log axes of strain vs. stress.

a.

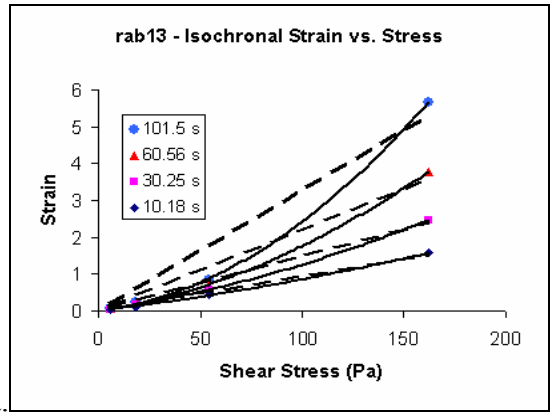

b.

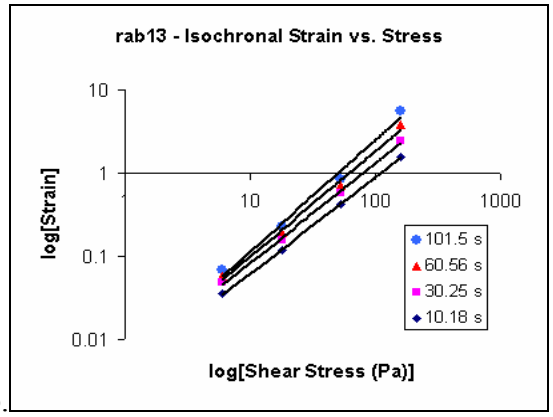

Figure 5.30 Isochronal data for *Rab 13* on (a) linear and (b) log-log axes of strain vs. stress.

a.

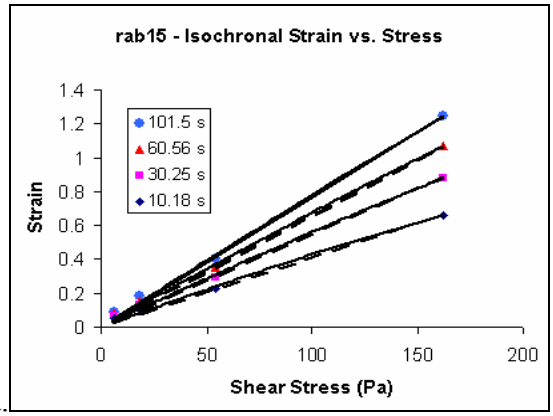

b.

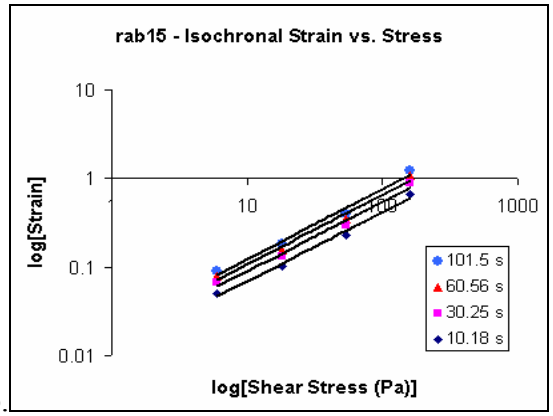

Figure 5.31 Isochronal data for *Rab 15* on (a) linear and (b) log-log axes of strain vs. stress.

5.2.8 Strain Prediction at Stresses of 18 Pa and 54 Pa

The attempt to predict strains using a QLV model was relatively successful. Model prediction parameters including values of the average stress power, m, and the coefficient of creep, A, are provided in Table 5.8. At an 18 Pa stress, the average R^2 value was 0.965 for the QLV model prediction and 0.919 for the linear viscoelastic model prediction. At stress of 54 Pa, the average

R^2 value was 0.983 for the QLV model prediction and 0.672 for the linear viscoelastic model prediction. Graphical results of the QLV model strain prediction compared to actual data and compared to the strains predicted by the linearly viscoelastic model are shown in Figures 5.32 through 5.36. Fit statistics are provided in Table 5.9 and Table 5.10.

Table 5.8 QLV model parameters for strain prediction at applied stresses of 18 Pa and 54 Pa.

Specimen Number	6Pa Slope, $\beta(\tau)$ ($x10^3$) [$Pa^{-1}.s^{-1/3}$]	Stress Power, m	Coefficient of Creep, A [$Pa^{-m}.s^{-1/3}$]	Andrade Const, J_A ($x10^3$) [Pa^{-1}]	Viscosity, η ($x10^{-6}$) [Pa.s]
1 (Rab 8)	2.499	0.7818	0.003695	1.900	0.2024
2 (Rab 9)	0.5360	1.0367	0.000502	0.8912	0.6527
3 (Rab 12)	2.315	1.0733	0.002030	0.1109	0.1173
4 (Rab 13)	2.015	1.1668	0.001494	1.354	0.1184
5 (Rab 15)	2.586	0.5233	0.006075	2.924	0.3973
Mean	1.9902	0.9164	0.002759	1.4360	0.2976
Std Dev	0.8418	0.2619	0.002185	1.0594	0.2290

a.

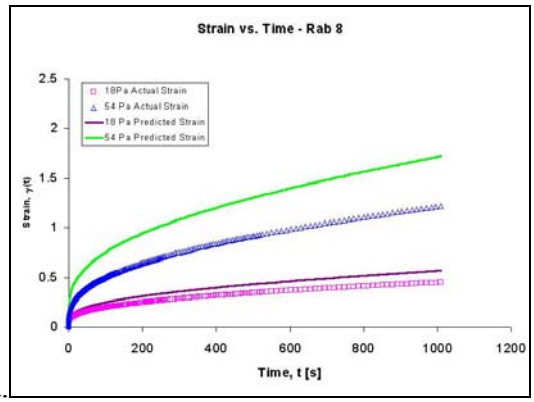

b.

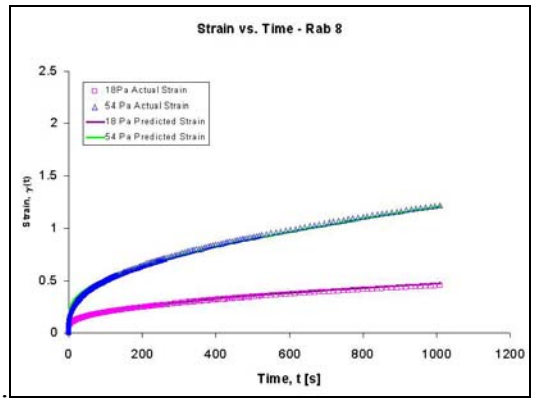

Figure 5.32 *Rab 8* - Strain vs. stress prediction for (a) linear viscoelastic and (b) QLV model.

a. 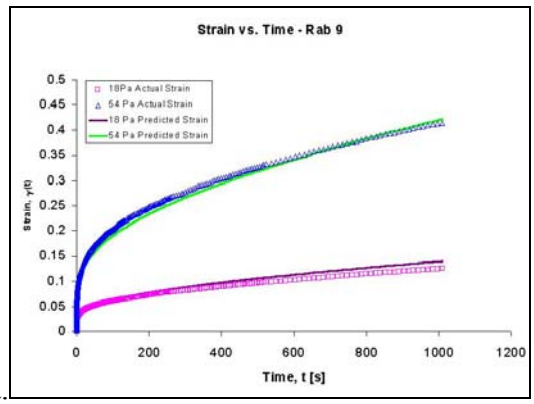

b. 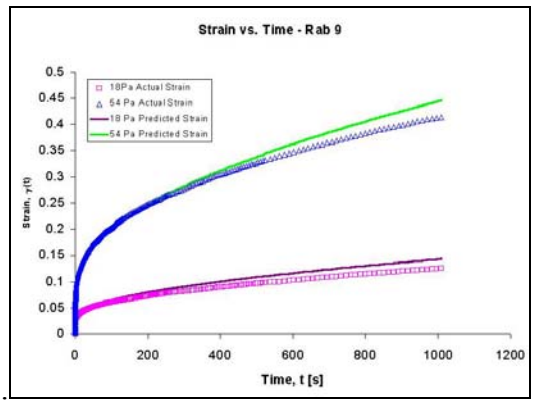

Figure 5.33 ***Rab 9*** **- Strain vs. stress prediction for (a) linear viscoelastic and (b) QLV model.**

a. 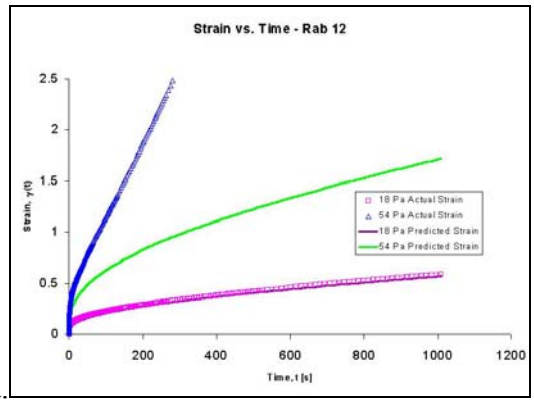

b. 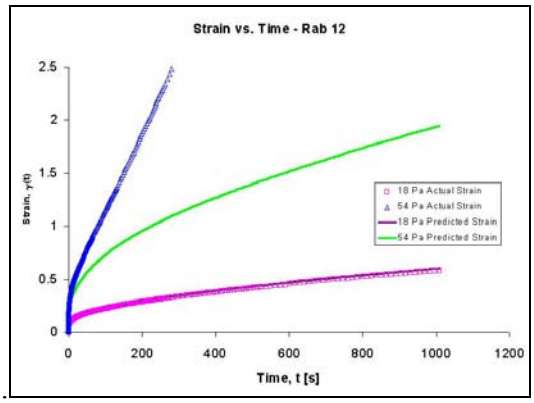

Figure 5.34 ***Rab 12*** **- Strain vs. stress prediction for (a) linear and (b) QLV model.**

a. 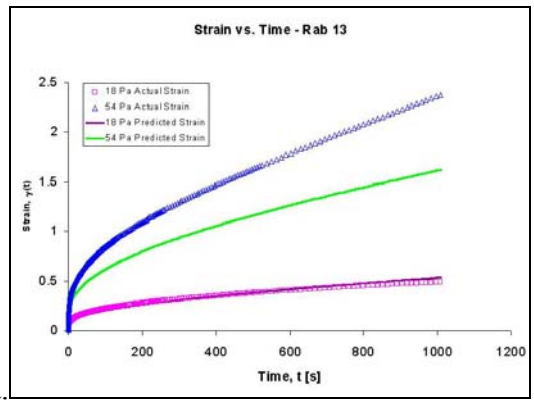

b. 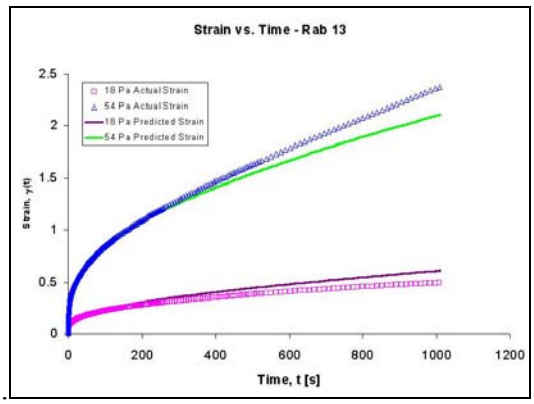

Figure 5.35 ***Rab 13*** **- Strain vs. stress prediction for (a) linear and (b) QLV model.**

a. 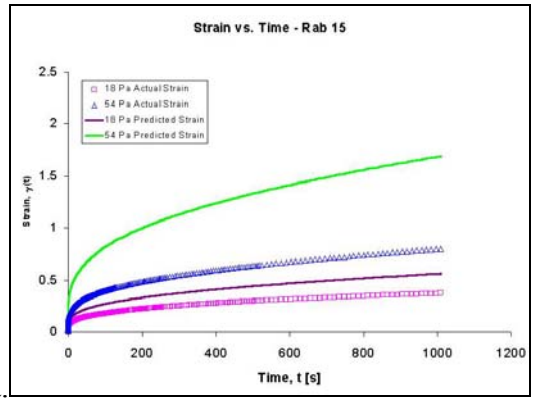

b. 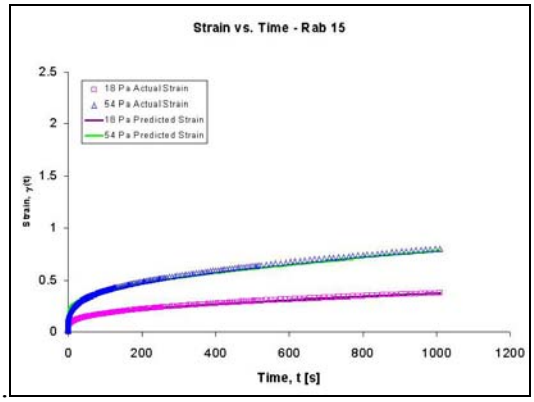

Figure 5.36 ***Rab 15*** **- Strain vs. stress prediction for (a) linear and (b) QLV model.**

Table 5.9 R^2 values for QLV model and linear viscoelastic model strain predictions.

Specimen	R^2 Value for Corresponding Stress and Model Type			
	18 Pa		54 Pa	
	QLV	Linear	QLV	Linear
Rab 8	0.9921	0.7460	0.9869	0.2810
Rab 9	0.9380	0.9662	0.9927	0.9902
Rab12	0.9905	0.9800	N/A	N/A
Rab13	0.9153	0.9846	0.9878	0.7445
Rab15	0.9871		0.9629	
Average	0.965	0.919	0.983	0.672
Std Dev	0.036	0.116	0.013	0.360

Table 5.10 SSE values for QLV model and linear viscoelastic model strain predictions.

Specimen	SSE Value for Corresponding Stress and Model Type			
	18 Pa		54 Pa	
	QLV	Linear	QLV	Linear
Rab 8	0.036	1.155	0.452	24.808
Rab 9	0.018	0.010	0.025	0.034
Rab12	0.070	0.148	N/A	N/A
Rab13	0.470	0.085	1.437	30.075
Rab15	0.038	3.345	0.489	72.663
Average	0.127	0.949	0.601	31.895
Std Dev	0.193	1.419	0.596	30.170

5.3 MINERAL OIL VALIDATION TESTING

5.3.1 Consecutive Creep Testing at 6 Pa (N = 10)

Upon analysis of the data from the 6 Pa consecutive creep tests, a general tendency for the specimen to decrease in compliance over an extended period of time was observed, as seen in Figure 5.37. Although variability was occasionally observed between consecutive creep steps where the compliance of a succeeding step would be greater than the compliance of the prior step, this occurrence was infrequent and appeared random (Figure 5.38). The overall creep behavior may be seen over an extensive number of steps as shown in Figure 5.39, where creep steps 1, 5, 10, 15, 20, and 25 are plotted on axes of compliance versus time. The reduction of compliance appears to approach an asymptote as the total experiment time increases (or with increasing creep steps), allegorical to an equilibration process or a decrease in driving potential. The recovery was also observed over a number of steps in order to determine whether this decrease in compliance was due to the accumulation of memory affects as dictated by the Boltzmann superposition principle. The overall recovery behavior over a number of steps is shown in Figure 5.40, where recovery steps 1, 5, 10, 15, 20, and 25 are plotted on axes of compliance versus time. The recovery compliance may be seen to decrease with increasing steps similar to the creep behavior. Recalling that the direction of recovery opposes the direction of creep, it is expected that the accumulation of memory with increasing creep steps would result in an increased recovery potential. This should be manifested as an increase in recovery compliance as the number of creep and recovery steps increase. However, an increase in recovery compliance is not observed in the data, thus suggesting that the decrease in creep compliance is due to some mechanism other than memory affects associated with the Boltzmann

superposition principle. Log-Log plots revealing similar trends from Figures 5.37-5.40 may be found in Section 5.4.2.

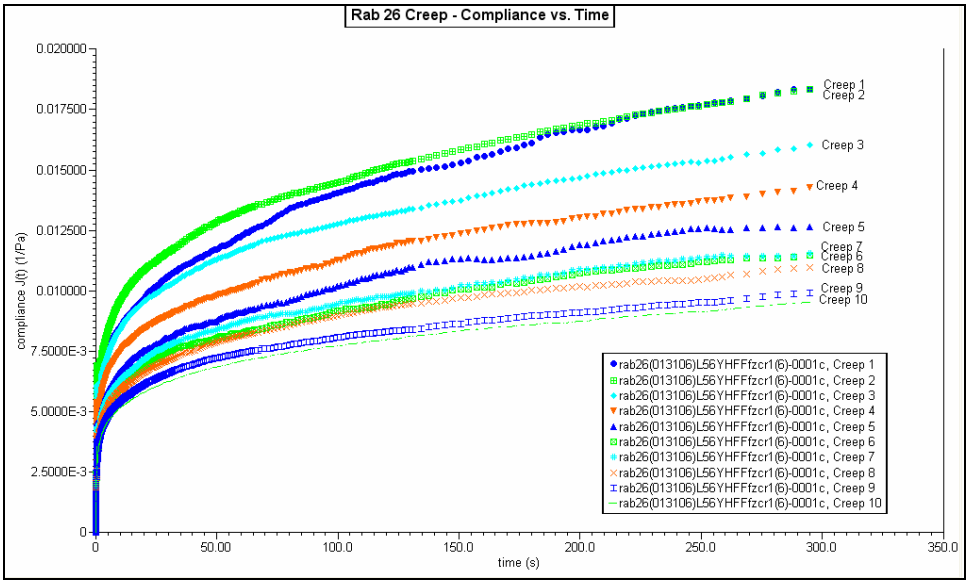

Figure 5.37 Data showing consistent decrease in compliance between consecutive steps.
Log-Log plots revealing similar trends from Figures 5.37-5.40 may be found in Section 5.4.2.

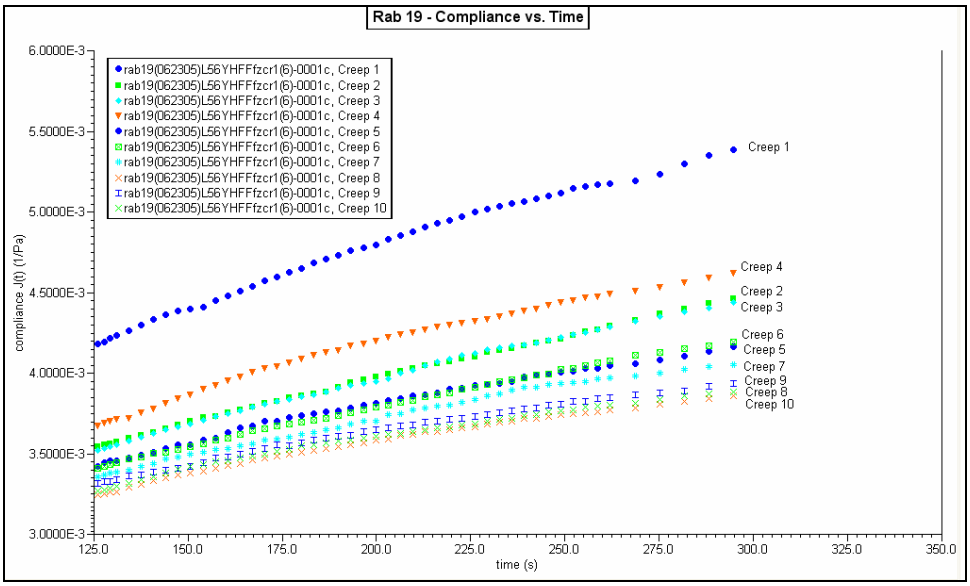

Figure 5.38 Data showing general trend of decreasing compliance despite variability.

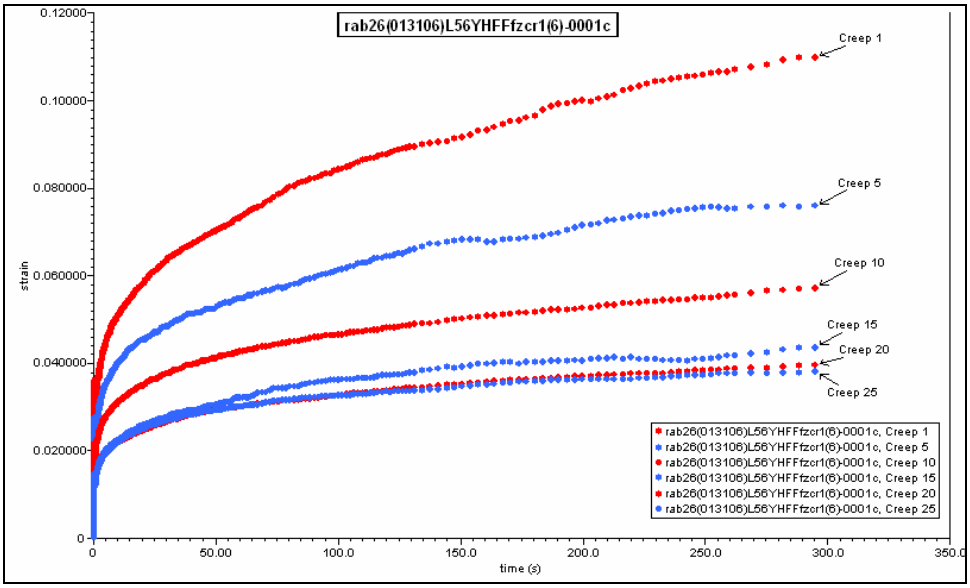

Figure 5.39 Data showing gross decrease in creep strain over extended number of steps.

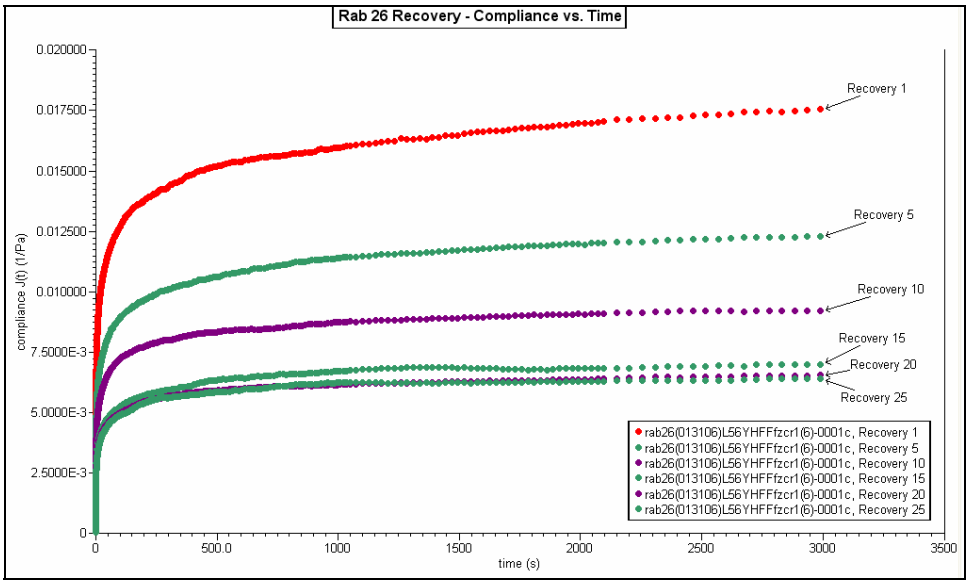

Figure 5.40 Data showing gross decrease in recovery strain over extended number of steps.

Results are provided in Table 5.11 for the percent error analysis, where the compliance change is provided for the first through the fourth creep step and the time prior to the start of the first creep step is also provided for each specimen. In Figure 5.41, the compliance change between the first and second creep step is plotted versus the time elapsed after installation and prior to the start of the first creep test. In general, this figure shows an approximate logarithmic relation between the initial creep change and the time elapsed prior to testing. In addition, the compliance change between the first and second creep step as well as the mean change over the first four steps was plotted versus the initial compliance of the first creep step at 300 s, as seen in Figure 5.42. This was performed to establish if the magnitude of the compliance change is related to the initial compliance level. However, no quantitative or qualitative relation was evident in the figure for either the change between the first and second creep steps or the mean change.

Table 5.11 Percent error in compliance between each of first four creep steps at 300 seconds.
In the table, the percent error between the final compliance value of the experiments creep 1 and creep 2 are provided. This highlights the immediate change in compliance that occurred within the specimens between subsequent steps. Percent errors from creep 2 to 3 and creep 3 to 4 also provide quantitative evidence of this. The mean and standard deviation of the percent errors provide general, qualitative evidence that a change in compliance is occurring over a number of creep steps. The compliance decrease tends to be largest from creep 1 to 2 and the overall compliance decrease tends to reduce as the "elapsed prior time" increases. Elapsed prior time is the total time elapsed following installation and prior to the start of the first creep step. ** Indicates the two specimens that had 8 hr, 50 min recoveries between subsequent creep steps.

Percent (%) Error in J(t) Between Each of First Four Creep Steps at 300 Seconds						
Specimen	Elapsed Prior Time (s)	Creep 1 & 2	Creep 2 & 3	Creep 3 & 4	Mean	Standard Deviation
rab17	116	58.23%	80.27%	13.59%	50.70%	33.97%
rab20**	680	26.42%	13.50%	-19.81%	6.70%	23.85%
rab18**	2315	7.94%	4.20%	2.82%	4.99%	2.65%
rab19	4725	17.08%	0.52%	-4.02%	4.53%	11.11%
rab22	4850	0.84%	0.68%	-6.32%	-1.60%	4.09%
rab24	8731	2.22%	0.66%	0.01%	0.97%	1.13%
rab26	14654	-0.40%	12.61%	11.04%	7.75%	7.10%
rab25	22519	-3.41%	0.31%	-0.04%	-1.05%	2.05%

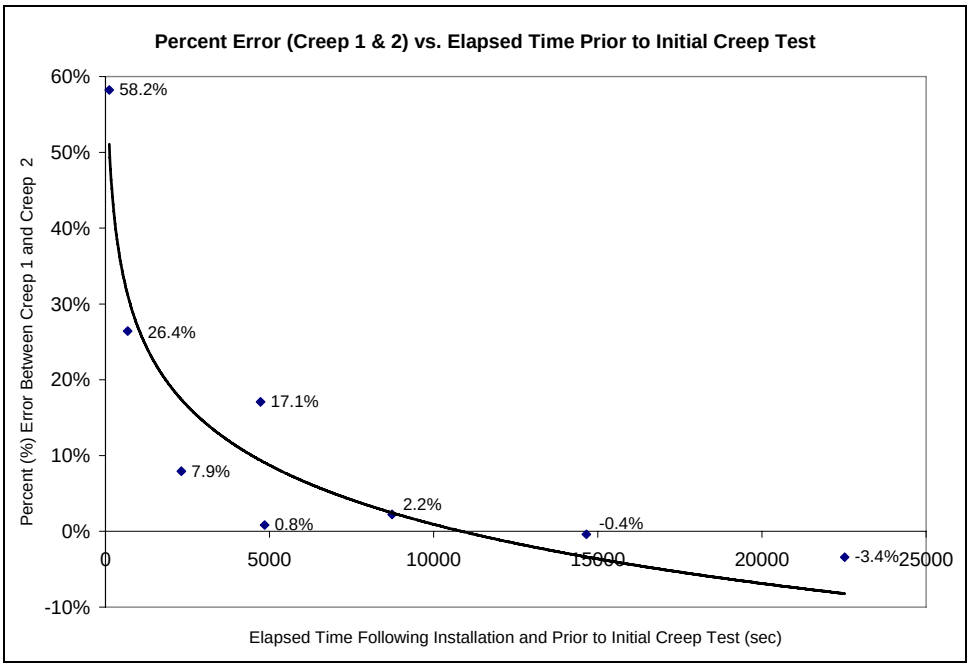

Figure 5.41 Percent error between first two creep steps versus time.
It appears that the decrease in creep compliance is reduced as the elapsed time increases following installation and prior to the first creep test.

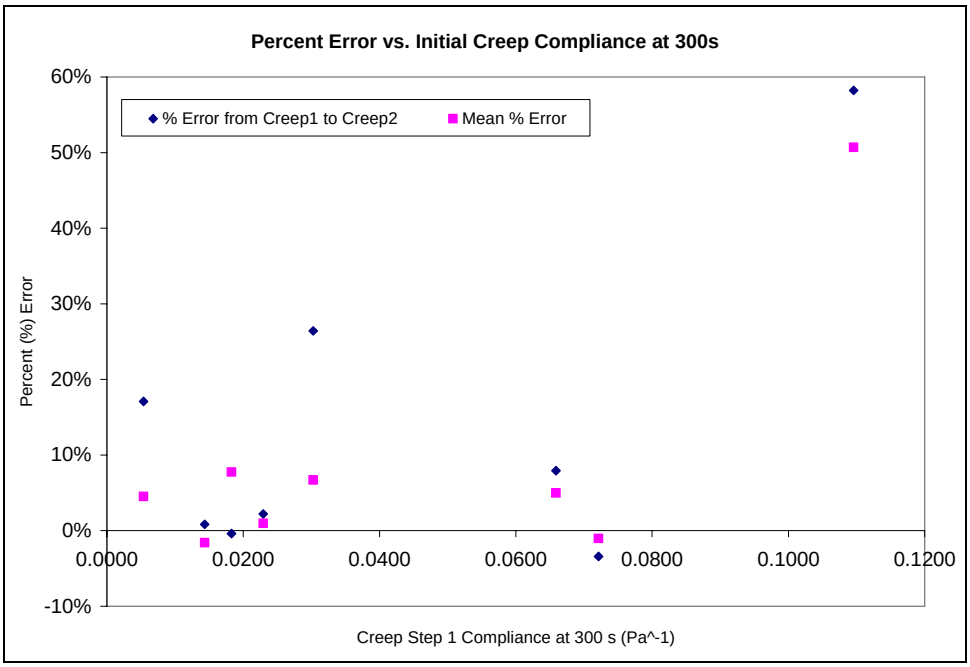

Figure 5.42 Percent error versus initial creep compliance.
The decrease in compliance is independent of the initial creep compliance level since no relationship may be seen for the percent error between first two creep steps (nor the mean percent error) versus the initial creep compliance.

5.3.2 Mineral Oil Dye Testing (N = 3)

Several observations were noted regarding the interaction of the NP with the mineral oil. Most notably, no evidence was found that indicates mineral oil is permeating into the NP. After an observation period lasting several weeks, no color change to the NP due to mineral oil penetration (dyed red) could be identified in any of the specimens. However, some evidence suggests that water may be slowly leaving the specimen. After a number of days, fine droplets surrounding the specimen were observed to appear in all specimens studied. The droplets at or near the NP interface were observed to increase significantly in quantity and become enlarged. At a magnification of 40x, rod-like entities were observed to appear in the mineral oil after two

weeks. The droplets are shown in Figure 5.43. The time-elapsed accumulation of droplets may be seen in Figure 5.44. The appearance of rod-like entities may be seen in Figure 5.45.

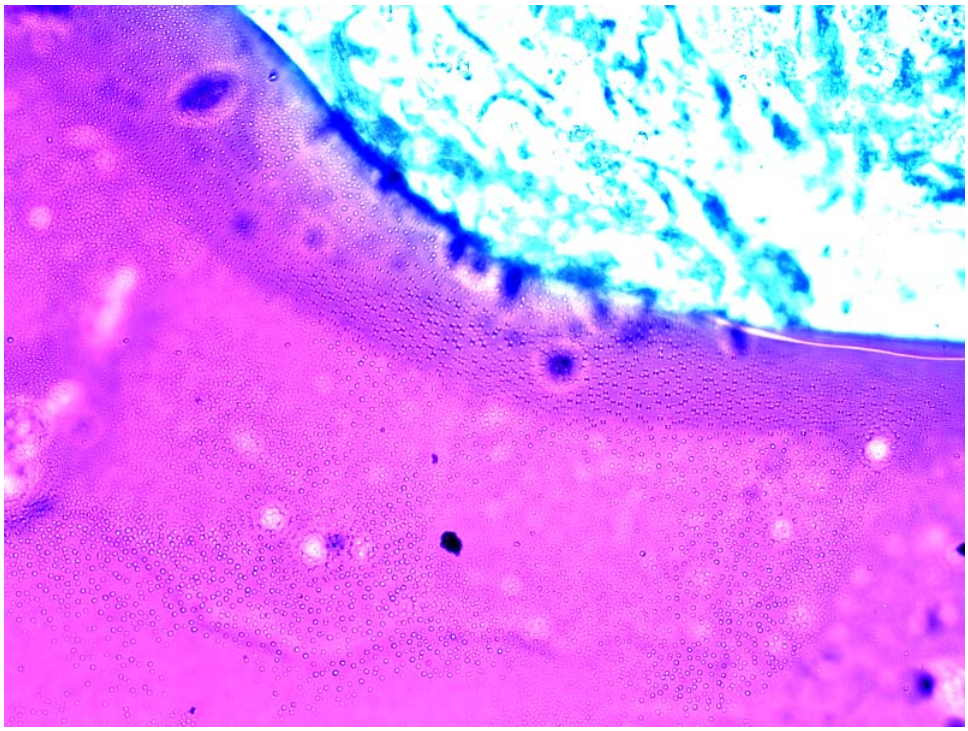

Figure 5.43 Photomicrograph (21x mag.) showing presence of droplets after three days.

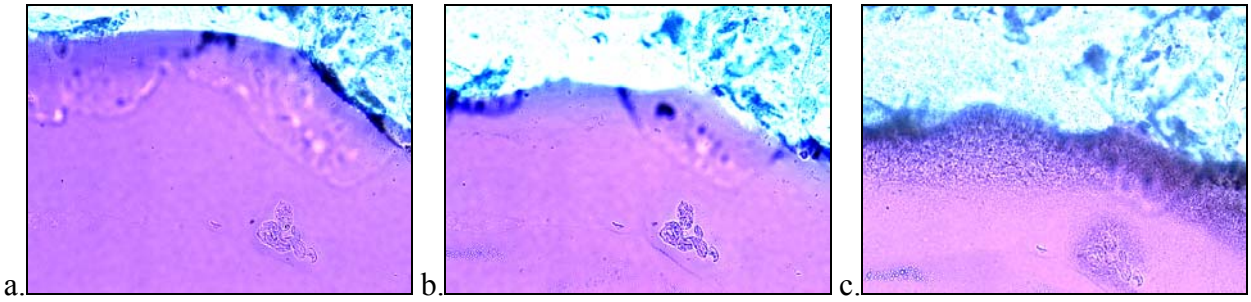

Figure 5.44 Photomicrographs (10x mag.) showing increase in droplet quantity with time.
Elapsed time after installation is increasing from left to right as follows: less than one hour (a), 3 days duration (b), and 14 days duration (c). The droplet quantity may be readily seen after 14 days duration.

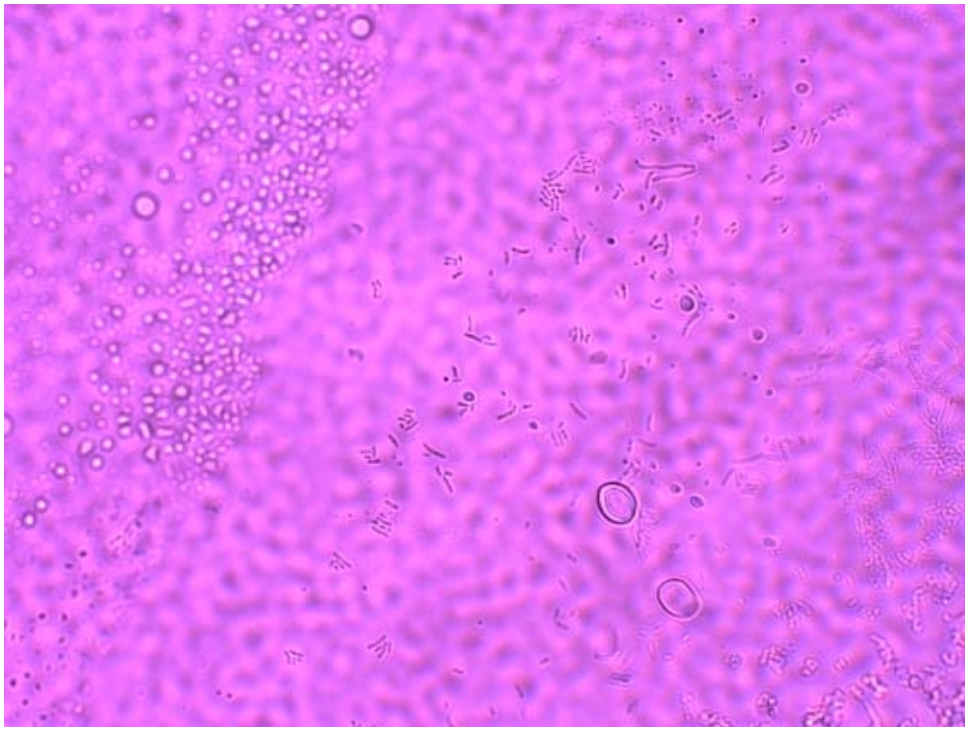

Figure 5.45 Photomicrograph (40x mag.) showing droplets and rod-like entities.
After two weeks, the presence of droplets was readily observable and the additional presence of rod-like entities was also noted. The identity of the rod-like entities and droplets are unknown. However, it is believed that the droplets are of water that has diffused out of the NP tissue. The rod-like entities may be related to this in some way.

5.4 HUMIDITY CHAMBER EXPERIMENTATION

5.4.1 Temperature Testing Heat Transfer Analysis Results

The analytical and numerical heat transfer analyses yielded similar results with calculated temperatures at the NP-to-cone interface of 37 ºC and 38 ºC, respectively. Figure 5.46 provides details of the FEA model including the solid model mesh and temperature distribution plot.

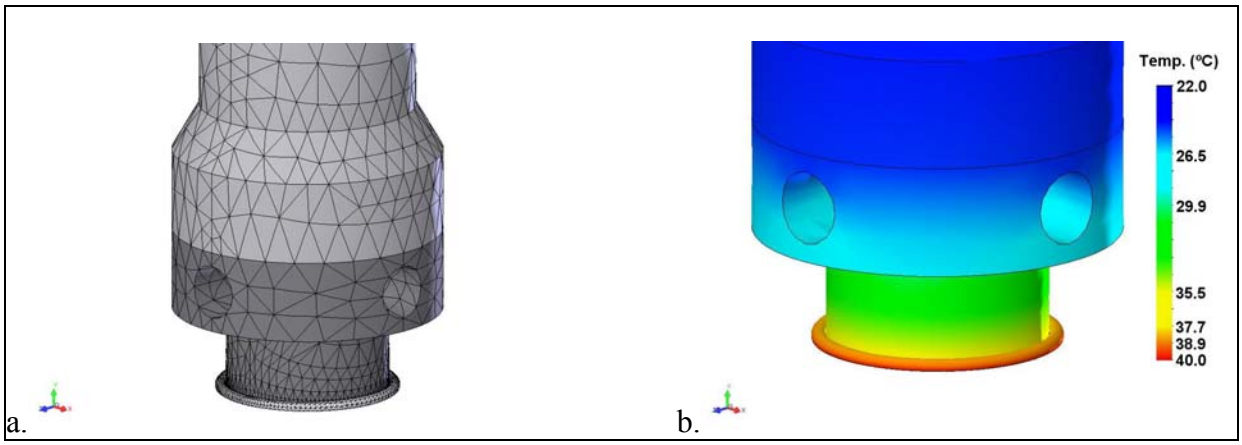

Figure 5.46 FEA model (a) mesh and (b) temperature distribution in specimen and cone.

5.4.2 Temperature Ramp Test Results

The temperature ramp testing revealed distinct temperature dependence within the viscoelastic behavior of the tissue. With each temperature increase of 5 ºC, the compliance shifted upward approximately 0.1 to 0.2 Pa^{-1} (Figure 5.47). Consistent with this observation, the ramp down temperature test produced a corresponding decrease in compliance (Figure 5.48). The combined ramp up, ramp down temperature test also resulted in an increase in compliance for each temperature increase and a decrease in compliance for each temperature decrease, although the compliance at each temperature on the downward ramp was slightly lower than the compliance at the same temperature during the upward ramp (Figure 5.49). It is speculated that this effect is due to dehydration, which is enhanced by the increase in temperature. Given the short duration of the creep steps within each test (60 seconds), behavioral traits associated with long-term temperature effects were unable to be delineated.

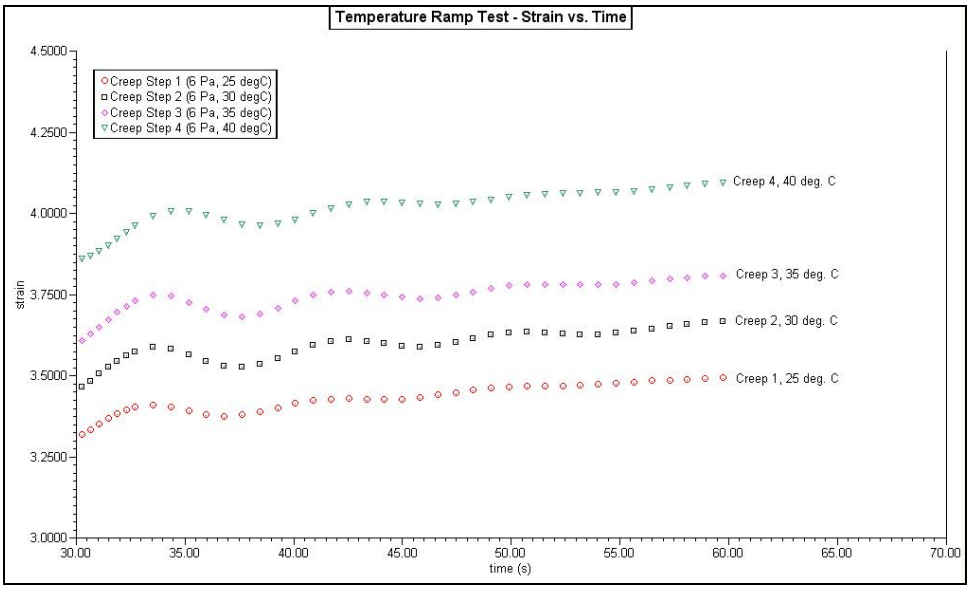

Figure 5.47 Results of the temperature ramp-up creep testing.

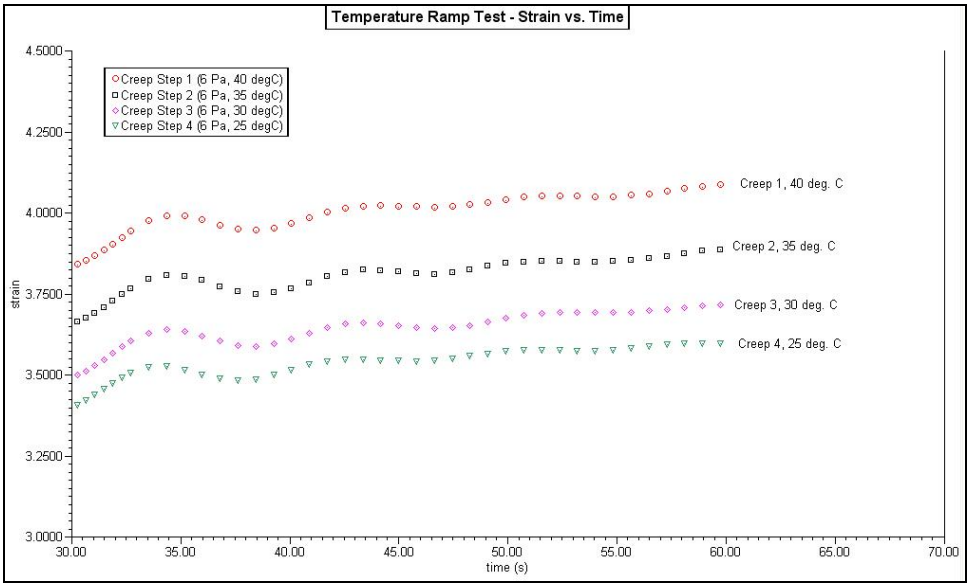

Figure 5.48 Results of the temperature ramp-down creep testing.

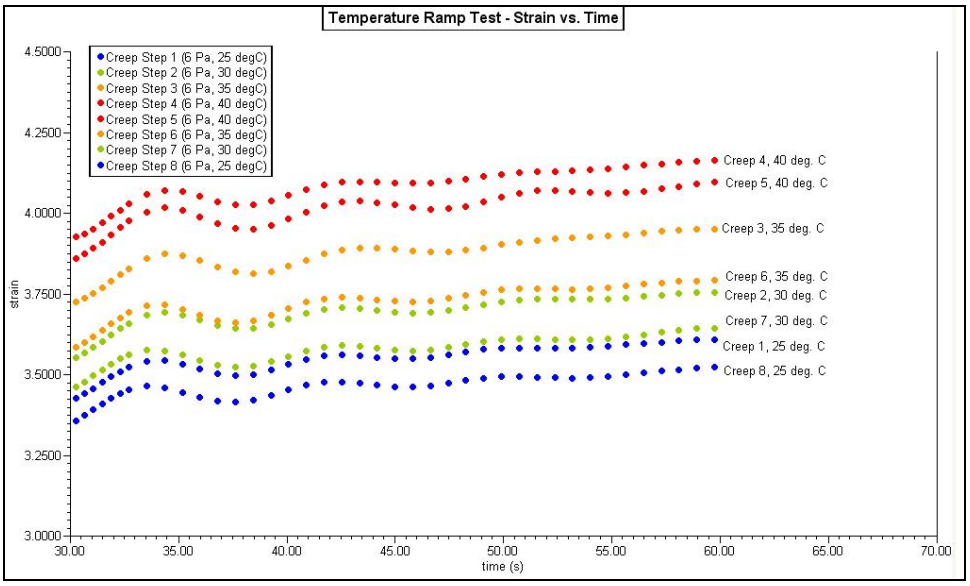

Figure 5.49 Results of the temperature ramp-up, ramp-down creep testing.

5.4.3 Specimen Creep Performance Using Mineral Oil Versus Humidity Chamber

In general, the use of mineral oil while conducting creep testing resulted in a decrease in strain level (and compliance) in subsequent creep steps at the same stress. This was further shown to be of some effect other than the accumulation of memory in the specimen due to insufficient recovery. The decreasing creep and recovery shown in Figure 5.50 and Figure 5.51, respectively, on log-log axes of strain versus time provide evidence of this. The inset view within each plot highlights the dominant strain decrease on linear axes. In addition, the strain of the 18 Pa creep test performed as creep step 46 was comparable in strain with the initial strain level achieved during 6 Pa creep testing, indicative of the substantial effect the compliance decrease has on data collected at larger stresses.

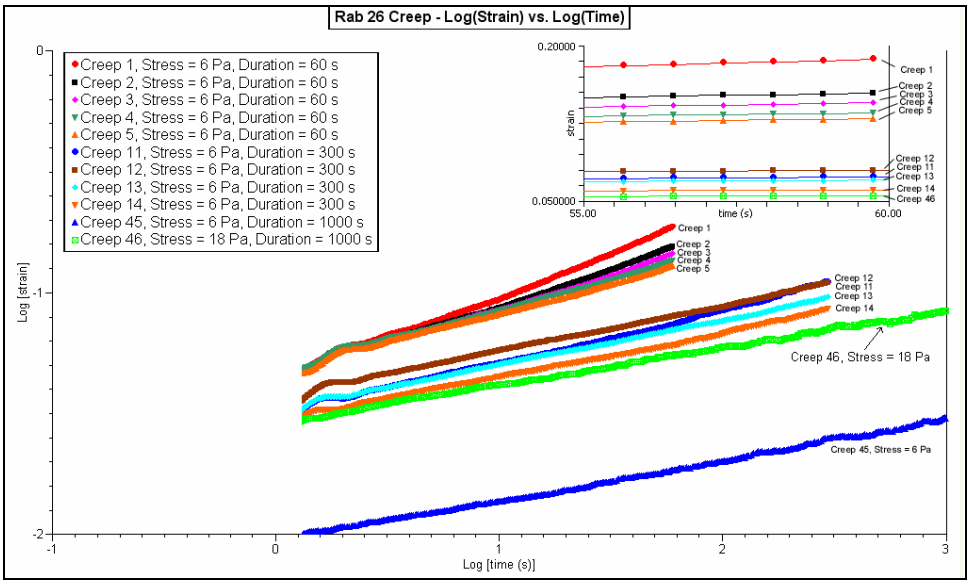

Figure 5.50 Representative creep data on axes of strain vs. time using mineral oil.
A decrease in strain level between subsequent creep steps at the same stress may be observed. The log-log axes indicate the noteworthy magnitude of the decrease. The inset view further highlights the strain decrease on linear axes. After 46 creep tests, the strain of the 18 Pa creep test is comparable in strain with the earlier 6 Pa creep tests. This emphasizes the substantial effect of the compliance decrease.

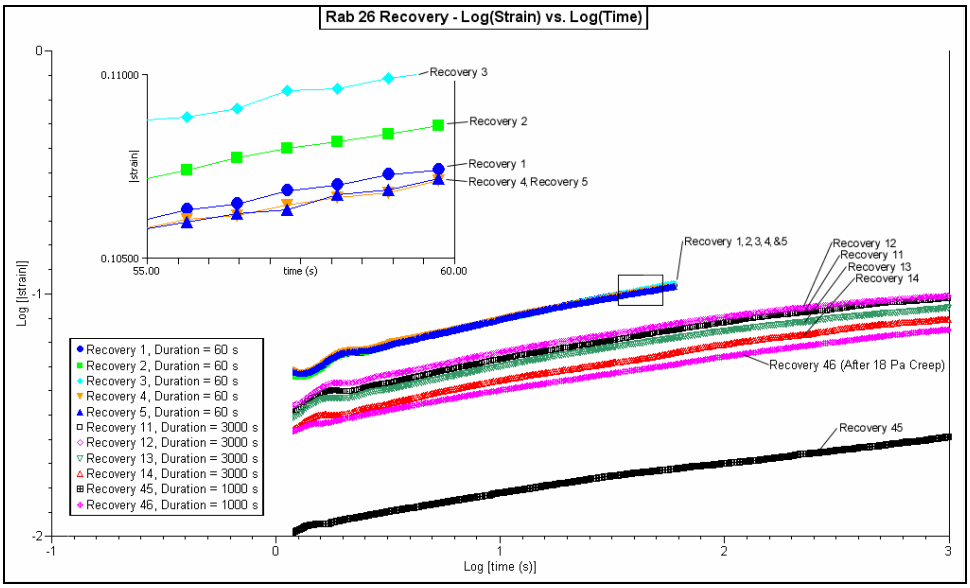

Figure 5.51 Representative recovery data on axes of strain vs. time using mineral oil.
A decrease in strain level between subsequent recovery steps may be observed. In particular, after 45 creep steps at 6 Pa stress, the recovery strain is well below the initial recovery strain level. Further, after the 46 creep step, which was performed at 18 Pa, the recovery strain is now nearly below the level of the initial 6 Pa creep recovery strains.

In contrast, the humidity chamber proved capable of producing both increased and decreased compliance in subsequent creep steps. In the instances where a decrease in compliance (or strain) was noted, the magnitude of decrease was of the same order or less than with the mineral oil. Further, an increasing level of recovery strain in subsequent steps was typically observed in conjunction with a decreasing compliance. This is suggestive of the accumulation of memory in the specimen from repeated loading and insufficient recovery rather than dehydration or some other mechanism. These observations are revealed for creep in Figure 5.52 and for recovery in Figure 5.53. In addition, the strain of the 18 Pa creep test performed as creep step 24 was about 0.5 logarithmic units larger than the initial strain level achieved during 6 Pa creep testing, indicating that the original level of compliance remained relatively constant over the elapsed time. Nonetheless, it is necessary to note that the results obtained while using the humidity chamber are preliminary and further validation is required.

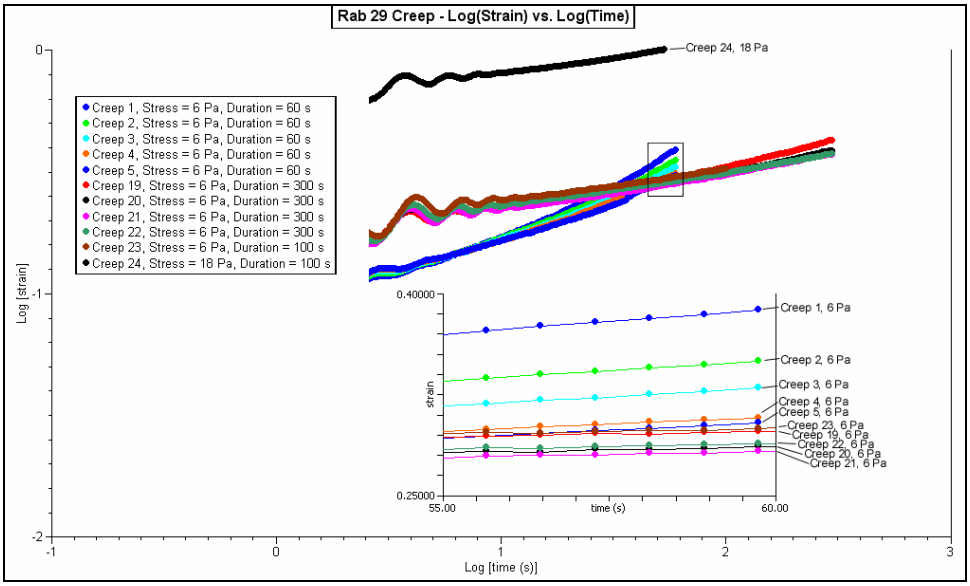

Figure 5.52 Representative creep data on strain vs. time axes using humidity chamber.
In the figure, low magnitude differences in creep strain are observable between subsequent steps. The inset reveals the slight trend of consistently decreasing creep strain with each consecutive step. However, after 24 creep steps, the strain level of the 18 Pa test is still about 0.5 logarithmic units greater that the 6 Pa tests.

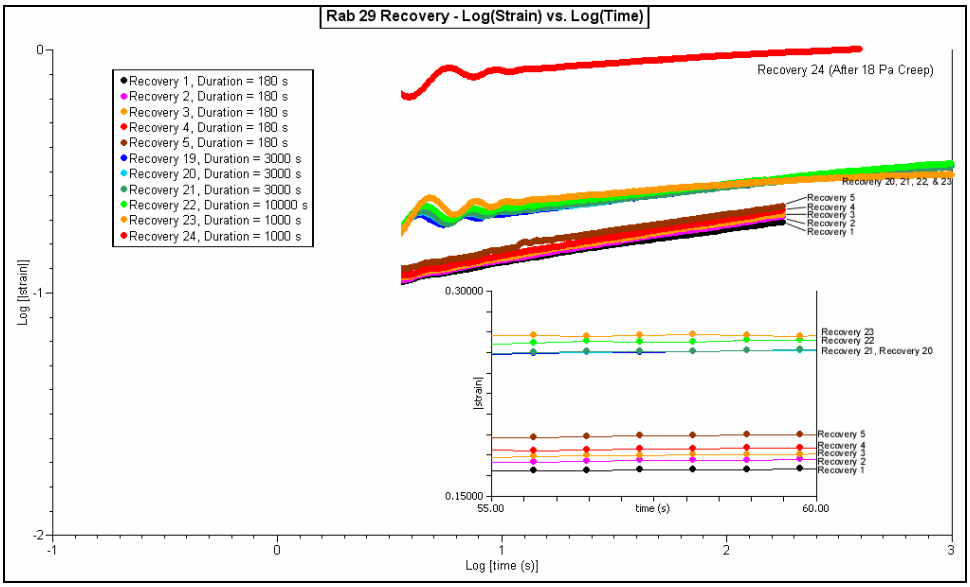

Figure 5.53 Representative recovery data on strain vs. time axes using humidity chamber.
In the figure, modest differences in recovery strain are observable between subsequent steps. The log-log axes indicate the low magnitude of these changes. The inset reveals the trend of consistently increasing recovery strain with each consecutive step. These slight increases may be due to the accumulation of memory in the specimen from repeated loading and insufficient recovery.

6.0 DISCUSSION

6.1 VARIABLE STRESS TESTING DATA SET

The general results obtained from the variable stress testing data set are summarized in the following statements. The 2 Pa stress was determined to be too insubstantial to use when testing the tissue since recovery potential remaining from installation strains seemed to override the applied torque, causing the specimen to creep in the opposite direction. The material tended to display mildly nonlinear viscoelastic behavior, evidenced by unique creep curves on linear axes of compliance versus time. The slope and corresponding creep rates appear to be the same for each of the applied stresses on log-log axes of strain versus time, indicating that the nonlinearity may be stress dependent and separable from the time-dependent behavior. At large strains and at long times, the material displayed yielding, a specific manifestation of strong nonlinear behavior indicative of breakdown or structural damage within the specimen.

It is believed that the considerable (and immeasurable) deformation performed on the specimen during installation was producing a significant installation memory and fostering an eagerness within the tissue to recover despite the applied 2 Pa stress. Thus, the 2 Pa stress was determined to be inadequate in overcoming these installation memory effects. This behavior, embodied by creep reversal, is erroneous and is not a measure of the true material properties of the specimen regardless of the applied stress that it is observed to occur. In cases where creep reversal was not observed, it was believed that the installation memory effects could still be

present but favoring the direction of the applied torque, thus intensifying the 2 Pa creep. This has been supported by the observation of markedly enhanced 2 Pa creep deformation occurring in some specimens. As a result, this testing issue led to the inclusion of a pre-test recovery step in subsequent procedure sets, intended to allow the specimen to recover out any memory effects incurred during extraction, installation into the rheometer, and fixturing beneath the cone and plate. Essentially, it was determined that the average ending creep strain rate at 6 Pa was approximately 0.0002 s^{-1}. Based on the lab rule that the recovery is sufficient when the recovery rate is 100 times less than the ending creep rate, the specimen should have a pretest recovery strain rate of about $2x10^{-6}$ s^{-1} prior to beginning creep testing. Through the exclusion of the 2 Pa creep test, implementation of the pretest recovery step, and allowing for extended recovery times of several multiples longer than the creep duration, effects of the creep reversal commonly associated with the 2 Pa creep stress appear to have been eliminated. This reinforces the argument that the observed behavior resulted from installation memory effects and indicates the consequences that residual memory may have on data obtained during subsequent testing. Furthermore, this emphasizes the need for vigilance during testing to ensure the specimen is sufficiently recovered prior to collecting additional data.

To determine whether the nonlinear viscoelastic behavior displayed by the specimen could be described by quasi-linear viscoelasticity (QLV), creep rates were analyzed for equality between different stresses on log-log axes of strain versus time. There was limited evidence suggesting that the general creep behavior of the specimen was of a more general form than QLV. For the lower stresses (6, 18, and 54 Pa), which were less inclined to produce yielding at short times, the data was statistically insignificant ($p >> 0.05$) and the null hypothesis was accepted. In other words, the data was insufficient to suggest that the creep rates differed and a

more general nonlinear model other than QLV is appropriate in describing the NP creep behavior. Therefore, the log-log slopes appear to be constant at low strains and times regardless of the applied stress. These findings are in agreement with the findings of Iatridis, who determined the nonlinear viscoelastic behavior of human nucleus pulposus tissue to obey QLV.[4,95] This may also be seen by the lines of data in Figure 6.1, depicting creep strain versus time on log-log axes, where the log-log slope is approximately the same for each of the stresses. For the 162 Pa stress application, the statistical significance was $p = 0.053$, rejecting the null hypothesis and accepting the alternate hypothesis. Recalling that the confidence is the difference between unity and the significance $(1 - p)$, the confidence level is approximately 95% (actually, it is 94.7%). Thus, at about 95% confidence, the data statistically proves that a more general theory than QLV is required to describe the 162 Pa creep behavior of the NP tissue. However, it may be seen that the 162 Pa data is only narrowly significant (i.e., the data is significant only by rounding off the last decimal). In this respect, the QLV theory is likely to be capable of describing the 162 Pa creep behavior in many cases but time-dependent nonlinear effects are prevalent at this stress and should be accounted for with an appropriate model. Further, the visibly nonlinear behavior at 162 Pa was manifested as yielding, which increased the standard deviation of the mean creep rate at this stress and may have contributed to rejection of the null hypothesis. The material may or may not be QLV at 162 Pa since no truly convincing conclusions could be drawn. Thus, reduced variability in the data is needed in order for more concrete statements to be made regarding the nonlinearity of the tissue.

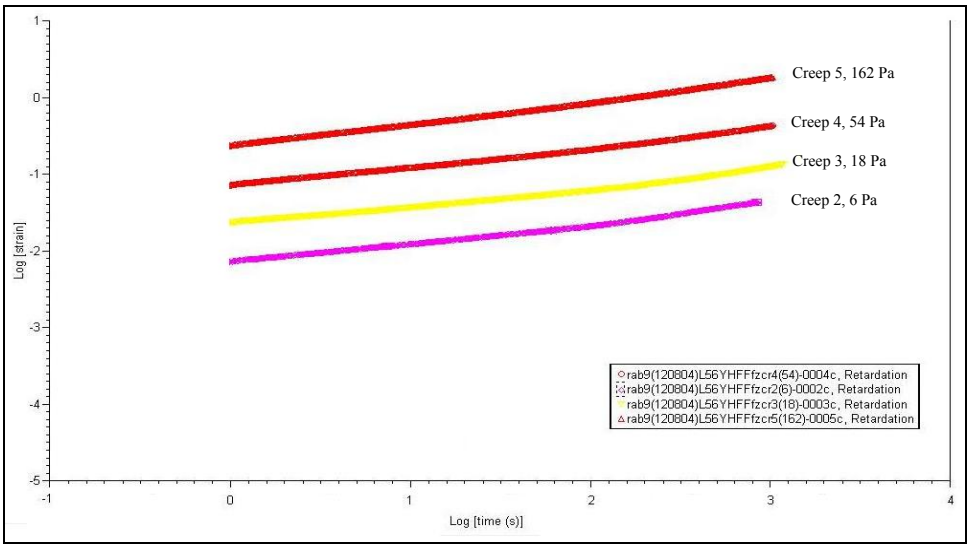

Figure 6.1 Log-log strain vs. time plot. Log-log slope is approx. equal for all stresses.

The analysis to determine the critical strain used positive acceleration of the creep curve on linear axes of compliance versus time and the presence of a relative minimum on linear axes of creep velocity versus time to locate the time and strain that the onset of yielding occurred. Statistical analysis determined the mean critical strain to be within the range of 1.91 to 3.67 at 95% confidence for specimens tested using the methods of the current study. This should be interpreted as follows: using the exact methods employed in this analysis, the average critical strain of a sample of N specimens will be somewhere within the range of 1.91 to 3.67 for 95% of the samples collected. In proximity to this range, the tissue reaches a strain where it begins to incur damage or begin experiencing structural breakdown to some extent.[77,78] While it is also possible to determine the presence of yielding by a slope of unity on log-log axes of compliance versus time, this criterion actually indicates the presence of steady-state flow[69] and is, therefore, a sufficient *but* unnecessary condition for the presence of yielding. Rather, positive acceleration of the creep compliance when plotted against time on linear axes is a sufficient *and* necessary

condition, providing a more comprehensive indicator of yielding behavior. The specific time location where the plot changes concavity (inflection point) and begins accelerating positively is made clear by a relative minimum of the creep velocity against time. The strain obtained at the time of this inflection is the critical strain for that specimen.

It is reasonable to speculate that the factors leading to the onset of yielding within the specimen are somewhat dependent on the condition or state of the material composing the specimen. The molecular weight and aggregating ability of the proteoglycans, the integrity and number of collagen cross-links, or the hydration level of the specimen are all affected by the IDD and some or all of these features may contribute to altered values of the critical strain. Therefore, from this procedure, it is possible that the critical strain may be determined for degenerated and treated NP tissue and these values may be compared against healthy tissue as an outcome measure for the success of IDD treatments. Further, discovering specific compositional factors that affect critical strain may lead to greater resolution in distinguishing the ability of one treatment over another in achieving specific compositional and biomechanical objectives.

6.2 MODELING ANALYSIS

The modeling analysis was performed on a select group of specimens within the variable stress testing data set. The general results obtained from the analysis are summarized in the following statements. Computer assisted curve fitting of both the Andrade and Nutting creep compliance models resulted in a strong fit to the data with tight confidence intervals and low residual error. Extrapolation of data using fits obtained over the first 300 seconds of data indicate that the Andrade creep model is more suitable than the Nutting creep model as well as both the logarithmic and exponential creep models. The prediction of the recovery strain was not

sufficient to suggest that the material adheres to the Boltzmann superposition principle, which implies that the material is nonlinearly viscoelastic. Lines of isochronal data on linear and log-log axes of strain versus time confirm that the inherent nonlinearity of the tissue is separable from the time dependence, supporting the belief that the tissue obeys QLV theory. Based on prediction of strains at higher stresses, the modified QLV Andrade model generally provides a more suitable constitutive model for describing the tissue behavior than the linear viscoelastic Andrade model.

The compliance formulation of the Andrade and Nutting models, equations 2.15 and 4.5 respectively, produced strong fits over the entire range of data. The mean R^2 value of the Andrade model fit for the five specimens was 0.9996, suggesting a strong fit for each of the specimens. Attention should also be placed on the mean Sum of Squared Error (SSE) value of 3.849×10^{-6}. The SSE is the error measure that is minimized during least squares regression fitting, having bounds from zero to positive infinity. A value closer to zero represents a good fit. Since the SSE does not exceed 10^{-5} for any of the specimens analyzed, a good fit is indicated by this parameter as well. However, complete analysis of the goodness of fit requires that the specific values of the parameters be analyzed in addition to the fit statistics. Restated, a particular model may have strong fit statistics but still be a poor model if the parameters it determined are physically meaningless. With this in mind, the values of J_A are realistic since they are all positive, bounded values. The same was also true for the slope term, β. The values of viscosity, η, were all positive with magnitudes on the order of 10^6 Pa.s, indicating a high viscosity. This is expected given the mucous-like nature of the tissue. The Nutting model fit statistics indicate a strong fit with a mean R^2 value of 0.9996 and a mean SSE of 3.44×10^{-6}. Analysis of the actual parameter values suggests the models are also realistic with positive,

bounded values of β, J_A, and viscosity, η. In addition, the Nutting power, n, for each specimen falls between 0 – 1 with a mean value of 0.398, as was anticipated in order to achieve a good fit. Therefore, the Andrade and Nutting models fit the entire data range very well, in general.

The goodness of fit was compared for both the Andrade and Nutting models. The R^2 values for the Nutting model were consistently improved over the Andrade R^2 values, but varied by less than 0.01% so limited goodness of fit information may be obtained from this statistic. Comparison of the SSE values provided greater resolution between the models, where the Nutting model resulted in a 15% improvement in SSE on average. The 95% confidence intervals of both the Nutting and Andrade model were within 1.5% of actual data, with the Nutting model showing a slight improvement of approximately 0.1%. Thus, the error associated with the Nutting model was reduced over the Andrade model, although this error improvement was small.

More noticeable deviation was noted between the models upon comparing the individual model parameters, with the mean β and J_A values differing by over 37% and the mean viscosity between each of the models differing by 54%. The Nutting power, n, typically results in a different power law than that of Andrade and is expected to have different β and J_A parameter values than the Andrade values of J_A. However, the difference in determined viscosity between models leads one to question which model produces a more appropriate viscosity value. Further, since the model fits provided here were obtained over the entire data range with the objective of minimizing overall error, one should expect that any reasonable model selection would produce a relatively good fit. Accordingly, further analysis was required to distinguish with more certainty which model provided a better fit.

Extrapolation of data from 300 to 1000 s using model parameters fit over the first 300 seconds of data aided in determining which model was most successful in describing the

viscoelastic behavior of the tissue. Two additional common creep models, logarithmic and exponential creep, were included for comparison. These models were only fit to two of the specimens since it was immediately obvious that a suitable fit could not be obtained using them. The logarithmic model from equation 4.6, $J(t) = J_0 + B\log(t) + t/\eta$, appeared to fit the data well over the first 300 s of data but produced a constant rate of creep (straight line) immediately upon entering the extrapolation region, which was uncharacteristic of the actual data. The exponential model from equation 4.7, $J(t) = J_0 + C(1 - e^{-dt}) + t/\eta$, was unable to predict the data well while still within the parameter fitting region since it accelerated positively from the start at zero time. In this respect, equation 4.7 may produce a more suitable model for describing yielding behavior. The comparison between the Andrade creep model and the Nutting creep model were performed on all five specimens selected for modeling. In all five instances, the Andrade creep model provided a better extrapolation of the data than the Nutting model. For three of the five specimens, the improvement in predicting data of the Andrade model over the Nutting model was substantial (Figure 5.17, Figure 5.18, and Figure 5.19). In only one instance did the Andrade model deviate a noteworthy amount at or near 1000 s, while still only deviating by about half the amount of the Nutting model (Figure 5.20). Therefore, although the Nutting model is capable of providing a better fit for the entire data range because it has increased freedom to minimize error (by alteration of the power, n), it is considerably less effective in extrapolating data or predicting beyond the fitting range. In this context, the Andrade model provides the most suitable fit of all the models compared via the extrapolation analysis.

An attempt was made to predict the recovery strain of each specimen from the creep portion of the data using the Boltzmann superposition principle. The prediction resulted in an average R^2 value of 0.8484, with a maximum $R^2 > 0.98$ and a minimum $R^2 < 0.55$. Although the

prediction fit was fair to good, with a strong fit for one specimen (Rab 8, $R^2 > 0.98$), it was evident that the overall prediction was insufficient to suggest that the tissue obeyed the Boltzmann superposition principle.[78] This indicates that the nonlinear behavior of the material may not be approximated as linearly viscoelastic. Rather, some other theory is required to describe the nonlinear viscoelastic behavior such as the QLV theory, which has been pointed to as a possible descriptor by the QLV statistical analysis discussed in section 6.1 and supports the findings of Iatridis.[4,95] However, from this analysis, it is still plausible that a more general nonlinear theory is required such as the nonlinear (modified) superposition principle or Shapery's nonlinear creep theory.[66,73]

Lines of isochronal data plotted on linear axes of strain versus stress provide an additional indicator that the tissue is nonlinearly viscoelastic. The average adjusted-R^2 values for the linear and second-order polynomial were 0.9931 and 0.9979, respectively. The quadratic fit consistently provided a greater adjusted-R^2 value with the exception of one specimen. Recall that the adjusted-R^2 adjusts for the number of terms in the model since the standard R^2 always increases as the number of model terms increase. Despite the adjustment, higher order terms were present in the lines fit to the isochronal data points on linear axes. It should be noted that, in most cases, it was visually obvious that the lines of isochronal data on linear axes were curved rather than straight. On log-log axes, the slopes of the isochronal data terms were approximately constant and the lines were straight. This suggests that nonlinearity of the tissue is independent of time. In other words, the nonlinearity of the material is dependent on the stress only and the time dependence of the strain of the tissue may be separated from the stress, again implying QLV.[81] The creep strain of the tissue may then be based on equation 4.13, $\gamma_c = K(t)\tau^m$.[93,94] Recall that K(t) is the separable time dependent component of the strain, τ is the stress, and m is

the stress power determined by the slope of the isochronal data lines on log-log axes of strain versus stress.

Using the average stress power, m, determined for each specimen via log-log lines of isochronal data, the creep strain of the tissue was predicted at 18 Pa and 54 Pa. The prediction was performed using the constitutive relation in equation 4.24,

$$\gamma(t) = J_A\tau + A\tau^m t^{1/3} + \tau\frac{t}{\eta},$$

where J_A, A, and η were determined by fitting the modified QLV Andrade creep model to the data at 6 Pa. This was compared with the linear viscoelastic formulation of the Andrade creep model. The creep strain predicted using QLV based model generally produced a strong fit to the data with average R^2 values of 0.965 and 0.983 at 18 Pa and 54 Pa, respectively. The linear viscoelasticity based model produced a moderate fit to the data with average R^2 values of 0.919 and 0.672 at 18 Pa and 54 Pa, respectively. The linear viscoelastic formulation produced a strong fit to the 18 Pa data for two of the specimens but modeling of the 54 Pa strain data was poor and resulted in substantial modeling error. In addition, the R^2 values for the 18 Pa and 54 Pa fits provided by the linear viscoelastic formulation of one specimen was effectively zero and could not be calculated. In contrast, the QLV formulation consistently provided a strong fit to the data with low residual error. In this respect, the QLV formulation of the Andrade creep model provided by equation 4.24 is a suitable constitutive model for describing the viscoelastic behavior of the tissue. However, more testing and data analysis is necessary to establish the model provided in equation 4.24 as an appropriate model for describing the tissue creep behavior.

Similar to the average critical strain value, it is reasonable to assume that the parameters of the constitutive model, J_A, m, A, and η, are dependent on the condition of the specimen.

Further, it is expected that the molecular weight of the proteoglycans, quantity of collagen cross-links, and the hydration level of the specimen will contribute to specific changes in the parameter values. In fact, the parameters of the Andrade equation, J_A and β, have been shown to decrease monotonically with increasing molecular weight for a given applied stress in various stocks of polydimethyl siloxane.[84] Similar results may be obtained in the NP tissue and further investigation in this area is suggested. Therefore, application of the Andrade model and the QLV constitutive model to degenerated rabbit NP tissue is expected to result in altered parameters – thus providing quantifiable, functional benchmarks of success for molecular therapy approaches to the treatment of IDD.

6.3 MINERAL OIL VALIDATION TESTING

The general results obtained from the mineral oil validation testing are summarized as follows. The consecutive creep testing revealed a consistent decrease in compliance with the use of mineral oil that appears to be independent of memory effects and the number of tests performed. The compliance change associated with this overall decrease appears to become reduced as time elapses following installation. The mineral oil dye testing revealed that the mineral oil does not permeate into the specimen. However, within one day, possible water droplets are observed to accumulate in the mineral oil around the periphery of the specimen. Thus, it is speculated that the decrease in compliance with time and the observed droplets are due to a dehydration mechanism in the tissue, where water is permeating out of the specimen and into the mineral oil.

During the consecutive creep testing, the creep compliance consistently decreased following each creep step. The recovery also decreased consistently rather than increasing with the increasing number of creep steps. Therefore, memory effects accumulated during testing are

not likely to be the dominant source of the decrease in compliance. A positive correlation was observed between the elapsed time prior to the start of creep testing and the amount of compliance decrease following the first creep test. The decrease in compliance became less as the time following installation and prior to the first creep test became greater. This may suggest that the decrease in compliance is due to memory effects associated with the installation of the specimen. However, correlation does not necessarily indicate causation. A more general, time-dependent mechanism may be producing the decrease in compliance. Two of the specimens were tested with 8 hour, 50 minute recovery durations instead of a 50 minute recovery. However, a compliance decrease was still observed during this time suggesting that the compliance decrease is independent of the number of creep steps performed on the specimen. This implies that accumulation of mechanically induced structural damage is an unlikely cause for the compliance decrease. In addition, it is speculated that structural breakdown or damage in the specimen resulting from testing would cause the tissue to become more compliant rather than less compliant. A post-yielded specimen is more compliant than prior to yielding, for example, which is a process that produces structural damage. Rather, the tissue is increasing in stiffness, suggestive of dehydration or an aging process. Incidentally, due to the low applied stress of 6 Pa, no yielding was observed in any of the specimens during the consecutive creep testing.

After an extended number of steps, the compliance appeared to approach an asymptote such that the compliance was nearly constant after 25 to 30 steps. This slowing may be the result of some equilibrating process. Combining the information summarized herein, it is reasonable to assume that the decrease in compliance is the result of a dehydration process. Studies have found the viscoelastic behavior of the NP tissue to be particularly sensitive to changes in hydration.[23,37] In addition, similar studies have shown that degenerate NP tissue displays

increased stiffness (decreased compliance) over healthy NP tissue.[37] This also corresponds with gross biomechanical observations due to the progression of IDD and subsequent water content loss, which states that the tissue transitions from fluidlike to solidlike behavior.[55]

In general, it is believed that the appearance of microscopic droplets observed around the periphery of the NP during the mineral oil dye testing is due to water migration and diffusion out through the NP "membrane." Initially, no droplets could be seen in the mineral oil. After a number of hours, a few droplets could be observed. The quantity of the droplets increased in magnitude over several days such that minimal effort was necessary in observing the droplets within a week. In addition, after two weeks, the presence of small, rod-like objects were observed in the mineral oil at 40x magnification that had not been noticeable initially. While the identity of these objects is still unknown, one may be tempted to speculate that the rod-like objects are proteoglycans that have leached out of the specimen. This is a reasonable assumption since, almost immediately following submersion in a bath of saline solution, NP tissue swells rapidly and proteoglycans leach out of the specimen.[6,7] However, some may argue that the proteoglycan should not be so readily visible, despite their macromolecular nature. Regardless if the observed objects are indeed proteoglycans, the possibility remains that proteoglycans are leaching into the mineral oil. It is also unknown at this point whether the proteoglycan leaching would follow apparent dehydration of the tissue or whether proteoglycan leaching into mineral oil precedes and initiates dehydration. The question is raised as to whether the apparent dehydration is an osmotic pressure or diffusion gradient issue. In the event that the speculated proteoglycan leaching follows dehydration, it may be possible to immerse the tissue in a solution with an equal osmotic pressure to that of the specimen, thereby reducing or eliminating the diffusion of water and minimizing dehydration. One study looking at the swelling pressure of

the IVD used different concentration solutions of polyethylene glycol (PEG) to study the effects of osmotic pressure on the IVD.[7] It was found that lower concentration solutions allowed the specimen to swell while higher molecular weight solutions caused the IVD to shrink. An optimal concentration was achieved where the concentration was equal in osmotic pressure to the IVD, maintaining the original shape and hydration of the tissue.[7] If the NP specimens of the current study are equilibrating osmotic pressures or diffusion gradients of some kind, it is possible that different molecular weights and solution concentrations may be "calibrated" experimentally to result in specific levels of specimen water content (e.g., 90%, 80%, etc.) upon equilibration of the specimen to the surroundings. In this respect, this could also lead to another way to control the hydration of the specimen.

Therefore, dehydration appears to explain the compliance decrease in the specimen as time elapses when using mineral oil. This is evidenced by results of the analysis of the consecutive compliance testing in addition to the observance of droplets increasing in quantity in the mineral oil after a number of hours or days. If dehydration is indeed occurring, the exact mechanism is still unknown and the remedy is also uncertain. Ultimately, more testing is necessary in order to further the understanding related to this issue.

6.4 HUMIDITY CHAMBER EXPERIMENTATION

An increase in temperature was shown to result in a vertical shift of the creep compliance at short times. According to analytical and numerical analysis techniques, the temperature gradient in the specimen may be neglected during testing at elevated temperatures, such as 40 ºC. The humidity chamber is capable of operating in such a way that the creep compliance increases or

decreases between consecutive tests. In addition, a middle ground may be found such that the level of creep compliance is essentially maintained.

Results of the temperature gradient analysis indicate a temperature difference of about 1.5 ºC to 2 ºC across the specimen. At a Peltier plate temperature of 40 ºC, the tissue would still be within the core temperature of the rabbit at the tissue-cone interface so this is acceptable. However, two major boundary condition assumptions in the FEA model may have resulted in improved heat transfer through the specimen, so the true temperature difference may be reduced. The ideal contact conditions between the tissue and stainless steel cone as well as between the cone and aluminum shank are somewhat unrealistic. Particularly between the cone and shank, the surface discontinuities between these solid objects help to insulate the cone and the specimen from the high thermal conductivity and resulting high heat transfer of the aluminum. In addition, thermal radiation and convective heating effects from the Peltier plate were ignored in the model, which are expected to help in buffering the thin tissue from convection affects of the ambient environment. Therefore, the true temperature difference in the material may be less than 1 ºC. It is important that the tissue be at an approximately constant temperature throughout since temperature dependent behavior, such as the increased compliance demonstrated in the specimen during the consecutive creep testing, to minimize inaccuracies that may otherwise result in the behavior of the specimen. This may be ensured through the use of an "oven," which surrounds the test geometry and specimen to aid in producing a constant temperature in the specimen. However, these units tend to be cumbersome and will not interface well with the humidity chamber so the ability to test at the core temperature of the rabbit in the absence of an oven is desirable.

Similar to the mineral oil, the humidity chamber also displayed decreasing creep compliance in some instances. However, in contrast to the mineral oil, the recovery was observed to increase in measured compliance during these instances, suggesting the accumulation of memory effects and an increase in recovery potential. One advantage of the active humidification is the relative ability to control the hydration and change. This is beneficial for studies where alteration and controllability of the hydration is desired over constant water content. For example, the humidity chamber is particularly suitable for studies that look at the effect of hydration on the viscoelastic behavior of the specimen, as this type of study would require precise and responsive control of the specimen hydration. On the contrary, hydration maintenance such as equilibrating a specimen in a PEG solution may prove more stable for testing where alteration of specimen hydration is not desired since the humidity within the chamber is rather sensitive to slight adjustments of the humidifier controls. Additional disadvantages of the humidity chamber are that it requires more attention from the experimenter with a more complicated setup and equilibration procedure. Condensation effects are also a concern during operation. Photographs of the humidity chamber in operation are provided in Figure 6.2 and Figure 6.3. Slight condensation may be observed on the walls and bottom surface of the chamber. However, accumulation of condensation onto the Peltier plate, specimen, or cone tended not to occur during active humidification testing mode with the humidifier on low output settings. It should be noted that the results obtained while using the humidity chamber are preliminary and require validation since few specimens were tested during its use and the testing procedures are still under development.

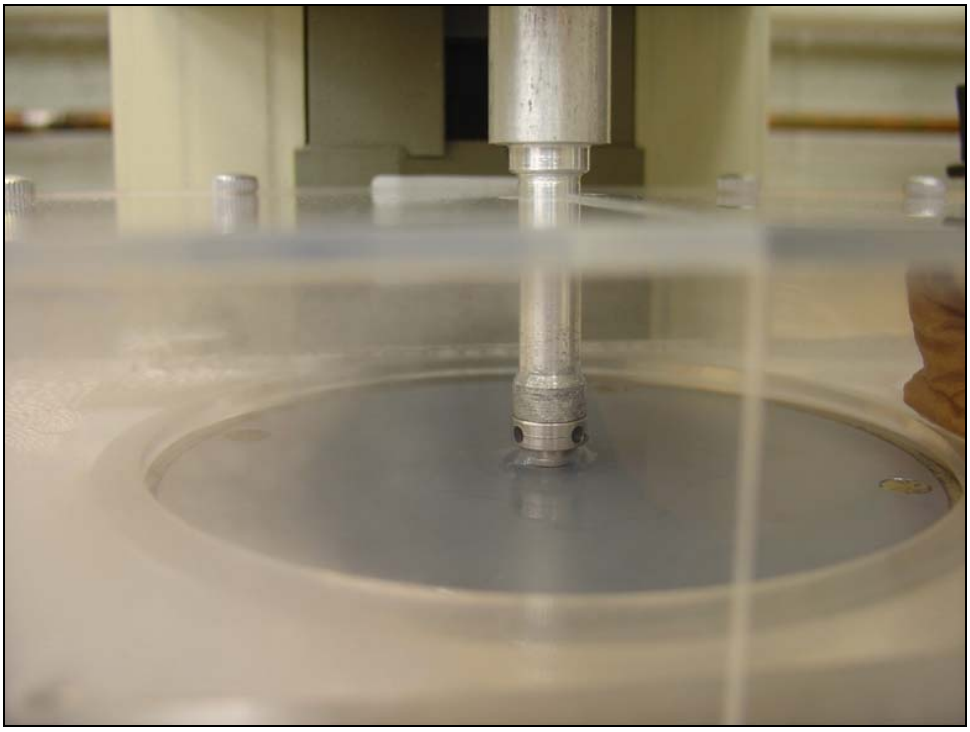

Figure 6.2 Photograph of cone and plate while testing with humidity chamber.

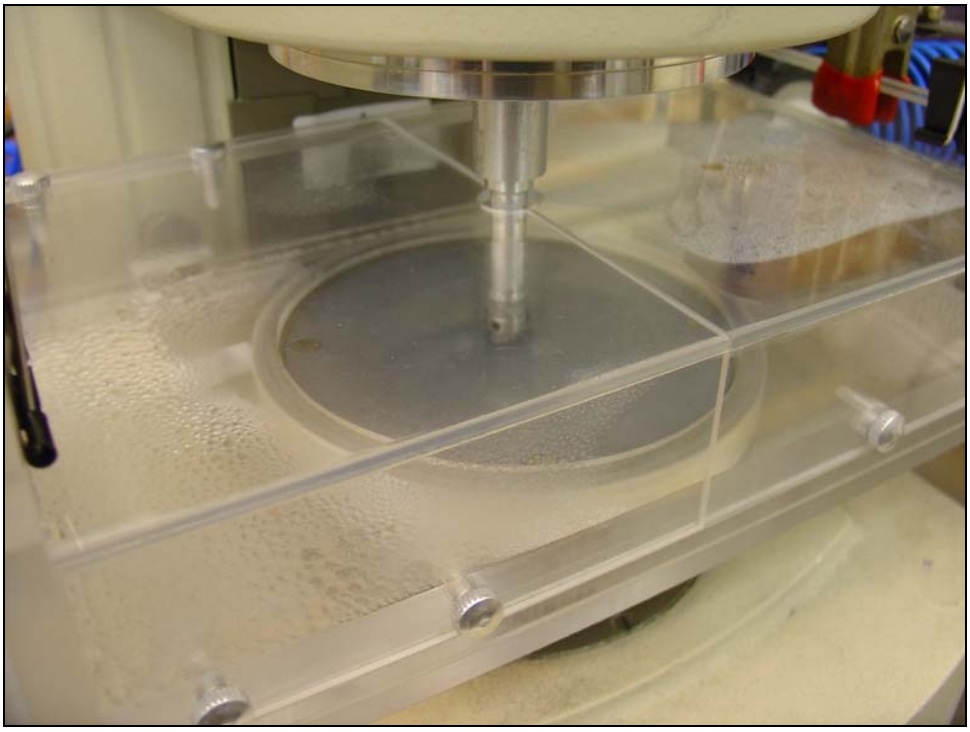

Figure 6.3 Photograph of the humidity chamber in operation during testing of specimen.

7.0 CONCLUSION

Traditionally, stress relaxation testing has been used to model biological tissues and evaluate their treatments. However, limitations exist in the ability of stress relaxation testing to adequately characterize the viscoelastic behavior of certain biological tissues.[78] As a result, some researchers have proposed that creep testing, though less common, may serve as a more suitable alternative for testing of biological tissues.[81] It is on this belief that the material testing technique of the current study is based. Through the current study, healthy rabbit NP tissue was determined to display nonlinear viscoelastic behavior that may be approximated by the QLV theory. The mean critical strain of the tissue was determined to be within the range of 1.91 to 3.67 at 95% confidence. The Andrade creep model was determined to provide a strong fit to the entire data range and also proved suitable for extrapolation of data using parameters fit over 300 s. In accordance with the viscoelastic nonlinearity of the NP tissue, the Boltzmann superposition principle is not obeyed. The strain behavior of the tissue may be described and predicted by the constitutive model provided by equation 4.24,

$$\gamma(t) = J_A\tau + A\tau^m t^{1/3} + \tau\frac{t}{\eta},$$

where the stress power, m, is determined from the slope of lines of isochronal data on log-log axes of strain versus stress. This constitutive model is the QLV formulation of the Andrade creep model. It was determined that water from within the tissue specimens may be permeating out into the mineral oil, resulting in a decrease in specimen water content and a subsequent

decrease in compliance with time. The use of a humidity chamber may be used to help minimize or prevent water loss and a subsequent compliance decrease. However, added complexity results when operating the humidity chamber and further development of this procedure is required since data obtained using the chamber is preliminary. The possibility of using solutions with different osmotic pressures to control hydration within the specimen may also need to be explored.

Ultimately, this study successfully determined a constitutive model capable of predicting the creep strain of healthy rabbit NP tissue and applied meso-scale rheological testing methods to establish viscoelastic properties of the tissue in torsional creep. Using this model to predict the behavior of degenerated rabbit NP tissue is expected to provide quantifiable, functional benchmarks of success for molecular therapy approaches to the treatment of IDD.

8.0 FUTURE WORK

Future direction of this study will focus on obtaining additional experimental data to support and refine the constitutive model gained through the research presented herein. Degenerated and treated rabbit NP tissue will be tested to build a database of model parameters for these specimen states. Additional development of procedures and testing will be performed to facilitate in the use of the humidity chamber and additional focus will be placed on improving the use of mineral oil or alternative methods of maintaining hydration. For example, testing may be performed using concentrations of PEG that balance the NP osmotic pressure and maintain initial swelling levels within the specimen. Possible existence of a time-hydration superposition analogous to the time-temperature superposition has been indicated[23] and some investigation may be aimed at determining if a "master curve" can be constructed pertaining to creep at various levels of hydration. Attempts will be made to predict the recovery using nonlinear viscoelastic superposition formulations and additional nonlinear theories more general than QLV will continue to be explored.

APPENDIX A

MANUAL CURVE FITTING OF ANDRADE CREEP MODEL

Manual Curve Fitting Methods[84]: The objective of fitting the Andrade creep model to the NP tissue data was to ascertain whether it provided a suitable power law creep model, as indicated by preliminary observations upon plotting compliance versus the cube root of time. From equation 2.15, the Andrade creep model in modified form to include viscous deformation, $J(t) = J_A+\beta t^{1/3}+t/\eta$, was fit to the creep data, where J_A is the Andrade intercept, β is the Andrade slope, and η is the viscosity. A least squares linear regression, neglecting the viscous processes (t/η) term, was used to fit J(t) to the data on axes of compliance versus the cube root of time, in the time range of 1 to 50 s. The slope of the linear regression provided the value for β while the intercept with the ordinate axis provided J_A. Upon inputting the newly obtained values of β and J_A from the first 50 seconds into

$$J_r(t) = J_A+\beta t^{1/3}, \qquad (A.1)$$

the t/η term was calculated for all of time, t, by taking the difference between the experimental compliance data, J(t), and the predicted recoverable compliance, Jr(t). Plotting t/η versus time was expected to result in a straight line intersecting the origin, from which the inverse slope of the line produced the viscosity, η. This process is demonstrated in Figure A.1. Having

determined the model parameters, β, J_A, and η, the model could now be used to predict additional creep or recovery behavior and fit statistics could be assessed.

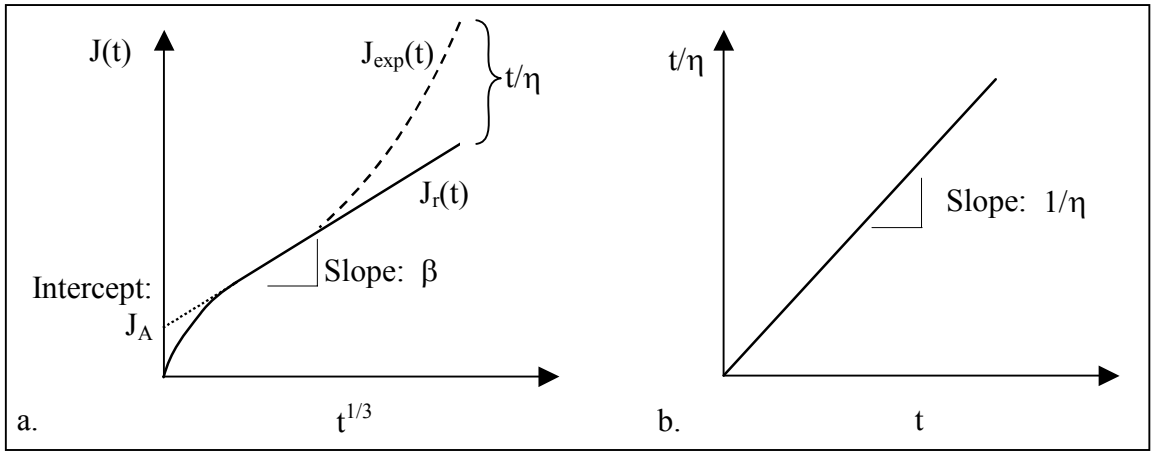

Figure A.1 Andrade creep parameter determination (a) and determination of viscosity, η (b).

Manual Curve Fitting of Andrade Creep Model Results: The Andrade creep model applied using the manual curve fitting method described by Plazek[84] corresponded to the data well. A representative plot of compliance versus cube root of time may be seen in Figure A.2, providing the original data and the data with the viscous term subtracted from it. The slope, 2.6×10^{-3} $Pa^{-1}.t^{1/3}$, of the straight line contributes the β term of the Andrade equation while the intercept, 1.6×10^{-3} Pa^{-1}, produces J_A. In Figure A.3, the viscous term is shown as a straight line plotted on axes of t/η versus time, where the inverse of the slope yields the viscosity, η = 0.3 MPa.s. Manually fit model parameters and fit statistics are provided in Table 5.4 for the five specimens analyzed. The R^2 values are for the linear regression fit to the first 50 seconds of experimental data creep plotted on Andrade axes in Figure A.4.

Initially, the manually determined and computer assisted fits of the Andrade creep model are compared. Referring back to Tables A.1 and A.2, it may be seen that the mean values for each of the parameters, J_A and β, fall within 5% of each other. However, the viscosity values show considerably greater variation. This is shown in Figure A.5, where the hand fit viscosity was much larger than the computer determined value in specimens 2 and 5. It should also be noted that the largest variations occurred with the specimens having the greatest viscosity, suggesting increasing model sensitivity to viscosity as the model approaches a viscoelastic solid (i.e., as the viscosity becomes infinite).

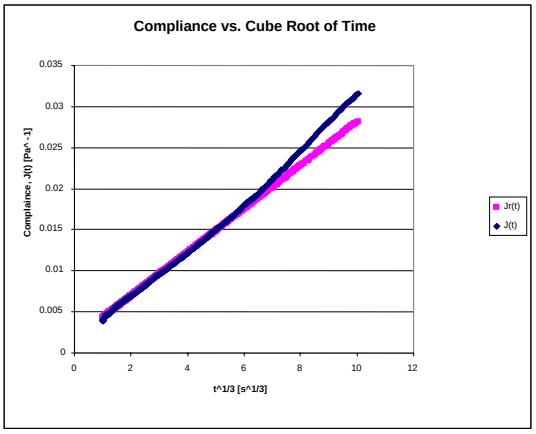

Figure A.2 Experimental and recoverable compliance plotted against the cube root of time.

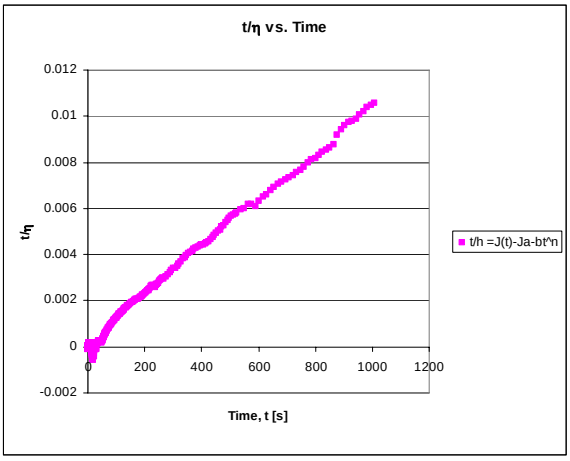

Figure A.3 Viscous contribution to deformation. Viscosity is obtained from inverse slope.

Table A.1 Fit statistics and model parameters for manually fit Andrade creep model.

Specimen	R^2 from 1 – 50 seconds	Beta flow slope, β	Intercept, J_A	Viscosity, η
	(Units)	($Pa^{-1}.s^{1/3}$)	(Pa^{-1})	(Pa.s)
1 (rab 8)	0.9987	2.647E-03	1.642x10-03	283552
2 (rab 9)	0.9981	6.502E-04	6.153 x10-04	2591424
3 (rab12)	0.9897	2.037E-03	1.128 x10-03	93118
4 (rab13)	0.9987	2.155E-03	1.203 x10-03	141882
5 (rab15)	0.9962	2.767E-03	2.503 x10-03	1157337
Mean	0.9963	2.051E-03	1.418 x10-03	853463
Std Dev	0.0038	8.429E-04	7.075 x10-04	1063264

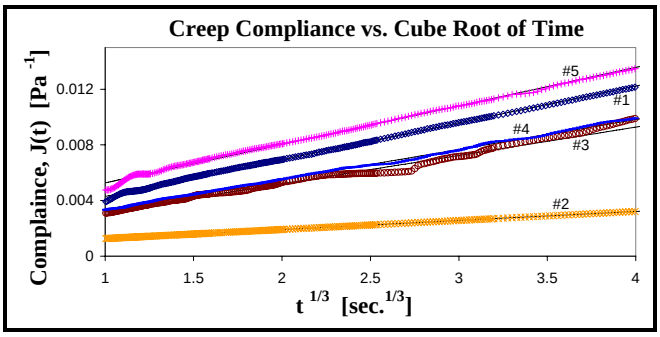

Figure A.4 Linear regression fits to data on J(t) vs t^1/3 axes.

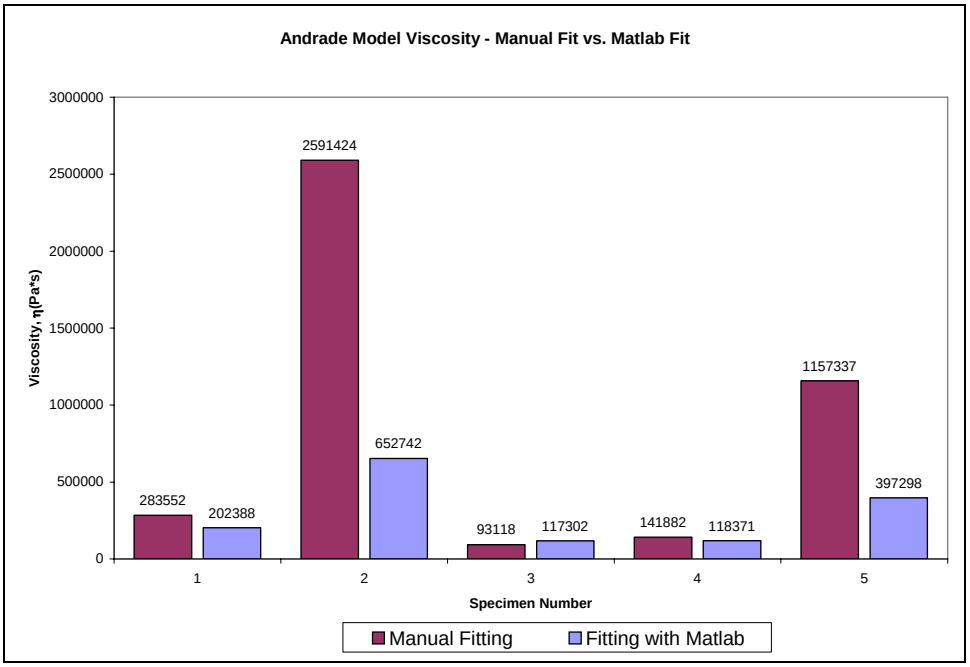

Figure A.5 Manually and computer determined viscosity values for Andrade creep model.

a.

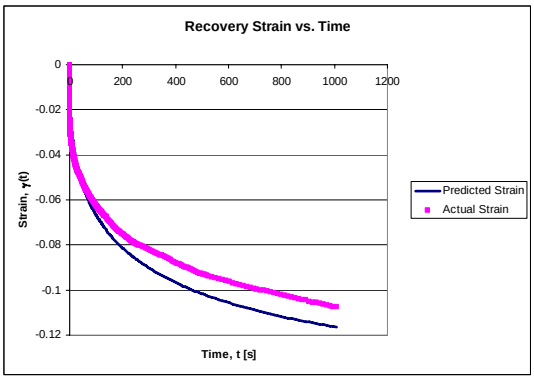

b.

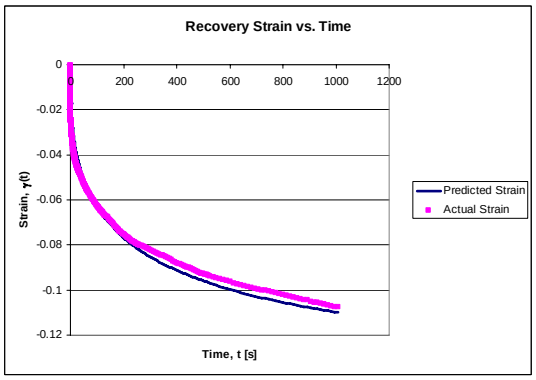

Figure A.6 *Rab 8* - Actual and predicted recovery of manual (a) and computer (b) fit creep.

a.

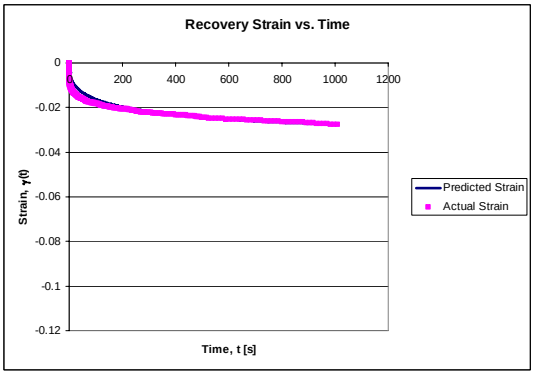

b.

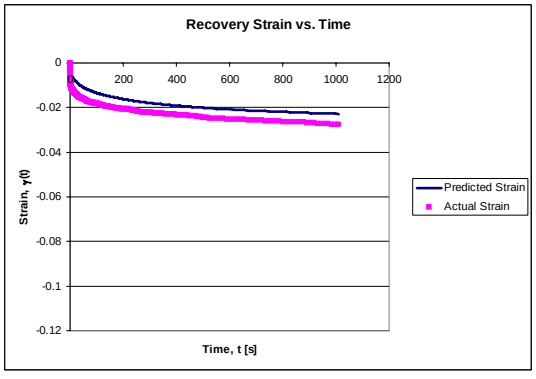

Figure A.7 *Rab 9* - Actual and predicted recovery of manual (a) and computer (b) fit creep.

a.

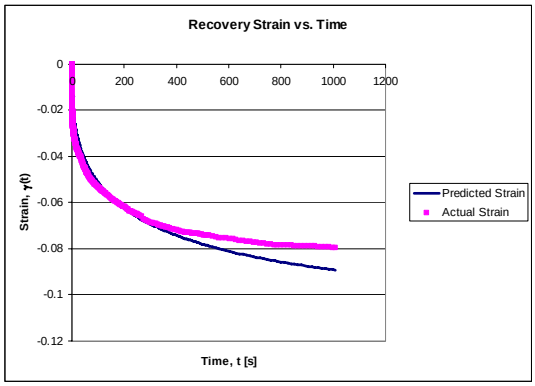

b.

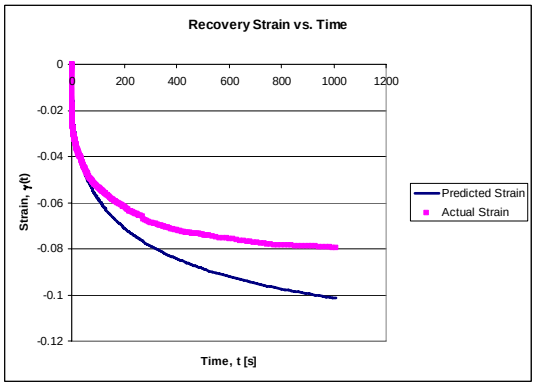

Figure A.8 *Rab 12* - Actual and predicted recovery of manual (a) and computer (b) fit creep.

a.

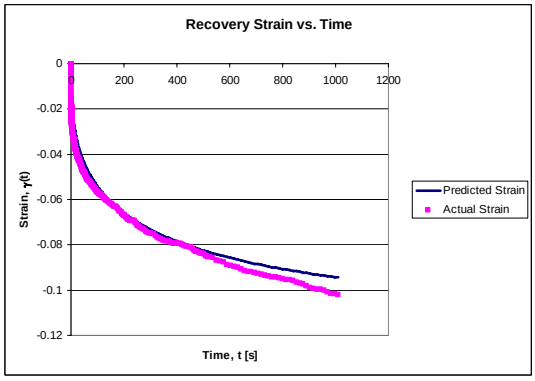

b.

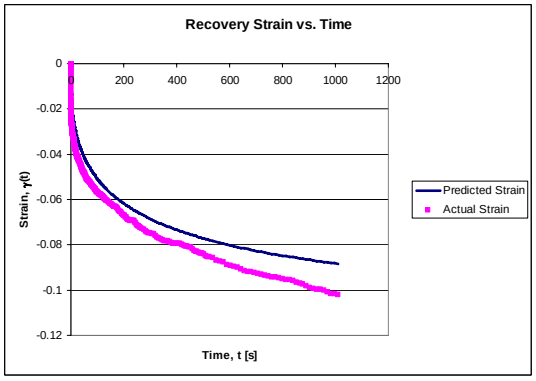

Figure A.9 *Rab 13* - Actual and predicted recovery of manual (a) and computer (b) fit creep.

a.

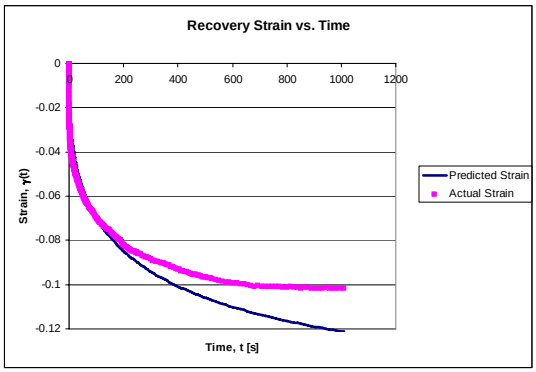

b.

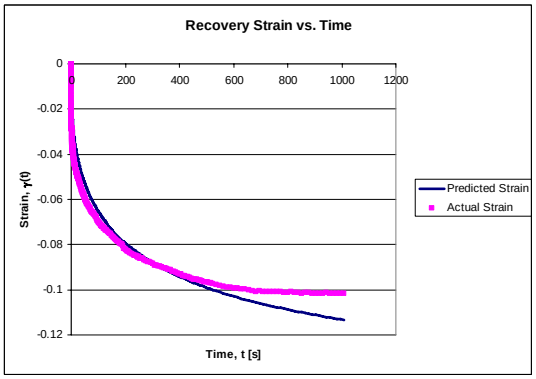

Figure A.10 ***Rab 15*** **- Actual and predicted recovery of manual (a) and computer (b) fit creep.**

Table A.2 Comparison of computer vs. manual model fits.

	Manual fit		Computer fit	
Measure of Fit	**R^2**	**SSE**	**R^2**	**SSE**
rab8	0.9620	0.01073	0.9816	0.00518
rab9	0.8561	0.00234	0.5264	0.00770
rab12	0.9558	0.00761	0.8551	0.02495
rab13	0.9751	0.00626	0.9304	0.01748
rab15	0.9405	0.01695	0.9483	0.01472
mean	0.9379	0.00878	0.8484	0.01401
std dev	0.0474	0.00547	0.1859	0.00791

APPENDIX B

ISOCHRONAL DATA R^2 AND ADJUSTED-R^2 VALUES

Table B.3 R^2 and adjusted-R^2 values of isochronal data 1st and 2nd order regressions.
Isochronal data was plotted on linear axes of stress versus strain at times of 10.18, 30.25, 60.56, and 101.5 s in Section 5.2.4. Linear and quadratic regressions were applied to the data at each time. In Section 5.2.4, only the R^2 and R^2_{adj} values at times of 10.18 s were provided. The R^2 and R^2_{adj} values for all of the indicated times are provided in this table.

Specimen	Time	Linear R^2	Quad R^2	Linear Adj-R^2	Quad Adj-R^2	Notes
Rab 8	10.18 s	0.9962	0.9978	0.9962	0.9967	
	30.25 s	0.9931	0.9982	0.9931	0.9973	
	60.56 s	0.9879	0.9985	0.9879	0.9978	
	101.5 s	0.9809	0.9987	0.9809	0.9981	
Rab 9	10.18 s	0.9923	0.999996	0.9923	0.99999	
	30.25 s	0.9891	0.999988	0.9891	0.99998	
	60.56 s	0.9865	0.999983	0.9865	0.99997	
	101.5 s	0.9847	0.99998	0.9847	0.99997	
Rab 12	10.18 s	0.9869	0.999993	0.9913	0.99999	
	30.25 s	0.9818	0.999989	0.9879	0.99999	
	60.56 s	0.9739	0.99996	0.9826	0.99996	
	101.5 s	0.9625	0.99977	0.9750	0.99977	Yielded
Rab 13	10.18 s	0.9922	0.999868	0.9922	0.99980	
	30.25 s	0.9825	0.999985	0.9825	0.99998	
	60.56 s	0.966	0.999979	0.966	0.99997	Yielded
	101.5 s	0.9477	0.999985	0.9477	0.99998	Yielded
Rab 15	10.18 s	0.9936	0.9955	0.9936	0.99325	
	30.25 s	0.9945	0.9954	0.9945	0.99310	
	60.56 s	0.9949	0.9953	0.9949	0.99295	
	101.5 s	0.9952	0.9954	0.9952	0.99310	

APPENDIX C

POST-YIELD MENDING TESTING

Post-yield Mending Testing Methods: The objective of post-yield mending testing was to determine if, after inducing structural damage to the specimen by yielding, the specimen would approach its initial pre-yield compliance level by a mending process. To achieve this, the specimen was installed and covered with a light coating of mineral oil. The specimen was subjected to pre-yield creep testing at a shear stress of 6 Pa for 35 seconds and permitted to recover for 20 minutes. This pre-yield creep testing was repeated a second time to create baseline compliance data for the pre-yielded state. Following the two initial creep tests at low stress and short duration, the specimen was creep tested at a shear stress of 162 Pa until yielding was observed. The onset of yielding was identified by observation of a positive acceleration of the compliance data on linear axes of compliance versus time. Yielding was then verified by observing a slope greater than or equal to unity on log-log axes of compliance versus time, upon which time the creep test was halted and the specimen permitted to recover until the rate of recovery was 1% (or $1/100^{th}$) of the initial creep rate during the two pre-yield tests. Once the rate of recovery was sufficiently slow, the recovery was halted and post-yield creep testing was begun. The post-yield creep testing procedure was identical to the pre-yield testing, creeping at a

shear stress of 6 Pa for 35 seconds followed by a 20 minute recovery. The post-yield creep testing was continuously repeated for several days to measure if the post-yield creep compliance would once again approach the initial level of the pre-yield creep compliance, the occurrence of which would indicate the ability of the specimen to mend.

Post-yield Mending Testing Results (N = 1 with mineral oil, N = 1 with humidity chamber): In general, it is possible that mending occurs. However, inadequate confidence in the ability to precisely control specimen hydration with the humidity chamber and possible dehydration despite the use of mineral oil may be dominating. Therefore, further testing is needed to determine if mending occurs or not. This has not been pursued since it is necessary to stabilize consecutive creep tests prior performing additional post-yield mending tests. Additionally, a lack of these data did not directly interfere with achieving the specific aims of this research. Figure C.11 and Figure C.12 provide test results for post-yield mending testing with the use of mineral oil and the humidity chamber, respectively, to maintain specimen hydration. Determination of whether or not the tissue is capable of mending may provide insight into the collagen-collagen as well as the collagen-proteoglycan interactions within the material. In addition, deviations between mending behavior of healthy and degenerated or treated tissue may provide further insight into treatments effectiveness.

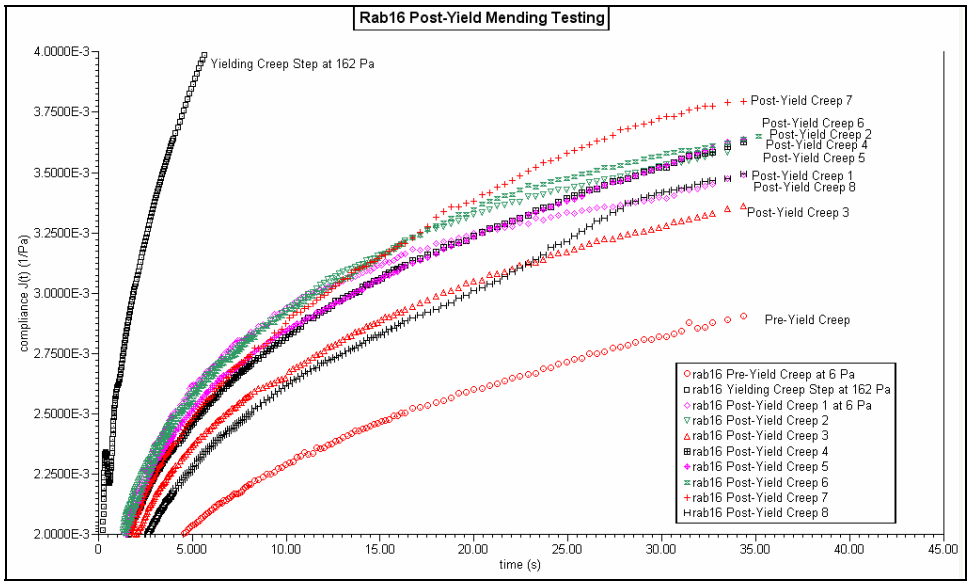

Figure C.11 Post-yield mending testing plot for specimen tested using mineral oil.

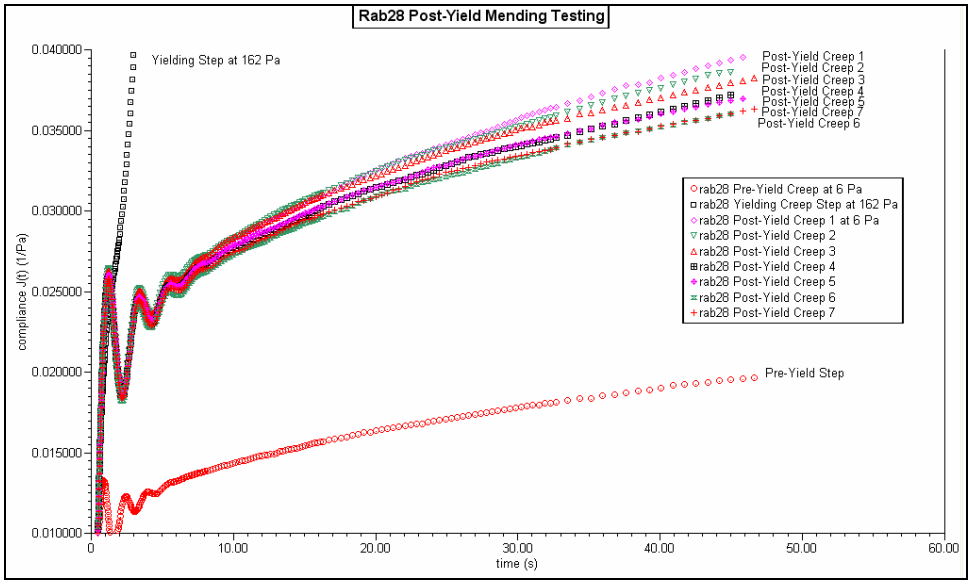

Figure C.12 Post-yield mending plot for specimen tested with humidity chamber.

In general, it appears that the specimen is approaching the original pre-yield compliance level. However, it is uncertain whether the decrease in compliance is truly due to mending or whether some other influence such as dehydration is causing the noted behavior. Thus, the post-yield mending testing is in conclusive and further testing is needed. The oscillations appearing within the first 10 seconds are due to inertial effects at each creep step start.

APPENDIX D

CONSTITUTIVE MODEL USING COMBINED MODEL PARAMETERS

A preliminary constitutive model of the rabbit NP tissue was determined. Model parameters obtained for each specimen by computer fitting of the Andrade creep model to 6 Pa creep data were combined and the mean values used to form the general model parameters. The standard deviation was used to produce error bars for the model. Only the model parameters from Rab 8, 12, 13, and 15 were used. The parameters from Rab 9 were omitted since it was a visible outlier. Determination of the parameters is seen in Table D.4.

Table D.4 Determination of constitutive model parameters with Rab 9 as an outlier.

Specimen	R^2	SSE	Slope, β ($x10^3$) [$Pa^{-1}.s^{-1/3}$]	Andrade Const., J_A ($x10^3$) [Pa^{-1}]	Viscosity, η ($x10^{-6}$) [Pa.s]
1 (Rab 8)	0.99979	2.82×10^{-6}	2.499	1.900	0.2024
~~2 (Rab 9)~~	~~0.99947~~	~~2.77×10^{-7}~~	~~0.5360~~	~~0.8912~~	~~0.6527~~
3 (Rab 12)	0.99951	7.22×10^{-6}	2.315	0.1109	0.1173
4 (Rab 13)	0.99944	6.71×10^{-6}	2.015	1.354	0.1184
5 (Rab 15)	0.99980	2.22×10^{-6}	2.586	2.924	0.3973
Mean	0.99964	4.74×10^{-6}	2.3538	1.5722	0.2089
Std Dev	0.00019	2.59×10^{-6}	0.2525	1.1716	0.1318

By definition, an outlier is a value that is 1.5 times larger (or smaller) than the *fourth spread*, the difference between the mean of the upper 25% of data and the mean of the lower 25% of data.[92] However, the number of specimens (n = 5) is insufficient to produce the resolution necessary for statistically defining Rab 9 as an outlier. Therefore, Rab 9 is *declared* an outlier based on visual observation of the spread of the data overall. This may be seen in Figure D.13. Thus, inputting the parameters in Table D.4 into equation 2.15 gives the constitutive model of the tissue at 6 Pa,

$$J(t)_{Rabbit,L5-L6,NP,6PaStress} = 0.0015755 + 0.0023538t^{1/3} + t/208900 \quad [\text{Pa}^{-1}], \tag{D.2}$$

where time, t, is in seconds. The constitutive model is plotted with actual data in Figure D.13.

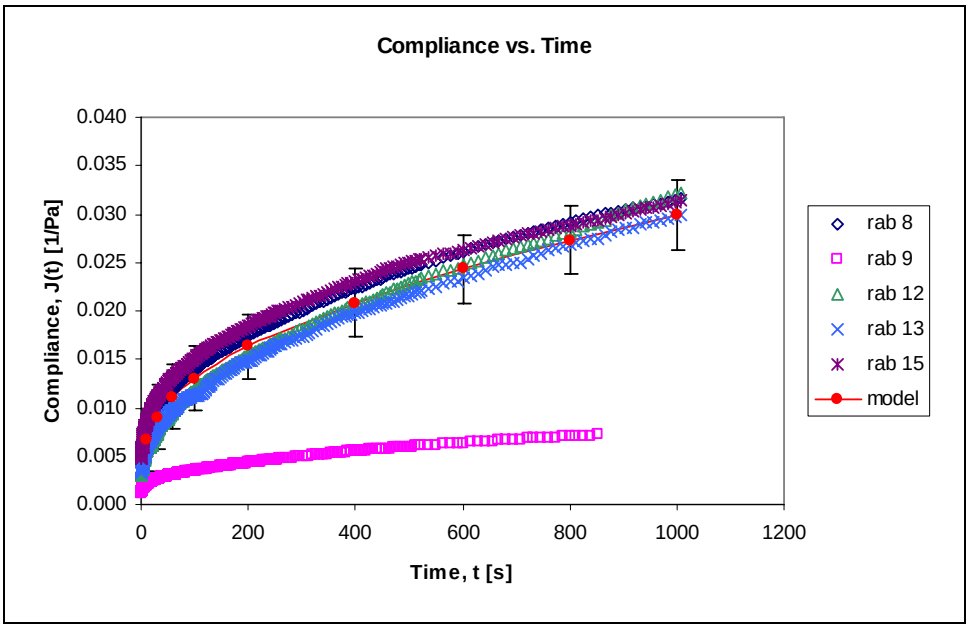

Figure D.13 Compliance versus time plot of 6 Pa creep data and general constitutive model.
The general constitutive model for the tissue is based on model parameters obtained by computer assisted fitting of Rab 8, 12, 13, and Rab 15 creep data at 6 Pa applied stress. Rab 9 data was declared a visible outlier and omitted from determination of the general constitutive model. Excluding Rab 9, the remaining data and error bars are well within 20% of the determined model. It should be noted that the parameter values of this general model are preliminary.

APPENDIX E

VARIABLE HYDRATION TESTING MASTER CREEP CURVES

In order to study the effects of hydration more fully, preliminary experiments were performed using the humidity chamber where either increased hydration or dehydration were promoted. In the case where dehydration was promoted, the humidity chamber was essentially turned off and allowed to decrease in humidity. Along with this occurrence, the specimen was believed to also begin giving up hydration to the atmosphere. Figure E.14 shows the resulting behavior when the humidity chamber was switched off and the specimen dehydrated significantly over 50 creep steps. Creep steps were performed at 6 Pa for 100 s with 1000 s recovery steps following each creep step. The initial and final hydration levels are unknown.

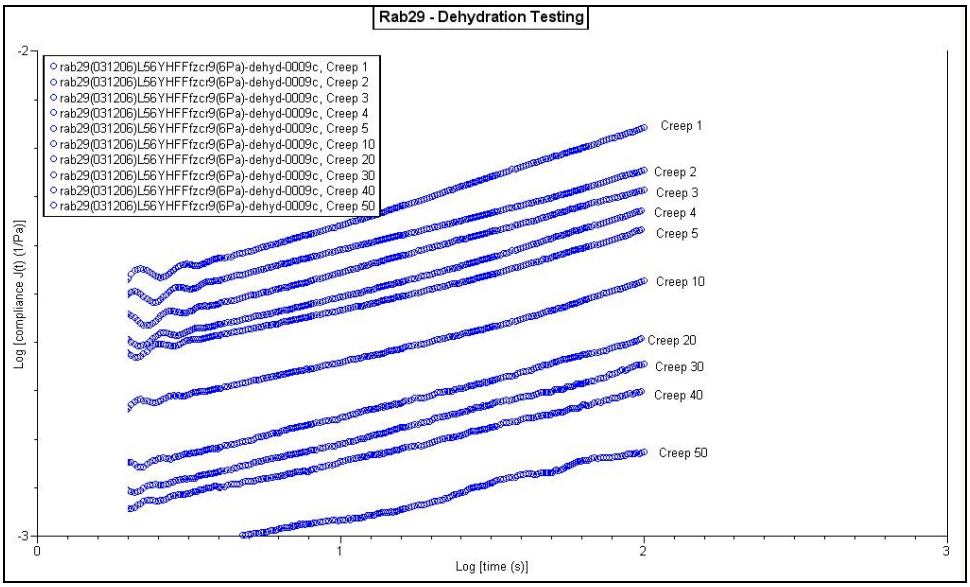

Figure E.14 Log-Log plot of compliance versus time showing dehydration testing results.

In the case where an increase in hydration was promoted, the humidity chamber output was set at a high humidity level causing the specimen to absorb water from the atmosphere. This usually required the humidifier to be set near maximum output. Figure E.15 shows the resulting behavior at a 6 Pa applied creep stress. Creep step duration lasted 300 s while recovery steps lasted 3000 s. Significant alteration of tissue behavior is noticeable as the tissue becomes excessively hydrated. Visual examination of Figure E.15 may lead one to question whether a "time-hydration superposition" exists for the material. In this case, experiments performed within a time interval at increased or decreased levels of hydration produce results similar to those obtained by shifting the time axis for a single creep experiment. This may allow the construction of a "master" creep curve, which displays the creep behavior of a material over many decades of time that would otherwise take a very long time to obtain. In Figure E.16, the creep curves at the different levels of hydration from Figure E.15 have been shifted horizontally along the time axis to produce such a "master" curve. It should be noted that a time-hydration

superposition might not necessarily exist, although it has been suggested by some authors.[23] However, it borrows from the idea of a time-temperature superposition,[69] which does in-fact exist for some materials. The initial, intermediate, and final hydration levels are unknown.

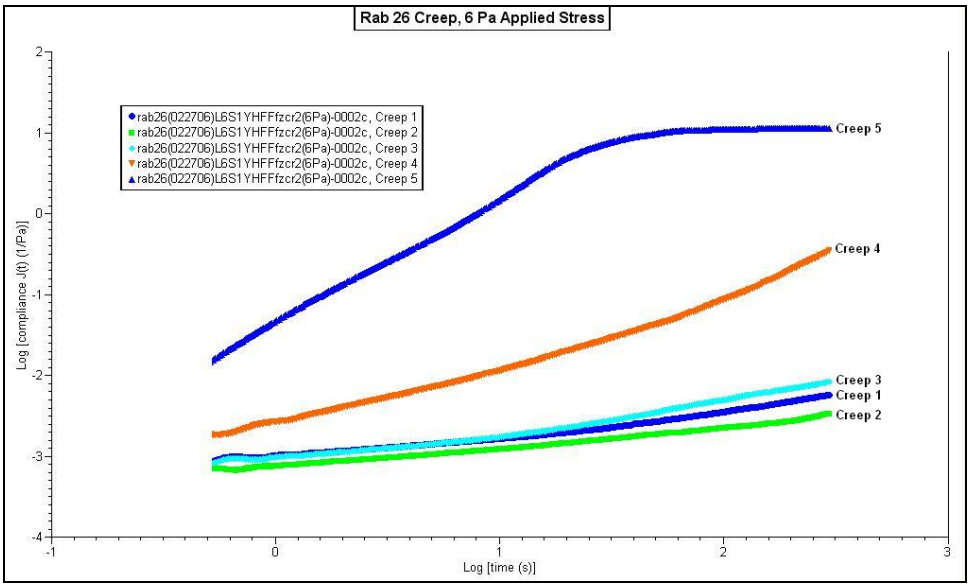

Figure E.15 Plot of creep tests performed at increasing levels of hydration.

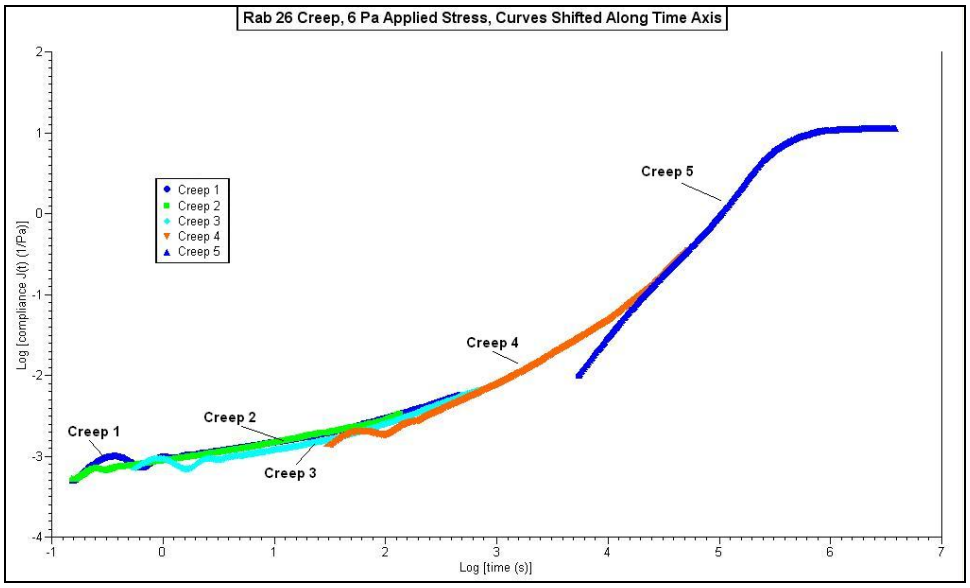

Figure E.16 Master curve constructed from Figure E.15 by shifting along time axis.
Time-hydration superposition "master" curve is demonstrated by horizontally shifting the curves at different levels of hydration along the time axis. The initial, intermediate, and final hydration levels are unknown.

APPENDIX F

DEFINITIONS OF STATISTICAL PARAMETERS [92]

Sum of Squared Error, SSE: The sum of squared error, SSE, is also known as the residual sum of squares and calculates the sum of the squared difference (error) between predicted data points and actual data points within a data series. The SSE is obtained using the equation

$$SSE = \sum_i (y_i - \hat{y}_i)^2 , \tag{F.3}$$

where y_i and $\hat{y}_i$ are ordinate values of the actual and predicted data points, respectively.

Total sum of squares, SST: The total sum of squares, SST, is the sum of the squared difference about the sample mean of ordinate (y-axis) values. The SST is obtained using the equation

$$SST = \sum_i (y_i - \bar{y})^2 , \tag{F.4}$$

where y_i are ordinate values of the actual data points and $\bar{y}$ is the mean of the actual data points.

Coefficient of Multiple Determination, R^2: The coefficient of multiple determination, R^2, is obtained using the equation

$$R^2 = 1 - \frac{SSE}{SST} \quad . \tag{F.5}$$

Adjusted Coefficient of Multiple Determination, R^2_{adj}: The adjusted coefficient of multiple determination adjusts for the number of data points, *n*, and the number of model terms, *k*, since the standard R^2 always increases with increasing model terms. It is obtained using the equation,

$$R^2_{adj} = 1 - \frac{SSE}{SST}\frac{(n-1)}{(n-1-k)} \quad . \tag{F.6}$$

BIBLIOGRAPHY

1. White, AA and MM Panjabi. Clinical Biomechanics of the Spine. Philadelphia, Lippincott. (1978).

2. Jayson, MIV. The Lumbar Spine and Back Pain. Edinburgh, Churchill Livingstone. (1992).

3. Stokes, IAF and JC Iatridis: "Biomechanics of the Spine." Basic Orthopaedic Biomechanics and Mechanobiology, Ed by VC Mow and R Huiskies. New York, Lippincott Williams & Wilkins, (2005), pp. 529-563.

4. Iatridis JC, Setton LA, Weidenbaum M, and Mow VC: "The Viscoelastic Behavior of the Non-degenerate Human Lumbar Nucleus Pulposus in Shear." *J Biomechanics* 30: (1997), pp. 1005-1013.

5. Urban, J: "Disc Biochemistry in Relation to Function." The Lumbar Spine, 2nd Ed. Ed by JN Weinstein and SW Wiesel. Philadelphia, W.B. Saunders Company, (1996), pp. 271-281.

6. Bayliss, MT, Johnstone, B, and O'Brien, JP: "Proteoglycan Synthesis in the Human Intervertebral Disc: Variation With Age, Region, Pathology," *Spine* 13(9): (1988), pp. 972-981.

7. Urban, JPG and A Maroudas: "Swelling of the Intervertebral Disc In Vitro." Connective Tissue Research 9(1): (1981), 1-10.

8. Bayliss, MT and B Johnstone: "Biochemistry of the Intervertebral Disc." The Lumbar Spine and Back Pain. 4th Ed. Ed by MIV Jayson. Edinburgh, Churchill Livingstone. (1992), pp. 111-131.

9. An, HS et al: "Disc Degeneration: Summary." *Spine* 29(23): (2004), pp. 2677-2678.

10. Koeller, W et al: "Biomechanical Behavior of Human Intervertebral Discs Subjected to Long Lasting Axial Loading." *Biorheology* 21: (1985), pp. 675-86.

11. Palmer, EI et al: "The Compressive Creep Properties of Normal and Degenerated Murine Intervertebral Discs." *Journal of Orthopaedic Research* 22: (2004), pp. 164-9.

12. Chin, JR et al: "Compression-Induced Apoptosis in the Mouse Intervertebral Disc is Time and Stress Dependent." *Transactions of the 45th Annual Meeting of the Orthopaedic Research Society* Anaheim, CA, (1999).

13. Burns, ML et al: "Analysis of Compressive Creep Behavior of the Vertebral Unit Subjected to a Uniform Axial Loading Using Exact Parametric Solution Equations of Kelvin-Solid Models: Part I. Human Intervertebral Joints." *Journal of Biomechanics* 17: (1984), pp. 113-130.

14. Keller, TS et al: "In Vivo Creep Behavior of the Normal and Degenerated Porcine Intervertebral Disc: A Preliminary Report." *Journal of Spinal Disorders* 1: (1988), pp. 267-278.

15. Kazarian, LE et al: "Creep Characteristics of the Human Spinal Column" *Orthopedic Clinics of North America* 6: (1975), pp. 3-18.

16. Dhillon, N et al: "Effect of Frozen Storage on the Creep Behavior of Human Intervertebral Discs." *Spine* 26: (2001), pp. 883-888.

17. Kroeber, MW et al: "New in Vivo Animal Model to Create Intervertebral Disc Degeneration and to Investigate the Effects of Therapeutic Strategies to Stimulate Disc Regeneration." *Spine* 27: (2002), pp. 2684-2690.

18. MacLean, JJ et al: "Effects of Immobilization and Dynamic Compression on Intervertebral Disc Gene Cell Expression in Vivo." *Spine* 28: (2003), pp. 973-981.

19. Ching, CT et al: "The Effect of Cyclic Compression on the Mechanical Properties of the Inter-vertebral Disc: an in vivo Study in a Rat Tail Model." *Clinical Biomechanics (Bristol, Avon)* 18: (2003), pp. 182-189.

20. Walsh, AJ et al: "Biological Response of the Intervertebral Disc to Dynamic Loading." *Journal of Biomechanics* 37: (2003), pp. 329-337.

21. Johannessen, W et al: "Intervertebral Disc Mechanics are Restored Following Loading and Unloaded Recovery." *Annals of Biomedical Engineering* 32: (2004), pp. 70-76.

22. Koeller, W et al: "Biomechanical Properties of Human Intervertebral Discs Subjected to Axial Dynamic Compression: Influence of Age and Degeneration." *Journal of Biomechanics* 19: (1985), pp. 807-816.

23. Panagiotacopulos, ND, Bloch, R, Knauss, WG, Harvey, P and Patzakis, M: "Viscoelastic Behavior of the Human Intervertebral Disc Under Consideration of Moisture Migration." Project Report. California Institute of Technology, Pasadena, CA, USA. (1977) [CaltechAUTHORS:PANafosr77-3139]

24. Kelley, BS, Lafferty, JF, Bowman, DA, and Clark, PA: "Rhesus Monkey Intervertebral Disc Viscoelastic Response to Shear Stress." *Journal of Biomechanical Engineering* 105(1): (1983), pp. 51-54.

25. Elliot, DM et al: "Young Investigators Award Winner: Validation of the Mouse and Rat Disc as Mechanical Models of the Human Lumbar Disc." *Spine* 29: (2004), pp. 713-22.

26. Lotz, JC et al: "Compression-Induced Degeneration of the Intervertebral Disc: An In Vivo Mouse Model and Finite-Element Study." *Spine* 23: (1998), pp. 2493-2506.

27. Iatridis, JC et al: "Compression-Induced Changes in the Intervertebral Disc Properties in a Rat Tail Model." *Spine* 24: (1999), pp. 996-1002.

28. Ohshima, H et al: "Water Diffusion Pathway, Swelling Pressure, and Biomechanical Properties of the Intervertebral Disc During Compression Load." *Spine* 14: (1989), pp. 1234-1244.

29. Court, C et al: "The Effect of Static In Vivo Bending on The Murine Intervertebral Disc." *The Spine Journal* 1: (2001), pp. 239-245.

30. McMillan, DW et al: "Effect of Sustained Loading on The Water Content of The Intervertebral Discs: Implications for Disc Metabolism." *Annals of the Rheumatic Diseases* 55: (1996), pp. 880-887.

31. Langrana, N et al: "Biomechanical Analysis of Loads on the Lumbar Spine." The Lumbar Spine, 2nd Ed. Ed by JN Weinstein and SW Wiesel. Philadelphia, W.B. Saunders Company, (1996), pp. 281-285.

32. Lotz, JC: "Animal Models of Intervertebral Disc Degeneration: Lessons Learned." *Spine* 29(23): (2004), pp. 2742–2750.

33. Bradford, DS et al: "Chymopapain, Chemonucleolysis, and Nucleus Pulposus Regeneration: A Biochemical and Biomechanical Study." *Spine* 9: (1984), pp. 135-147.

34. Van Deursen, DL et al: "In Vitro Torsion-Induced Stress Distribution Changes in Porcine Intervertebral Discs." *Spine* 26: (2001), pp. 2582-2586.

35. Kasra, M et al: “Effect of Dynamic Hydrostatic Pressure on Rabbit Intervertebral Disc Cells.” *Journal of Orthopaedic Research* 21: (2003), pp. 597-603.

36. Iatridis, JC, Weidenbaum, M, Setton, LA, Mow, VC: “Is the Nucleus Pulposus a Solid or a Fluid? Mechanical Behaviors of the Nucleus Pulposus of the Human Intervertebral Disc.” *Spine* 21(10): (1996), pp. 1174-1184.

37. Iatridis JC, Setton LA, Mow VC, Weidenbaum M: “Alterations in the Mechanical Behavior of the Human Lumbar Nucleus Pulposus with Degeneration and Aging.” *Journal of Orthopaedic Research* 15: (1997), pp. 318-322.

38. Urban, JP et al: “Swelling Pressure of the Inervertebral Disc: Influence of Proteoglycan and Collagen Contents.” *Biorheology*22: (1985), pp. 145-157.

39. Rannou, F et al: “Cyclic Tensile Stretch Modulates Proteoglycan Production by Intervertebral Disc Annulus Fibrosus Cells Through Production of Nitrite Oxide.” *Journal of Cell Biochemistry* 90: (2003) pp. 148-157.

40. Iatridis JC, Kumar S, Foster RJ, Weidenbaum M, Mow VC: “Shear Mechanical Properties of Human Lumbar Annulus Fibrosus.” *Journal of Orthopaedic Research* 17(5): (1999), pp. 732-737.

41. Iatridis JC, Setton LA, Foster RJ, Rawlins BA, Weidenbaum M, Mow VC: “Degeneration Affects the Anisotropic and Nonlinear Behaviors of Human Anulus Fibrosus in Compression - Influence of Age, Spinal Level, Composition, and Degeneration.” *Journal of Biomechanics* 31(6): (1998), pp. 535-544.

42. Huyghe, JM et al: “Uniaxial Tensile Testing of Canine Annulus Fibrosus Tissue Under Changing Salt Concentrations.” *Biorheology* 41: (2004), pp. 255-261.

43. Ebara, S, JC Iatridis, et al: "Tensile Properties of Nondegenerate Human Lumbar Anulus Fibrosus." *Spine* 21(4): (1996), 452-461.

44. Acaroglu, JC Iatridis, et al: "Degeneration and Aging Affect the Tensile Behavior of Human Lumbar Anulus Fibrosus." *Spine* 20(24): (1995), 2690-2701.

45. Setton, LA et al: “Compressive Properties of the Cartilaginous End-Plate of the Baboon Lumbar Spine.” *Journal of Orthopaedic Research* 11: (1993), pp. 228-239.

46. Van Dieen, JH et al: “Stress Distribution Changes in Bovine Vertebrae Just Below the Endplate After Sustained Loading.” *Clinical Biomechanics* 16: (2001), pp. S135-S142.

47. Ishihara, H et al: "Effects of Continuous Quantitative Vibration on Rheologic and Biological Behaviors of the Intervertebral Disc." *Spine* 17: (1992), pp. S7-S12.

48. Setton, LA, W Zhu and VC Mow: "The Biphasic Poroviscoelastic Behavior of Articular Cartilage: Role of the Surface Zone in Governing the Compressive Behavior." *Journal of Biomechanics* 26: (1993), pp. 581-592.

49. Mow, VC et al: "Structure and Function of Articular Cartilage and Meniscus." Basic Orthopaedic Biomechanics and Mechanobiology, Ed by VC Mow and R Huiskies. New York, Lippincott Williams & Wilkins, (2005), pp. 181-259.

50. Osti, OL and RJ Moore: "Biochemistry and Histology of the Intervertebral Disc: Animal Models of Disc Degeneration." The Lumbar Spine, 2nd Ed. Ed by JN Weinstein and SW Wiesel. Philadelphia, W.B. Saunders Company, (1996), pp. 281-285.

51. Stokes, IAF and JC Iatridis: "Mechanical Conditions that Accelerate Intervertebral Disc Degeneration: Overload vs. Immobilization." Spine 29(23): (2004), pp. 2724-2732.

52. Garfin, SR and HN Herkowitz: "Lumbar Disc Degeneration: Normal Aging or a Disease Process?" The Lumbar Spine, 2nd Ed. Ed by JN Weinstein and SW Wiesel. Philadelphia, W.B. Saunders Company, (1996), pp. 458-473.

53. Videman, T and MC Battie': "Epidemiology of Disc." The Lumbar Spine, 2nd Ed., Ed by JN Weinstein and SW Wiesel. Philadelphia, W.B. Saunders Company, (1996), pp. 16-42.

54. Frymoyer, JW: "Magnitude of the Problem" The Lumbar Spine, 2nd Ed., Ed by JN Weinstein and SW Wiesel. Philadelphia, W.B. Saunders Company, (1996), pp. 8-16.

55. Vernon-Roberts, B: "Age Related and Degenerative Pathology of Intervertebral Discs and Apophyseal Joints." The Lumbar Spine and Back Pain. 4th Ed., Ed by MIV Jayson. Edinburgh, Churchill Livingstone. (1992), pp. 17-41.

56. Ljunggren, AE: "Natural History and Clinincal Role of the Herniated Disc." The Lumbar Spine, 2nd Ed., Ed by JN Weinstein and SW Wiesel. Philadelphia, W.B. Saunders Company, (1996), pp. 473-491.

57. Bogduk, N: "The Sources of Low Back Pain." The Lumbar Spine and Back Pain. 4th Ed., Ed by MIV Jayson. Edinburgh, Churchill Livingstone. (1992), pp. 61-88.

58. Keyes DC and EL Compere: "The Normal and Pathological Physiology of the Nucleus Pulposus of the Intervertebral Disc." *Journal of Bone and Journal Surgery* 14: (1932), pp. 897-935.

59. Sobajima, S et al: "A Slowly Progressive and Reproducible Animal Model of Intervertebral Disc Degeneration Characterized by MRI, X-Ray, and Histology." *Spine* 30(1): (2004), pp. 15-24.

60. Anderson, PA et al: "Intervertebral Disc Arthroplasty." *Spine* 29(23): (2004), pp. 2779–2786.

61. Shimer, AL et al: "Gene Therapy Approaches for Intervertebral Disc Degeneration." *Spine* 29(23): (2004), pp. 2770–2778.

62. Masuda, K et al: "Growth Factors and Treatment of Intervertebral Disc Degeneration." *Spine* 29(23): (2004), pp. 2757–2769.

63. Shimer, AL et al: "BMP-2 Gene Transfer Favorably Alters Course of Disc Degeneration in Rabbit Model." *Transactions of the 51st Annual Meeting of the Orthopaedic Research Society* Paper No. 183, Washington, D.C., February 20-23, (2005).

64. Agosti, CD et al: "Viscoelastic Modelling of Rabbit Nucleus Pulposus Tissue in Torsional Creep." *Transactions of the 52nd Annual Meeting of the Orthopaedic Research Society* Paper No. 1224, Chicago, IL, March 19-22, (2006).

65. Doraiswamy, D: "The Origins of Rheology: A Short Historical Excursion." *Rheology Bulletin* 71(1): (2002), pp. 1-9.

66. Findley, WN, JS Lai, et al. Creep and Relaxation of Nonlinear Viscoelastic Materials: With an Introduction to Linear Viscoelasticity. Amsterdam, North-Holland. (1976).

67. Macosko, CW. Rheology: Principles, Measurements, and Applications. New York, NY, VCH. (1994).

68. Lockett, FJ. Nonlinear Viscoelastic Solids. London, Academic Press. (1972).

69. Ferry, JD. Viscoeleastic Properties of Polymers. New York, Wiley, (1961).

70. Plazek, DJ: "Viscoelastic and Steady-State Rheological Response." Methods of Experimental Physics: Polymers, Physical Properties, Volume 16. Ed. by R.A. Fava. New York, Academic Press, (1980), pp. 1-58.

71. Slaughter, WS. The Linearized Theory of Elasticity. Boston, Birkhäuser. (2002).

72. Shames, IH and FA Cozzarelli. Elastic and Inelastic Stress Analysis. Revised Printing. Washington, D.C., Taylor and Francis, 1997.

73. Lakes, RS. Viscoelastic Solids. Boca Raton, CRC Press (1998).

74. Aklonis, JJ and WJ MacKnight. Introduction to Polymer Viscoelasticity. New York, Wiley. (1983).

75. Leaderman, H: "Viscoelasticity Phenomena in Amorphous High Polymeric Systems." Rheology: Theory and applications. Volume 2. Ed. by Eirich, F. R., New York, Academic Press. (1958), pp. 1-61.

76. Plazek, DJ: "Dynamic Mechanical and Creep Properties of a 23% Cellulose Nitrate Solution; Andrade Creep in Polymeric Systems." *Journal of Colloid Science* 15(1): (1960), pp. 50-75.

77. Bocchieri, Robert Thomas, "Time-Dependent Deformation of a Nonlinear Viscoelastic Rubber-toughened Fiber Composite with Growing Damage." (unpublished Ph.D. Dissertation, University of Texas at Austin, 2001).

78. Plazek, DJ, Private Communication, University of Pittsburgh, Pittsburgh, PA, (2005).

79. Wallace, DG, et al: "Shear Creep of Injectable Collagen Biomaterials." *Journal of Biomedical Materials Research* 21: (1987), pp. 861-880.

80. Provenzano, PP, RS Lakes, et al: "Application of Nonlinear Viscoelastic Models to Describe Ligament Behavior." *Biomechanical and Modeling in Mechanobiology* 1: (2002), pp. 45-57.

81. Provenzano, PP, RS Lakes, et al: "Nonlinear Ligament Viscoelasticity." *Annals of Biomedical Engineering* 29(10): (2001), pp. 908-914.

82. Schapery, RA: "On the Characterization of Nonlinear Viscoelastic Materials." *Polymer Engineering and Science* 9: (1969), pp. 295–310.

83. Andrade, EN da C: "On the Viscous Flow in Metals, and Allied Phenomena." *Proceedings of The Royal Society. A.* 84: (1910), pp. 1-12.

84. Plazek, DJ: "Viscoelastic Dispersion of Polydimethyl Siloxane in the Rubberlike Plateau Zone." *Journal of Colloidal Science* 16(2): (1961), pp. 101-126.

85. Cottrell, AH: "Andrade Creep." Philosophical Magazine Letters, 73(1): (1996), 35-37.

86. Andrade, EN da C: "The Validity of the $t^{1/3}$ Law of Flow of Metals." *Philosophical Magazine*, 7(84): (1962), pp. 2003-2013.

87. Kennedy, AJ: "On the Generality of the Cubic Creep Function." *Journal of the Mechanics and Physics of Solids* 1: (1953), pp. 172-181.

88. "AR500/1000 Rheometers Hardware Manual." TA Instruments, Inc., New Castle, DE, [PN 500017.001 Rev. E], (2003).

89. Pflaster, DS et al: "Effect of Test Environment on Intervertebral Disc Hydration." *Spine* 22(2): (1997), pp. 133-139.

90. Race, A: "Effect of Loading Rate and Hydration on the Mechanical Properties of the Disc." *Spine* 25(6): (2000), pp. 662-669.

91. Nice, D and M Brain: "How Humidifiers Work." HowStuffWorks, Inc., April 12, 2006, <http://home.howstuffworks.com/humidifier.htm>.

92. Devore, JL. Probability and Statistics for Engineering and the Sciences. 6th ed. Australia, Thomson/Brooks Cole, (2004).

93. Rees, DWA: "Nutting Creep in Mono- and Bi-Layer Polymers." *Plastics, Rubber and Composites* 31(8): (2002), pp. 350-358.

94. Smith, TL: "Physical Properties of Polymers – An Introductory Discussion." *Polymer Engineering and Science* 13(3): (1973), pp. 161-175.

95. Iatridis, JC, Private Communication, 52nd Ann Mtg ORS, Chicago, IL, March 20, 2006.